Damage Identification of Structures by Minimum Constitutive Relation Error and Sparse Regularization

Guo Jia

2019

Abstract

Methods for damage identification are undergoing increased attention and development. Finite element model-based methods treat damage identification as a constrained nonlinear optimization problem in which the discrepancy between the test data and the predictions from the numerical model is minimized.

This research focuses on the improvement of the overall performance of minimum constitutive relation error (min-CRE) based damage identification techniques for general applications. The objective function for identification is defined as the constitutive relation error (CRE), which is an energy inner product of the residual of the constitutive equation connecting the admissible stresses and the kinematically admissible displacements. The identification procedures using the CRE function has been applied to multiple types of measured data: static, modal, frequency response function and spectrum data. Different types of measured data correspond to different mathematical details for the formulation of the CRE function and thus result in different subsequent numerical solving processes.

To circumvent the ill-posedness of the inverse problem which is caused by use of the possibly insufficient data and enhance the robustness of the identification process, the sparse regularization is introduced where the ℓ_1-norm regularization term is added to the original CRE function. In regard to the minimum solution of the sparse-regularized CRE objective function, the alternating minimization (AM) method is established. The attractive features of the present damage identification approach are: (a) no sensitivity analysis is involved and high computational cost could be avoided; (b) as the objective function is separately convex, large damages may become identifiable; (c) while coping with the sparse regularization, a closed-form

solution can be obtained due to the decoupling feature of the CRE function with respect to the damage parameters and hence the sparse regularization term would introduce little computational complexity; (d) the sparse regularization parameters are directly determined by a simple threshold setting method.

Each chapter of this thesis concludes with several numerical and experimental case studies of increasing size. Throughout the case studies, the proposed approach by min-CRE and sparse regularization exhibits good identification accuracy and convergence properties for both small and large, single and multiple damage identification. Results also show that the sparse regularization obviously enhances the robustness of the damage identification procedure and the proposed approach has the advantage that it performs well even under the condition that only noise-contaminated measured data from few limited sensors are available during the identification process.

Acknowledgements

I wish to express my sincere gratitude to my supervisor, Professor Izuru Takewaki, for his sustained encouragement and guidance throughout the course of my Ph.D. studies. It was his experience and inspiration that kept the research going.

I would like to extend my appreciation to Dr. Li Wang for his indispensable contributions and collaboration in our joint research. My gratitude also extends to Professor Kohei Fujita for his extensive knowledge in the field of experimental modal analysis and system identification.

I also want to express my gratitude to my doctoral committee members, Professors Makoto Ohsaki and Yoshiki Ikeda for their time, supports and essential suggestions.

Thanks are also due to past and present colleagues who never hesitated to give a helping hand.

Finally, I would like to mention Professor Peng Pan who shared his insight into many related fields of interest.

Contents

List of Figures

List of Tables

Standard Abbreviations

AM Alternating Minimization

CRE Constitutive Relation Error

DOFs Degree of Freedoms

ExS-based the Excitation Spectrum-based

FE Finite Element

FEM Finite Element Method

FRF Frequency Response Function

GA Genetic Algorithm

min-CRE Minimum-Constitutive Relation Error

PEM Pseudo Excitation Method

ReS-based the Response Spectrum-based

SHM Structural Health Monitoring

UDP Update the damage parameters

UMF Update the mechanical field

1

Introduction

1.1 Damage identification

Damage can arise in structures due to operational incidents, extreme events and/or aggressive environmental conditions. It mainly causes a loss of structural stiffness which may affect the safety, integrity, serviceability and operation of structures. Thus, establishment of the structural health monitoring (SHM) system that provides damage and safety information for preventive maintenance, inspection and repair of structures becomes essential. Indeed, a reliable and effective non-destructive damage identification approach is always the core ingredient of the SHM system [1].

There are several conventional, experimental and local approaches that are able to directly identify the damage. The simplest one is visual inspection; however, it is often difficult and even impossible to work well since there may be damage scenarios that are not visible [2]. Other approaches, such as ultrasonic testing, radiography and thermal analysis, require the damaged region to be known *a priori* and accessible for testing, which cannot be guaranteed in most cases. Hence, global approaches accounting for global behavior of the damaged region are developed to overcome these difficulties [3–6]. Generally, global damage detection approaches are devoted to the identification of damage location and severity based on the procedure in which the responses caused by external excitations are measured from dynamic or static tests and thereafter, damage is often identified indirectly through numerical manipulations. A direct consequence of damage is the decrease in local stiffness, and therefore damage, regarded as changes in stiffness, can be detected using changes in dynamic or static characteristics since response characteristics are functions of structural stiffness. This has been the key idea of many extant global approaches [7–9].

In fact, the approaches, using strucutral response data in the damage identification process, could be classified into two groups: methods based on signals and methods based on models [10]. Signal-based methods received much attention in recent years and have been successfully applied to detect and locate structural damages [11, 12]. They are typically non-parametric methods and able to avoid modeling errors and high computational costs during numerical simulations. However, these methods are hard to assess the damage severity, sensitive to the measurement noise and mostly limited up to small-sized structures [10]. In contrast, the advantage of the methods based on models is obvious: able to identify the damage location and severity simultaneously and capable to take into account all of the available structural information.

Classically, the model-based methods treat damage identification as a constrained nonlinear optimization problem with the structural model parameters such as mass, stiffness and damping forming the basic variables. The objective function of the non-linear problem is usually set up by measuring the discrepancies between the numerical model and the test results. The selection of the objective function is a crucial issue. It does not only affect the interpretation of the best correlation, but also influences the behavior of the utilized optimization algorithm [13]. Weighted least squares of the errors between the measured data and the derived data is generally chosen as the objective function [14]. To solve this optimization problem, the genetic algorithms (GA) and the sensitivity-based approaches are commonly used [15–17]. Other opimization methods include the minimization of rank perturbation theory [18] and the 'residual force' method [19].

1.2 Minimum constitutive relation error

Recently, usage of the error in constitutive relation for damage identification has caught the attention of researchers [20–24]. This idea was first proposed for model updating analysis and then extended to structural damage identification problems in linear statics [25], transient dynamics [26], elastoplastics [27] and so on. In this approach, the objective function is defined as the constitutive relation error (CRE), that is, an energy inner product of the residual of the constitutive equation connecting the admissible stresses and the kinematically admissible displacements. This idea is enlightened by a recent variational theory of [24] for inverse parameter identification. As it is pointed out, damage parameters and stresses can be identified through minimization of the CRE objective function as long as displacement measurements are readily acquired under given loads. It is remarkable that the CRE function is separately convex (see Chapter 2 for detailed proofs), which guarantees the appropriate application of the efficient alternating minimization (AM) approach [28, 29] so as to get the solution of this nonlinear optimization problem. To this end, the sensitivity analysis is no longer needed.

To define the constitutive relation error (CRE), consider an elastic structure occupying the domain Ω and bounded by the boundary $\partial\Omega$ first. The mathematical equations of this linear elasticity problem could be described as

- Kinematic constraints

$$\boldsymbol{u} \in \mathfrak{U} := \begin{cases} \boldsymbol{\varepsilon} = \boldsymbol{B}\boldsymbol{u} \text{ in } \Omega \\ \boldsymbol{u} = \bar{\boldsymbol{u}} \text{ over } \partial\Omega_u \end{cases} \tag{1.1}$$

  where $\boldsymbol{B}$ is the strain-displacement matrix and $\bar{\boldsymbol{u}}$ is the prescribed value of the displacement filed $\boldsymbol{u}$ on the Dirichlet boundary $\partial\Omega_u$. $\boldsymbol{\varepsilon}$ represents the strain field.

- Equilibrium equations

$$\boldsymbol{\sigma} \in \mathfrak{S} := \begin{cases} \boldsymbol{\mathcal{L}}\boldsymbol{\sigma} + \bar{\boldsymbol{b}} = \boldsymbol{0} \text{ in } \Omega \\ \boldsymbol{n}\boldsymbol{\sigma} = \bar{\boldsymbol{t}} \text{ over } \partial\Omega_f \end{cases} \tag{1.2}$$

  where $\boldsymbol{\mathcal{L}}$ is the divergence operator (div) on stress filed $\boldsymbol{\sigma}$ and $\boldsymbol{n}$ the external unit vector normal to the Neumann boundary $\partial\Omega_f$. Over $\partial\Omega_f$, the traction field $\bar{\boldsymbol{t}}$ is prescribed. In addition, $\bar{\boldsymbol{b}}$ denotes the body force.

- Constitutive relations

$$\boldsymbol{\sigma} = \boldsymbol{D}\boldsymbol{\varepsilon} \tag{1.3}$$

  where $\boldsymbol{D}$ is an elastic modulus matrix with appropriate material properties.

Now consider an admissible physical pair $(\boldsymbol{u}, \boldsymbol{\sigma})$, of which the displacements $\boldsymbol{u}$ satisfy the kinematic constrains (1.1) ($\boldsymbol{u} \in \mathcal{U}$) and the stresses $\boldsymbol{\sigma}$ satisfy the equilibrium equations (1.2) ($\boldsymbol{\sigma} \in \Im$), respectively. It is easily known that, if the constitutive relations (1.3) are additionally satisfied with an elastic modulus matrix $\boldsymbol{D}(\boldsymbol{\theta})$ ($\boldsymbol{\theta} \in \mathcal{A} \subseteq \mathbb{R}^{m+}$), where $\mathcal{A}$ denotes the admissible damage parametric space with $\theta_e = 1$ meaning no damage of the eth element, the above admissible solution trio $(\boldsymbol{u}, \boldsymbol{\sigma}, \boldsymbol{\theta})$ would be the exact solution $(\boldsymbol{u}_{\text{ex}}, \boldsymbol{\sigma}_{\text{ex}}, \boldsymbol{\theta}_{\text{ex}})$. As a result, the CRE function (functional) is introduced as the following integral form

$$J = e_{\text{CRE}}(\boldsymbol{u}, \boldsymbol{\sigma}, \boldsymbol{\theta}) = \frac{1}{2} \int_{\Omega} \left(\boldsymbol{D}(\boldsymbol{\theta})\boldsymbol{B}\boldsymbol{u} - \boldsymbol{\sigma}\right)^T \boldsymbol{D}(\boldsymbol{\theta})^{-1} \left(\boldsymbol{D}(\boldsymbol{\theta})\boldsymbol{B}\boldsymbol{u} - \boldsymbol{\sigma}\right) \mathrm{d}\Omega. \tag{1.4}$$

Normally, *variational method* in which stationarity is sought is used to obtain the approximation of $(\boldsymbol{u}_{\text{ex}}, \boldsymbol{\sigma}_{\text{ex}}, \boldsymbol{\theta}_{\text{ex}})$ in the forms of equation (1.4). The reader not familiar with variations in the field of mathematical analysis may be confused about the solving process in the following sections. We shall introduce here some basic concepts of calculus of variations and review the variational procedures used in the finite element method (FEM) for obtaining the approximation in such integral forms, so as to help the reader to establish a comprehensive picture on how the principle of the proposed minimum constitutive relation error (min-CRE) obtains the desired results.

A '*variational principle*' specifies a scalar quantity (functional) Π, which is defined by an integral form

$$\Pi = \int_{\Omega} F\left(\boldsymbol{u}, \frac{\partial \boldsymbol{u}}{\partial x}, \cdots\right) \mathrm{d}\Omega + \int_{\Gamma} E\left(\boldsymbol{u}, \frac{\partial \boldsymbol{u}}{\partial x}, \cdots\right) \mathrm{d}\Gamma \tag{1.5}$$

in which $\boldsymbol{u}$ is the unknown admissible function and F and E are prescribed known functions or operators. The solution to the continuum problem is a function $\boldsymbol{u}$ which makes Π *stationary* with respect to arbitrary changes $\delta\boldsymbol{u}$ satisfying homogeneous boundary conditions. Thus, for a solution to the continuum problem, the 'variation' is

$$\delta\Pi = 0 \tag{1.6}$$

for any $\delta\boldsymbol{u}$, which defines the condition of stationarity [30].

Variational principles such as minimum potential energy may be well known to the reader in the field of FEM. The whole solving process of principle of minimum potential energy could be described as finding stationarity ($\delta\Pi_p(\boldsymbol{u}) = 0$) for $\Pi_p(\boldsymbol{u})$ under the constraints $\boldsymbol{u} \in \mathcal{U}$, as shown in **Table 1.1**. Another famous variational principle in

FEM, or say mixed FEM, is the Hellinger-Reissner variational principle [31, 32], which releases the kinematic constraints $\boldsymbol{u} \in \mathcal{U}$ by introducing these constraints into the original functional $\Pi_p(\boldsymbol{u})$, using the method of Lagrange multipliers. To this end, the new variational functional $\Pi_{HR}(\boldsymbol{u}, \boldsymbol{\sigma})$ becomes unconstrained, at the expense of increasing the total number of independent variables. In this case, the newly introduced Lagrange multipliers $\boldsymbol{\sigma}$ coincidentally correspond to the stresses which have a clear physical interpretation and thus their computation is also of interest. A further extension of such principles is known by the name of Hu-Washizu [33].

Above presents general concepts of the FEM. The comparison of using variational methods in the FEM [35] and the min-CRE is shown in **Figure 1.1**. As could be seen, the processes of finding stationarity of different variational principles with respect to different variables provide numerical approximations to different continuum problems. Different variational principles correspond to different integral forms, which indicate different release of the original elasticity problem and thus results in different more 'permissive' solutions. The principle of min-CRE is established on the integral form of the constitutive equation, which means the satisfying the constitutive equation at each material point is unnecessary (equilibrium equations, kinematic constrains and boundary conditions have to be strictly satisfied at each point), while the principle of minimum potential energy is derived from the integral form of the equilibrium equations and Neumann boundary conditions (BC) and the principle of minimum complementary energy from the integral form of the kinematic constrains.

Before proceeding further, it is worth noting that the principle of the proposed min-CRE obtains the numerous approximations of $(\boldsymbol{u}_{\mathrm{ex}}, \boldsymbol{\sigma}_{\mathrm{ex}}, \boldsymbol{\theta}_{\mathrm{ex}})$ by finding stationarity $(\delta J(\boldsymbol{u}, \boldsymbol{\sigma}, \boldsymbol{\theta}) = 0)$ for J under the constraints $\boldsymbol{u} \in \mathcal{U}$, $\boldsymbol{\sigma} \in \Im$, $\boldsymbol{\theta} \in \mathcal{A}$. Those constraints could also be released by the method of Lagrange multipliers [26, 34]. To distinguish the processes with and without Lagrange multipliers, the method using Lagrange multipliers is called 'principle of generalized minimum constitutive relation error' in this research (see **Table 1.1**). Although the Lagrange multipliers could change the original problem into unconstrained, unlike the Hellinger-Reissner variational principle, the physical meaning of the newly introduced Lagrange multipliers $\boldsymbol{u}^*$ seems rather hard to be understood. Indeed, the solution field $\boldsymbol{u}^*$ is the error in the displacement $\boldsymbol{u}$ introduced by the integral form of the constitutive equation ($\boldsymbol{\sigma} = \boldsymbol{DB}(\boldsymbol{u}+\boldsymbol{u}^*)$). To avoid such obscure step, Lagrange multipliers are not used in this research. Instead,

Table 1.1 Variational Principles

	Principle of minimum potential energy
Variational functional	$\Pi_P = \frac{1}{2}\int_\Omega \boldsymbol{\varepsilon}^{\mathrm{T}}\boldsymbol{D}\boldsymbol{\varepsilon}\mathrm{d}\Omega - \int_\Omega \boldsymbol{u}^{\mathrm{T}}\bar{\boldsymbol{b}}\mathrm{d}\Omega - \int_{\Omega_f} \boldsymbol{u}^{\mathrm{T}}\bar{\boldsymbol{t}}\mathrm{d}S$
Variational constraints	$\boldsymbol{u} \in \mathfrak{U} := \begin{cases} \boldsymbol{\varepsilon} = \boldsymbol{B}\boldsymbol{u} \text{ in } \Omega \\ \boldsymbol{u} = \bar{\boldsymbol{u}} \text{ over } \partial\Omega_u \end{cases}$
Stationary condition	$\delta\Pi_P = \dfrac{\partial \Pi_P}{\partial \boldsymbol{u}}\delta\boldsymbol{u} = 0$ (only $\boldsymbol{u}$ is independent)
	Hellinger-Reissner variational principle
Variational functional	$\Pi_{HR} = \dfrac{1}{2}\displaystyle\int_\Omega \boldsymbol{\sigma}^{\mathrm{T}}\boldsymbol{D}^{-1}\boldsymbol{\sigma}\mathrm{d}\Omega + \int_\Omega \boldsymbol{u}^{\mathrm{T}}\left(\boldsymbol{\mathcal{L}}\boldsymbol{\sigma} + \bar{\boldsymbol{b}}\right)\mathrm{d}\Omega - \int_{\Omega_f} \boldsymbol{u}^{\mathrm{T}}\left(\boldsymbol{n}\boldsymbol{\sigma} - \bar{\boldsymbol{t}}\right)\mathrm{d}S - \int_{\Omega_u} \bar{\boldsymbol{u}}^{\mathrm{T}}\left(\boldsymbol{n}\boldsymbol{\sigma}\right)\mathrm{d}S$
Variational constraints	Unconstrained
Stationary condition	$\delta\Pi_{HR} = \dfrac{\partial \Pi_{HR}}{\partial \boldsymbol{u}}\delta\boldsymbol{u} + \dfrac{\partial \Pi_{HR}}{\partial \boldsymbol{\sigma}}\delta\boldsymbol{\sigma} = 0$ ($\boldsymbol{\sigma}$ and $\boldsymbol{u}$ are independent)
	Principle of proposed minimum constitutive relation error
Variational functional	$J = \frac{1}{2}\int_\Omega \left(\boldsymbol{D}(\boldsymbol{\theta})\boldsymbol{\varepsilon} - \boldsymbol{\sigma}\right)^{\mathrm{T}}\boldsymbol{D}(\boldsymbol{\theta})^{-1}\left(\boldsymbol{D}(\boldsymbol{\theta})\boldsymbol{\varepsilon} - \boldsymbol{\sigma}\right)\mathrm{d}\Omega$
Variational constraints	$\boldsymbol{u} \in \mathfrak{U} := \begin{cases} \boldsymbol{\varepsilon} = \boldsymbol{B}\boldsymbol{u} \text{ in } \Omega \\ \boldsymbol{u} = \bar{\boldsymbol{u}} \text{ over } \partial\Omega_u \end{cases}$ $\boldsymbol{\sigma} \in \mathfrak{S} := \begin{cases} \boldsymbol{\mathcal{L}}\boldsymbol{\sigma} + \bar{\boldsymbol{b}} = \boldsymbol{0} \text{ in } \Omega \\ \boldsymbol{n}\boldsymbol{\sigma} = \bar{\boldsymbol{t}} \text{ over } \partial\Omega_f \end{cases}$ $\boldsymbol{\theta} \in \mathcal{A} \subseteq \mathbb{R}^{m+}$
Stationary condition	$\delta J = \dfrac{\partial J}{\partial \boldsymbol{u}}\delta\boldsymbol{u} + \dfrac{\partial J}{\partial \boldsymbol{\sigma}}\delta\boldsymbol{\sigma} + \dfrac{\partial J}{\partial \boldsymbol{\theta}}\delta\boldsymbol{\theta} = 0$ ($\boldsymbol{\sigma}$, $\boldsymbol{u}$ and $\boldsymbol{\theta}$ are independent)
	Principle of generalized minimum constitutive relation error [26, 34]
Variational functional	$J' = \dfrac{1}{2}\displaystyle\int_\Omega \left(\boldsymbol{D}(\boldsymbol{\theta})\boldsymbol{\varepsilon} - \boldsymbol{\sigma}\right)^{\mathrm{T}}\boldsymbol{D}(\boldsymbol{\theta})^{-1}\left(\boldsymbol{D}(\boldsymbol{\theta})\boldsymbol{\varepsilon} - \boldsymbol{\sigma}\right)\mathrm{d}\Omega - \int_\Omega \boldsymbol{u}^{*\mathrm{T}}\left(\boldsymbol{\mathcal{L}}\boldsymbol{\sigma} + \bar{\boldsymbol{b}}\right)\mathrm{d}\Omega - \int_{\Omega_u} \boldsymbol{t}^{*\mathrm{T}}\left(\boldsymbol{u} - \bar{\boldsymbol{u}}\right)\mathrm{d}S - \int_{\Omega_f} \boldsymbol{\mu}^{\mathrm{T}}\left(\boldsymbol{n}\boldsymbol{\sigma} - \bar{\boldsymbol{t}}\right)\mathrm{d}S$
Variational constraints	$\boldsymbol{\varepsilon} = \boldsymbol{B}\boldsymbol{u}$ in Ω, $\boldsymbol{\theta} \in \mathcal{A} \subseteq \mathbb{R}^{m+}$
Stationary condition	$\delta J' = \dfrac{\partial J'}{\partial \boldsymbol{u}}\delta\boldsymbol{u} + \dfrac{\partial J'}{\partial \boldsymbol{\sigma}}\delta\boldsymbol{\sigma} + \dfrac{\partial J'}{\partial \boldsymbol{\theta}}\delta\boldsymbol{\theta} + \dfrac{\partial J'}{\partial \boldsymbol{u}^*}\delta\boldsymbol{u}^* + \dfrac{\partial J'}{\partial \boldsymbol{t}^*}\delta\boldsymbol{t}^* + \dfrac{\partial J'}{\partial \boldsymbol{\mu}}\delta\boldsymbol{\mu}$ (only $\boldsymbol{u}, \boldsymbol{u}^*$ and $\boldsymbol{\theta}$ are independent [26])

*Note: $\boldsymbol{t}^*, \boldsymbol{u}^*, \boldsymbol{\mu}$ are the Lagrange multipliers associated with the constraints.

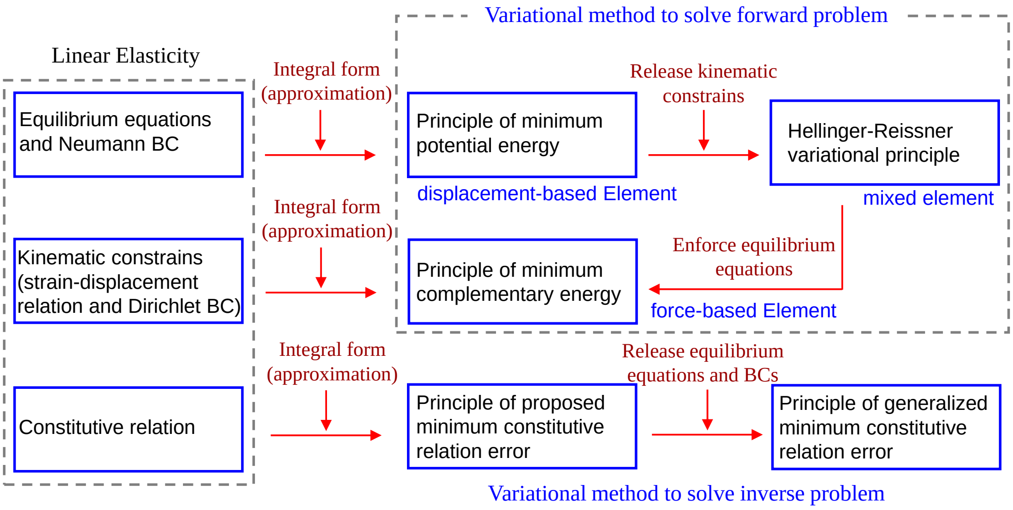

Figure 1.1 Overview of variational methods

constraints are directly imposed into the corresponding variables. It is well known that admissible displacement field $\boldsymbol{u}$ which satisfies the kinematic constraints could be approximated by the selection of appropriate shape functions in displacement-based element. However, the difficulty lies in how to obtain the admissible stress field $\boldsymbol{\sigma}$ which satisfies the equilibrium equations and the Neumann boundary within the principle of min-CRE. In this research, two novel distinct solving processes are proposed. The first is to use force-based element which pre-satisfies the admissibility condition in the stress field (Chapter 2∼4). Degrees of freedom (DOFs) of the independent global nodal force are found by the formulation of nodal force equilibrium. This procedure is efficient and convenient with respect to the beam-type elements but may lead to solving sophistication for other types of elements. The second is to obtain the admissible stress field $\boldsymbol{\sigma}$ directly through the equilibrium equation by acquiring the pseudoniverse of the transpose of the strain-displacement matrix (Chapter 5). The pseudoniverse is computed by using the singular value decomposition (SVD). This procedure is recommended for a more general physical problem. Once the admissible physical fields $(\boldsymbol{u}, \boldsymbol{\sigma})$ are founded and the corresponding stationary condition is determined, subsequent operations follow a standard mathematical path. Chapter 2∼3 consider the corresponding finite element formulation arising in a plane while Chapter 4∼5 concern the formulations in 3D space. In this thesis, we chose to present the proposed technique in the simplified case of the identification of the properties in elastic beam elements. The method can also be applied to more complicated cases in general continuum mechanics. Nevertheless, this simplified framework is sufficient to test the capabilities of the approach.

1.3 ℓ_p-norms and regularization

For large scale civil structures, it is often required to identify the structural parameters based on the incomplete structural response measurement data. This is essentially an ill-posed inverse problem. Attempting to circumvent this drawback, regularization techniques such as the Tikhonov regularization and the sparse regularization are always introduced. The idea that all the damages or changes of parameters are as small as possible is implicated in the Tikhonov regularization [36]. Such an idea is reasonable for model updating however, it may not be appropriate for damage identification since large damages may occur. On the other hand, damages always occur at a few locations where maximum-stress/plasticity appears, impact loads work or crack propagates for practical structures. This would be appropriately implicated in the sparse regularization [37, 38], which weakly enforces the sparsity constraint for the damage locations.

Back to the basics in mathematics, the process of adding a norm to the objective function for the optimization problem is known as *regularization*. One can regularize the data for different underlying reasons and with different effects. In the case of Tikhonov and sparse regularizations, both of these regularizers are built to solve colinearity and model complexity; but the way in which they attain the goals is fundamentally different. The properties of regularizing with ℓ_2–norm and ℓ_1–norm are what causes these differences. For generalized mathematical definition, a norm is a mapping $\|\cdot\|$ from a vector space X into $\mathbb{R}$ which satisfies the following properties for every $\boldsymbol{x} \in X$ and $\boldsymbol{y} \in X$ and every $\alpha \in \mathbb{C}$:

$$\begin{cases} \|\boldsymbol{x}\| \geq 0 \\ \|\alpha\boldsymbol{x}\| = |\alpha| \mid \|\boldsymbol{x}\| \\ \|\boldsymbol{x}+\boldsymbol{y}\| \leq \|\boldsymbol{x}\| + \|\boldsymbol{y}\| \end{cases} \tag{1.7}$$

A norm generalizes the concept of distance inherited from Euclideam geometry. One of the most commonly used norms are the ℓ_p-norms, which for a vector space $X \in \mathbb{C}^n$

and $0 < p \leq \infty$ is defined as

$$\|\boldsymbol{x}\|_p = \left(\sum_{i=1}^{n} |x_i|^p \right)^{1/p} \tag{1.8}$$

In the case of $p = 2$, one obtain the usual ℓ_2–norm or say, Tikhonov regularization term. Mathematically, the regularization norms $\|x\|_p$ with $0 \leq p \leq 1$ all can enforce sparsity in solution $\boldsymbol{x}$. In this research, the sparse regularization is specified as ℓ_1–norm regularization, that is, $p = 1$, in equation (1.8). The main reason is that although the ℓ_1–norm is weaker than the $p < 1$ norm in ensuring sparsity, ℓ_1-regularized optimization is a convex problem and admits efficient solution using linear programming techniques [39].

To get a better physical interpretation of Tikhonov and sparse regularizations, consider a simple structural system (see **Figure 1.2**) with n displacement DOFs $\boldsymbol{x}$ and the potential energy of the system is designated as $f(\boldsymbol{x})$. On one hand, if the spring of stiffness 2μ is additionally enforced onto every mass (see **Figure 1.2**(b)), the potential energy becomes $f_\mu(\boldsymbol{x}) = f(\boldsymbol{x}) + \mu\|\boldsymbol{x}\|_2^2$, which obviously corresponds to the Tikhonov regularization. Adding springs to all masses would physically decrease the displacements and this coincides well with the effect of the Tikhonov regularization. On the other hand, if all masses are placed on a frictional surface with the same threshold value of the static friction force λ (see **Figure 1.2**(c)), the potential energy would be changed into $f_\lambda(\boldsymbol{x}) = f(\boldsymbol{x}) + \lambda\|\boldsymbol{x}\|_1^1$, which is equivalent to the ℓ_1–norm regularization. As is noteworthy, if the prescribed friction λ is greater than the maximum of the forces exerted on all masses, no movement ($\boldsymbol{x} = 0$) would occur, while if the prescribed friction λ is less than the $k(\ll n)$ greatest ones of the forces exerted on all masses but larger than others, k masses corresponding to k greatest forces would admit some movement and others keep unmoved; this leads to the sparse solution of $\boldsymbol{x}$. To conclude, with a proper choice of λ, the sparsity of the solution $\boldsymbol{x}$ can be reached by the ℓ_1–norm regularization and therefore, the ℓ_1-norm term $\lambda\|\boldsymbol{x}\|_1^1$ can indeed serve for the sparse regularization. Details on how to obtain the appropriate value of the regularization parameter λ is discussed mainly in Chapter 3 and identification results of comparison between Tikhonov and sparse regularizations are drawn in Chapter 4.

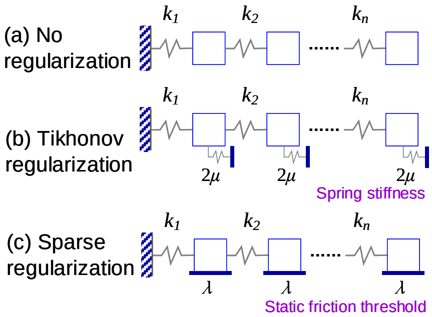

Figure 1.2 Physical interpretation of regularizations

1.4 Objectives of research

The objective of the research presented in this thesis is to improve the overall performance of min-CRE based damage identification techniques for general applications. The specific objectives relevant to this work are:

1. To develop the computational procedures for applying the min-CRE principle into multiple types of measured data;

2. To clarify the mathematical advantages of the CRE objective function with respect to the damage parameters;

3. To find sparse solutions to the ill-posed inverse problems;

4. To present a novel and simple threshold setting method to properly determine the sparse regularization parameters.

The following outline of the thesis briefly summaries the content of each chapter. The order of the chapters largely follows with the progress made during research.

1.5 Outline of thesis

Damage identification methods are always categorized based on the type of measured data used. In this research, the presentation has been divided into six chapters, representing probably the most widely used measured data: static (Chapter 2), modal (Chapter 3), frequency response function (FRF) (Chapter 4) and spectrum (Chapter 5) data, except for the first introduction and last conclusion chapters, as shown in

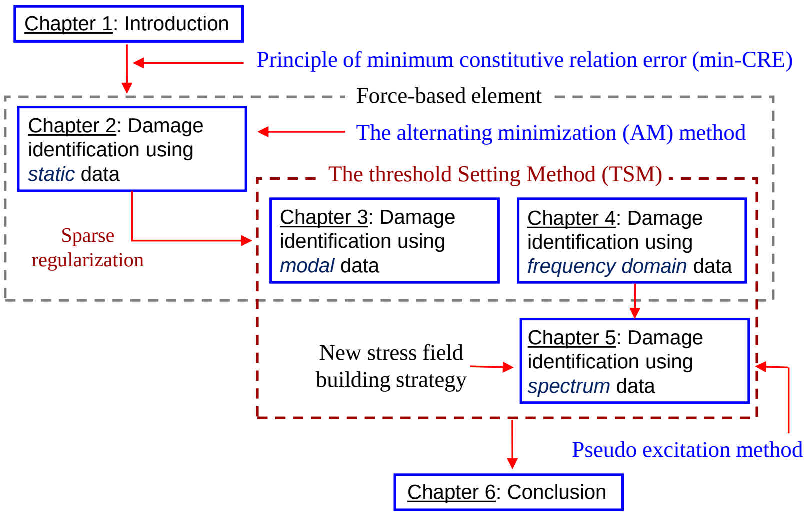

Figure 1.3 Outlines of thesis

Figure 1.3. Different types of measured data correspond to different mathematical details for the formulation of the CRE function and thus result in different subsequent numerical solving processes.

Chapter 2 illustrates the basic min-CRE principle theoretically. Damage identification is performed based on static tests, without the need to consider any additional knowledge of mass and damping information. Under this circumstance, the static equilibrium equation is only related to the structural stiffness, and static displacement and strain measurements can be obtained accurately, rapidly and cheaply. Two novel identification approaches are proposed: the min-CRE approach for full-field measurements and the modified min-CRE approach for finite-point measurements, respectively. The difference between the two approaches is whether to use additional penalty terms for the enforcement of the experimental displacement data or not. Multiple loads and associated sets of measurements are also considered to improve the identifiability and robustness of the procedure. The alternating minimization (AM) method has been established to fulfill the practical implementation and its convergence has been proved. Numerical tests have been carried out to verify these approaches.

Chapter 3 presents a modal-based sparse-regularized min-CRE approach for structural damage identification. In particular, modal data (natural frequencies and mode shapes) have found broad application as a target for parameter identification due to the convenience in obtaining modal data, e.g., through ambient tests. To circumvent the ill-posedness of the inverse problem that is caused by use of the possibly insufficient modal data and enhance the robustness of the identification process, the sparse regularization is introduced where a sparse (or ℓ_1-norm) regularization term is added to the original CRE function. The attractive feature of this damage identification approach is that no sensitivity analysis is involved herein and the additional introduction of the sparse regularization term introduces little computational complexity. The approach is applied to damage identification of beam structures with experimental or simulated modal data. Results show that the sparse regularization indeed improves the effectiveness and robustness of the min-CRE approach under measurement noises and initial model errors.

Chapter 4 aims at providing a sparse-regularized min-CRE approach using FRF data for damage identification. Vibration-based damage identification using FRF measurements has been studied by a number of references and it has been proved that FRF data are more reliable and practical to provide abundant information at measured degrees of freedom and at a great number of desired frequencies without being contaminated by any modal extraction errors and loss of information. Particular attention should be paid to properly select the frequency ranges of the frequency response data. Numerical results show that the proposed approach is more efficient, more accurate and less sensitive to the modeling errors than the sensitivity-based approaches with the Tikhonov regularization.

Chapter 5 is concerned with a spectrum-driven damage identification strategy based on min-CRE approach. For large-scale architectural or civil structures under the action of stationary random excitations such as earthquake ground motions and random wind loads, the power spectral density matrix of structural responses are more easily obtained. The above stationary random vibration problem is transformed into a series of harmonic vibrations by the pseduo excitation method (PEM) and building of the admissible stress field is addressed in a much simpler way by using singular value decomposition. The proposed method has the advantage that only measurement power spectrum density data from few limited sensors are needed for the inverse problem. Numerical and experimental verification examples show that the proposed method is insensitive to measurement noise and effective for both small and large damage identifications.

Chapter 6 summarizes the research work performed in this thesis, emphasizes the main original contributions and findings of the research work and provides recommendations for future research.

2

Damage identification using static data

2.1 Problem statement

2.1.1 Baseline model

Consider a one-dimensional Euler-Bernoulli beam defined in interval $X = [x_s, x_e]$ as shown in **Figure 2.1**. The curve $w(x)$ describes the deflection of the beam at some position x. The flexural stiffness of the beam is assumed to be $k(x) = EI(x)$. Loading conditions are distributed loads $q(x)$ and concentrated loads F^{ex}, M^{ex} along with boundary displacements w_p on the prescribed displacement boundary Σ. In this beam model, the bending moment M is directly related to the curvature through the constitutive relation $M = k\theta' = kw''$ and the shear force V is given by $V = M'$, where $f' = \frac{df}{dx}$ and $f'' = \frac{d^2f}{dx^2}$. For general equilibrium, $V' = M'' = q(x)$ and V, M should be in equilibrium with concentrated loads. Space H^2 is the Sobolev space defined with the derivatives up to the second order being square-integrable and it is usually known as containing the C^1-continuous functions and space L^2 is the Lebesgue space of square-integrable functions. The beam model can be described as a combination of the following three parts:

- **Kinematic constraints**

$$\mathcal{U} = \{w \in H^2(X) : w = w_p \text{ on } \Sigma\} \tag{2.1}$$

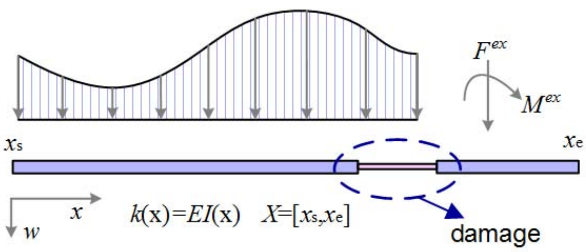

Figure 2.1 Model of Euler-Bernoulli beam

- **Equilibrium equations**

  Find bending moment $M \in \Im$ with

$$\Im = \{M \in L^2(X) : \int_X M v'' dx = \int_X q(x) v dx + \sum (F^{ex} v(x^{ex}) + M^{ex} v'(x^{ex})), \forall v \in \mathcal{U}_0\} \tag{2.2}$$

  where x^{ex} denotes the position where concentrated loads F^{ex}, M^{ex} are enforced and $\mathcal{U}_0$ the homogeneous part of $\mathcal{U}$;

- **Constitutive relations**

$$M = kw'' \tag{2.3}$$

  with $k \in \mathcal{C} = \{k \in L_2(X) : \exists 0 < c_0 < C_0,$ such that $c_0 \leq k(x) \leq C_0\}$ representing a positive and bounded stiffness field.

Generally, $\mathcal{U}$, $\Im$, $\mathcal{C}$ that will be used frequently in what follows are called the spaces of (kinematically) admissible displacement field, (statically) admissible bending moment field and (constitutively) admissible elastic stiffness field, respectively.

2.1.2 Constitutive relation error (CRE) function

Consider an admissible solution trio $(\tilde{w}, \tilde{M}, \tilde{k})$ which satisfies

$$\tilde{w} \in \mathcal{U}, \tilde{M} \in \Im, \tilde{k} \in \mathcal{C} \tag{2.4}$$

It is easily known that if the constitutive equation (2.4) is additionally satisfied, the solution trio would be the exact solution of the Euler-Bernoulli beam model. Thus, to measure the distance of the admissible solution trio to the exact solution trio in energy product, an error in constitutive relation is introduced

$$e_{CRE}(\tilde{w}, \tilde{M}, \tilde{k}) = \frac{1}{2}\int_X \frac{(\tilde{M} - \tilde{k}\tilde{w}'')^2}{\tilde{k}} dx \qquad (2.5)$$

which is termed the constitutive relation error (CRE) [40, 41] (or constitutive equation gap (CEG) [42].

2.2 Damage identification by min-CRE approach

In practice, damage identification approaches appear to be limited with respect to certain displacement measurement techniques. Herein, two cases regarding full-field displacement measurements and finite-point displacement data, respectively, are considered within the framework of the minimum CRE principle. For the first case using full-field displacement measurements, the CRE functional (2.5) is directly treated as the objective functional and the parameter identification approach is referred to as the min-CRE approach; while in case of finite-point measurement data, the CRE functional along with additional penalty terms for treatment of the finite-point displacement measurements are defined as the objective functional. The second identification case is more applicable and can be viewed as extension of the first identification case, therefore, the identification approach involved in the second case is referred to as the modified min-CRE approach.

2.2.1 Min-CRE approach

Assume that the spaces $\mathcal{C}$, $\mathcal{U}$, and $\Im$ for search of the stiffness k, displacement w and the bending moment M, respectively, are already known. Then, identification of the stiffness k as well the bending moment M from the full-field displacement data $\hat{w}$ pertains to the following minimization of the CRE functional (2.5), i.e.,

$$(M, k) = \arg \min_{\tilde{M}\in\Im, \tilde{k}\in\mathcal{C}} F(\tilde{M}, \tilde{k}); \;\; F(\tilde{M}, \tilde{k}) := e_{CRE}(\tilde{M}, \tilde{k}, \hat{w}) \qquad (2.6)$$

which is known as the minimum CRE principle [43] for identification problems. To proceed further, it is necessary to clarify some important properties of the CRE functional $F(\cdot, \cdot, \cdot)$.

Theorem 2.2.1. *The following properties for $F(\cdot,\cdot)$ on compact spaces $\Im \times \mathfrak{C}$ hold:*

(a) $F(\tilde{M},\tilde{k}) \geq 0, \forall(\tilde{M},\tilde{k}) \in \Im \times \mathfrak{C}$.

(b) $F(\tilde{M},\tilde{k}) = 0$ *if and only if the constitutive relation* $\tilde{M} = \tilde{k}\hat{w}''$ *is verified.*

(c) The functional $F(\cdot,\cdot)$ *is convex on* $\Im \times \mathfrak{C}$.

(d) The convexity of $F(\cdot,\cdot)$ *on* $\Im \times \mathfrak{C}$ *guarantees the existence of the minimizer to problem* (2.6)*. Then, if* $\mu(x \in X : \hat{w}'' = 0) = 0$ *with* $\mu(\cdot)$ *denoting the Lebesgue measure, the minimizer must lie in* $\Im^* \times \mathfrak{C}$ *with* $\Im^* = \{M \in \Im : \mu(x \in X : M(x) = 0) = 0\}$ *and moreover,* $F(\cdot,\cdot)$ *possesses separately strict convexity on* $\Im^* \times \mathfrak{C}$.

Proof of Theorem 2.2.1.

(a) and (b) are obvious.

(c) Let δ denote the variation operator. Then, one has for

$$\begin{array}{l} \delta\tilde{M} \in \Im_0 = \{M \in L_2(X) : \int_X Mv''dx = 0, \forall v \in \mathfrak{U}_0\}, \\ \delta\tilde{k} \in \mathfrak{C}_0 = \{k \in L_2(x) :\mid \delta k(x) \mid\leq C_0 - c_0, \forall x \in X\}, \\ \forall(\tilde{M},\tilde{k}) \in \Im \times \mathfrak{C} \end{array} \tag{2.7}$$

where $\Im_0$ and $\mathfrak{C}_0$ are the corresponding trial spaces. To verify convexity of $F(\cdot,\cdot)$, the term $F(\tilde{M}+\delta\tilde{M},\tilde{k}+\delta\tilde{k})$ with $(\delta\tilde{M},\delta\tilde{k}) \in (\Im_0,\mathfrak{C}_0)$ is expressed in Taylor expansion, i.e.

$$\begin{array}{l} F(\tilde{M}+\delta\tilde{M},\tilde{k}+\delta\tilde{k}) \\ = F(\tilde{M},\tilde{k}) + \int_X \left[\frac{\tilde{M}-\tilde{k}w''}{\tilde{k}}\delta\tilde{M} + \frac{1}{2}(-\frac{\tilde{M}^2}{\tilde{k}^2} + (w'')^2)\delta\tilde{k}\right]dx \\ +\frac{1}{2}\int_X \left[\frac{(\delta\tilde{M})^2}{\tilde{k}} + \frac{\tilde{M}^2}{\tilde{k}^3}(\delta\tilde{k})^2 - 2\frac{\tilde{M}}{\tilde{k}^2}\delta\tilde{M}\cdot\delta\tilde{k}\right]dx + h.o.t \\ := \phi(\tilde{M},\tilde{k}) + \frac{1}{2}\delta^2 F + h.o.t \end{array} \tag{2.8}$$

where $h.o.t.$ contains higher (than two) order variation terms, and $\phi(\tilde{M},\tilde{k})$ and $\delta^2 F$ are the respective tangential hyper-plane and second order variation of $F(\cdot,\cdot)$ at $(\tilde{M},\tilde{k})$, that are of the following forms

$$\phi(\tilde{M},\tilde{k}) = F(\tilde{M},\tilde{k}) + \int_X \left[\frac{\tilde{M}-\tilde{k}w''}{\tilde{k}}\delta\tilde{M} + \frac{1}{2}(-\frac{\tilde{M}^2}{\tilde{k}^2} + (w'')^2)\delta\tilde{k}\right]dx \tag{2.9}$$

and

$$\begin{aligned} \delta^2 F &= \int_x \left[\frac{(\delta\tilde{M})^2}{\tilde{k}} + \frac{\tilde{M}^2}{\tilde{k}^3}(\delta\tilde{k})^2 - 2\frac{\tilde{M}}{\tilde{k}^2}\delta\tilde{M}\cdot\delta\tilde{k}\right]dx \\ &= \int_X \frac{1}{\tilde{k}}(\delta\tilde{M} - \frac{\tilde{M}}{\tilde{k}}\delta\tilde{k})^2 \\ &\geq \int_X \frac{1}{C_0}(\delta\tilde{M} - \frac{\tilde{M}}{\tilde{k}}\delta\tilde{k})^2 \end{aligned} \tag{2.10}$$

Obviously, $\delta^2 F \geq 0$ implies the convexity of $F(\cdot,\cdot)$.

(d) Denote the minimizer by (M, k), which satisfies the following two conditions,

$$\int_X \frac{M^2}{k^2}\delta\tilde{k}dx = \int_X (w'')^2\delta\tilde{k}dx, \forall\delta\tilde{k} \in \mathfrak{C}_0 \tag{2.11}$$

and

$$\int_X \frac{M}{k}\delta\tilde{M}dx = \int_X w''\delta\tilde{M}dx, \forall\delta\tilde{M} \in \Im_0 \tag{2.12}$$

Then, contradiction is utilized to verify

$$\mu(x \in X : w''(x) = 0) = 0 \Rightarrow \mu(x \in X : M(x) = 0) = 0. \tag{2.13}$$

Assume that there exists a subset $X_{pp} \subseteq X$ with $\mu(X_{pp}) > 0$ such that $M(x) = 0$ on X_{pp}. Trivially, substitution of $\delta\tilde{k} = \begin{cases} c, x \in X_{pp} \\ 0, x \in X \setminus X_{pp} \end{cases}, c = \frac{1}{2}(C_0 - c_0) > 0$ into equation (2.11) yields

$$\int_{X_{pp}} c(w'')^2 dx = 0 \tag{2.14}$$

which contradicts with the condition $\mu(w''(x) = 0, x \in X) = 0$.

Next, let $\delta^2_{\tilde{M}}F$ and $\delta^2_{\tilde{k}}F$ denote the second order variations on $F(\cdot,\cdot)$ for $\tilde{M}$ and $\tilde{k}$, respectively. By a similar derivation to equation (2.10), one has

$$\begin{aligned} \delta^2_{\tilde{M}}F &= \int_X \frac{(\delta\tilde{M})^2}{\tilde{k}}dx \geq \frac{1}{C_0}\int_X (\delta\tilde{M})^2 dx > 0, \\ \delta^2_{\tilde{k}}F &= \int_X \frac{\tilde{M}^2}{\tilde{k}^3}(\delta\tilde{k})^2 dx \geq \frac{1}{C_0^3}\int_X \tilde{M}^2(\delta\tilde{k})^2 > 0 \end{aligned} \tag{2.15}$$

for $\int_X (\delta\tilde{M})^2 dx > 0$, $\int_X (\delta\tilde{k})^2 > 0$ and $\tilde{M} \in \Im^*$,indicating the separately strict convexity on $\Im^* \times \mathfrak{C}$. □

According to Theorem 2.2.1, it is seen that the damaged stiffness is identifiable through the minimum CRE principle in beams. Theoretically, the complete and unique identification of the damage requires some extra conditions on the static measurements—which are inherent in the context of inverse problems (see the following Remark)-including the deforming condition $\mu(\tilde{w}''(x) = 0, x \in X) = 0$ such that $F(\cdot,\cdot)$ becomes strictly convex in the vicinity of the minimizer.

Remark. *From equation* (2.12)*, it is found that*

$$\int_X \frac{\tilde{M}}{\tilde{k}}\delta\tilde{M}dx = \int_X w''\delta\tilde{M}dx = \sum_p (\theta_p\delta\tilde{M}\mid_p + w_p(\delta\tilde{M})'\mid_p) \tag{2.16}$$

where the subscript p indicates the prescribed displacement boundary condition. Obviously, equation (2.16) *embodies the minimum complementary energy principle*

$$M(\tilde{k}) = arg \min_{\tilde{M}\in\Im} \{\frac{1}{2}\int_X \frac{\tilde{M}^2}{\tilde{k}}dx - \sum_p(\theta_p\tilde{M}\mid_p + w_p(\tilde{M})'\mid_p)\} \tag{2.17}$$

and there corresponds to a unique mapping $d : \mathfrak{C} \to \mathfrak{U}$ *such that*

$$\int_X \tilde{k}(d(\tilde{k}))''v''dx = \int_X q(x)vdx + \sum(F^{ex}v(x^{ex}) + M^{ex}v'(x^{ex})), \forall v \in \mathfrak{U}_0 \tag{2.18}$$

and $M(\tilde{k}) = \tilde{k}(d(\tilde{k}))''$*. With these notations, the minimization problem* (2.6) *can become*

$$\min_{\tilde{M}\in\Im,\tilde{k}\in\mathfrak{C}} = \min_{\tilde{k}\in\mathfrak{C}} \frac{1}{2}\int_X \frac{(M(\tilde{k}) - \tilde{k}w'')^2}{\tilde{k}}dx = \min_{\tilde{k}\in\mathfrak{C}} \frac{1}{2}\int_X \tilde{k}\left|(d(\tilde{k}) - w)''\right|^2 dx \tag{2.19}$$

which is a common variational form for inverse identification and its well-posedness has been investigated in a variety of work (see [44–46] for instance). As indicated in the work, problem (2.19) *as well as problem* (2.6) *will have a unique minimizer if* $\inf_{x\in X}|w''| > 0$ *and* $\tilde{k}$ *is prescribed along the inflow portion of the boundary [47]. It is noted that* $\inf_{x\in X}|w''| > 0$ *is a stronger version of the deforming condition* $\mu(x \in X : w''(x) = 0) = 0$.

In practice, using more than one set of static measurements could improve the identifiability and robustness of the identification procedure and provide remedy for possible unidentifiability of the proposed approach [28, 48]. To this end, the objective functional as well as the identification procedure becomes,

$$\begin{aligned}(M^{(1)}, M^{(2)}, \dots, k) &= \arg \min_{\tilde{M}^{(j)}\in\Im^{(j)},\tilde{k}\in\mathfrak{C}} F(\tilde{M}^{(1)}, \tilde{M}^{(2)}, \dots, \tilde{k});\\ F(\tilde{M}^{(1)}, \tilde{M}^{(2)}, \dots, \tilde{k}) &:= \sum_j r_j e_{CRE}(\tilde{M}^{(j)}, \tilde{k}, \hat{w}^{(j)})\end{aligned} \tag{2.20}$$

where $\hat{w}^{(j)}$ denotes the jth set of full-field displacement data resulting from the loading condition $\tilde{M}^{(j)} \in \Im^{(j)}$and $r_j > 0$ is the corresponding weight.

2.2.2 Modified min-CRE approach

In most cases, finite-point displacement measurements rather than full-field displacement measurements are available. Let $\{\hat{w}_i, i \in \wp\}$ be the measured finite-point displacement data on the set of points $\{i \in \wp\}$ and then, a new objective functional as well as a new parameter identification formulation is given as follows.

$$\begin{aligned} F_{\mathrm{mod}}(\tilde{M},\tilde{k},\tilde{w}) &:= e_{CRE}(\tilde{M},\tilde{k},\tilde{w}) + \sum_{i\in\wp}\frac{\alpha_i}{2}\left(\tilde{w}_i-\hat{w}_i\right)^2 \\ (M,w,k) &= \arg\min_{\tilde{M}\in\Im,\tilde{w}\in\mathcal{U},\tilde{k}\in\mathcal{C}} F_{\mathrm{mod}}(\tilde{M},\tilde{k},\tilde{w}); \end{aligned} \tag{2.21}$$

where w_i is the displacement of w at point i and $\{\alpha_i > 0, i\in\wp\}$ represent the penalty factors. Practically, values of $\{\alpha_i > 0, i\in\wp\}$ could be tuned according to the confidence of the corresponding displacement data: $\alpha_i \to +\infty$ means completely trust of this data, while $\alpha \to 0$ means completely untrust. Again, in case of multiple sets of static data, the parameter identification can read,

$$\begin{aligned} &(M^{(1)}, w^{(1)}, M^{(2)}, w^{(2)}, \ldots, k) = \\ &\arg\min_{\tilde{M}^{(j)}\in\Im^{(j)},\tilde{w}^{(j)}\in\mathcal{U}^{(j)},\tilde{k}\in\mathcal{C}} F_{\mathrm{mod}}(\tilde{M}^{(1)},\tilde{w}^{(1)},\tilde{M}^{(2)},\tilde{w}^{(2)},\ldots,\tilde{k}); \\ &F_{\mathrm{mod}}(\tilde{M}^{(1)},\tilde{w}^{(1)},\tilde{M}^{(2)},\tilde{w}^{(2)},\ldots,\tilde{k}) := \\ &\sum_j r_j\left\{e_{CRE}(\tilde{M}^{(j)},\tilde{k},\tilde{w}^{(j)}) + \sum_{i\in\wp}\frac{\alpha_i}{2}\left(\tilde{w}_i^{(j)}-\hat{w}_i^{(j)}\right)^2\right\} \end{aligned} \tag{2.22}$$

where $\Im^{(j)}, \mathcal{U}^{(j)}$ represents the loading and prescribed displacement boundary conditions for the jth set of static measurement, $\hat{w}_i^{(j)}$ is the corresponding measurement displacement at point i and r_j is the weight. In what follows, specific algorithms will be elaborately designed to solve the minimization problems (2.6)-(2.22).

2.2.3 Alternating minimization (AM) method

The above sections give the theoretical view that the damaged stiffness can be identified through the minimum CRE principle. In this section, numerical algorithms for the min-CRE approach and the modified min-CRE approach are to be developed.

Min-CRE approach

In Theorem 2.2.1, the CRE function is shown to be convex and hence, separately convex on $\tilde{M}$ and $\tilde{k}$. The alternating minimization (AM) method is proposed subsequently due to the separate convexity property of the objective function. To this end, no sensitivity analysis is required herein. It is shown that the AM method could lower the computational costs associated to the minimization of the CRE objective function than the traditional direct way [29]. Actually, the AM method has been a suitable approach for minimum solution of the separately convex objective function and in principle, it tries to get the solution iteratively by alternating minimization of the objective function over every separated variable in each iteration. Specifically, given the initial stiffness $\tilde{k}_0$ as those of the intact structure, the solution is obtained successively as follows.

Firstly, minimization of the CRE function over $\tilde{M}$ yields a minimum complementary energy problem that should be solved by the force method. Therefore, the procedure is simply designated as

$$\begin{aligned}\tilde{M} =& \text{Force\_Method}(\tilde{k}, \Im, \mathfrak{U}) \\ :=& \arg\min_{\tilde{M}\in\Im} \left\{ \frac{1}{2}\int_X \frac{\tilde{M}^2}{\tilde{k}} dx - \sum_p (\theta_p \tilde{M}|_p - w_p(\tilde{M})'|_p) \right\}\end{aligned} \tag{2.23}$$

and this step is called the force-method step.

Secondly, minimization of the CRE over $\tilde{k}$ gives

$$\int_X \left\{ \frac{\tilde{M}^2}{\tilde{k}^2} - (w'')^2 \right\} \delta\tilde{k} dx = 0 \tag{2.24}$$

Practically, it is sufficient to assume that the stiffness $\tilde{k}$ is piecewise constant, that is to say,

$$\begin{aligned}& X = \cup_{i=1}^N X_i, \forall 1 \le i \ne j \le N, X_i \text{ and } X_j \text{ are non-overlapping,} \\ & \tilde{k}(x) = \{\tilde{k}_i, x \in X_i\}\end{aligned} \tag{2.25}$$

where N is the number of non-overlapping pieces, or elements. Under this circumstance, equation (2.24) is reduced to

$$\int_{X_i} \left\{ \frac{\tilde{M}^2}{\tilde{k}_i^2} - (w'')^2 \right\} \delta\tilde{k}_i dx = 0,\ i = 1, 2, \ldots, N \tag{2.26}$$

and then, one has

$$\tilde{k}_i = \sqrt{\frac{\int_{X_i} \tilde{M}^2 dx}{\int_{X_i} (w'')^2 dx}},\ i = 1, 2, ..., N \tag{2.27}$$

This step is named the UDP (update the damage parameters) step.

After integration of both of the force-method step (2.23) and the UDP step (2.27), the AM method for the min-CRE approach is established for its convenience to solve sets of equations as described in **Table 2.1**.

Table 2.1 The AM method for min-CRE approach

• Given the initial stiffness k^0 and the initial bending moment M^0, i.e. $M^0 = \text{Force\_Method}(k^0, \Im, \mathfrak{U})$
• Successively determine (k^{n+1}, M^{n+1}) from (k^n, M^n) by the following two steps,
step 1: $k_i^{n+1} = \sqrt{\dfrac{\int_{X_i} (M^n)^2 dx}{\int_{X_i} (w'')^2 dx}},\ x \in X_i,\ i = 1, 2, ..., N$
step 2: $M^{n+1} = \text{Force\_Method}(k^{n+1}, \Im, \mathfrak{U})$
• Test of convergence with given error tolerance TOL,
$\sqrt{\dfrac{\int_X (k^{n+1} - k^n)^2 dx}{\int_X (k^0)^2 dx}} + \sqrt{\dfrac{\int_X (M^{n+1} - M^n)^2 dx}{\int_X (M^0)^2 dx}} \leq \text{TOL}$

It is noteworthy that when the beam forms a statically determinate structure, such as a simply supported beam, a cantilever beam and so on, the exact bending moment is directly known. Under this circumstance, a single step in equation (2.27) would give the stiffness.

Actually, the AM method is designed for solution of the discrete version of the problem (2.20); that is

$$(M_h, k_h) = \arg \min_{\tilde{M}_h \in \Im, \tilde{k}_h \in \mathcal{C}_h} F(\tilde{M}_h, \tilde{k}_h) \tag{2.28}$$

where $\mathcal{C}_h = \{k \in \mathcal{C} : k \text{ is constant in } X_i, i = 1, 2, \ldots, N\}$ is a compact subspace of $\mathcal{C}$, with h denoting the characteristic mesh size. Finally, as closure of this subsection, the AM method will be shown to converge for problem (2.28).

Theorem 2.2.2. *Assume that the problem* (2.28) *has a unique minimizer* (M_h, k_h) *and* $F(\cdot, \cdot)$ *is strictly convex in the vicinity of* (M_h, k_h)*, then, the AM method will converge to the exact solution.*

Proof of Theorem 2.2.2.

For proof of Theorem 2.2.2, a lemma is introduced first.

Lemma 2.2.3. *Let* $f : H \to R$ *be a continuous and strictly convex function and* $u \in H$ *be its unique minimizer, where* H *is a compact Banach space with norm* $\|\cdot\|$*. Then, for an arbitrary sequence* $\{u_n\}_{n=0}^{\infty} \in H$ *satisfying* $\lim_{n\to\infty} f(u_n) = f(u)$*,one has*

$$\lim_{n\to\infty} \|u_n - u\| = 0 \tag{2.29}$$

Proof. This is obvious by contradiction. Assume that $\| u_n - u \|$ does not converge to zero; that is, there exists a positive constant ϵ such that for an arbitrary positive integer $N > 0$, there is $m \geq N$ with $\| u_m - u \| > \epsilon$.

Note that $H_\epsilon = \{v \in H : \| v - u \| \geq \epsilon\}$ is a compact subspace of H and therefore, f is also continuous and strictly convex on H_ϵ, implying that there is $u_\epsilon \in H_\epsilon$ such that

$$u_\epsilon = \arg \min_{v \in H_\epsilon} f(v) \tag{2.30}$$

By the strict convexity, one has $f(u_\epsilon) > f(u)$ and hence $f(u_m) > f(u_\epsilon) > f(u)$, contradicting with $\lim_{n\to\infty} f(u_n) = f(u)$. $\square$

From the AM method in **Table 2.1**, one has for $(M^0, k^0) \in \Im \times \mathfrak{C}_h$ and the integer $n \geq 0$

$$\begin{aligned} k^{n+1} &= \arg \min_{\tilde{k} \in \mathfrak{C}_h} F(M^n, \tilde{k}), \\ M^{n+1} &= \arg \min_{\tilde{M} \in \Im*} F(\tilde{M}, k^{n+1}) \end{aligned} \tag{2.31}$$

Then, define a sequence $\{F_n\}_{n=0}^{\infty}$ as

$$F_{2m} = F(M^m, k^m), \ F_{2m+1} = F(M^m, k^{m+1}), m \in \mathbb{N} \tag{2.32}$$

and by considering equation (2.31),one has

$$F_{2m} \geq F_{2m+1} \geq F_{2m+2} \tag{2.33}$$

Along with Theorem 2.2.1(a), it is seen that $F_n \geq 0, n = 0, 1, \ldots$ and thus, it is deduced that $\{F_n\}_{n=0}^{\infty}$ is a decreasing and bounded (from below) sequence, meaning that $\{F_n\}_{n=0}^{\infty}$ is a Cauchy sequence. Furthermore, uniqueness of the minimizer must require $(M^h, k^h) \in \Im{*}{\times}\mathfrak{C}_h$ and by Theorem 2.2.1(d), $F(\cdot, \cdot)$ is separately strictly-convex on $\Im * \times \mathfrak{C}_h$. Thus, on considering Lemma 2.2.3, one has

$$\begin{aligned} F_{2m+1} - F_{2m} \to 0 &\Rightarrow \|k^{m+1} - k^m\|_{L^2} \to 0, \\ F_{2m+2} - F_{2m+1} \to 0 &\Rightarrow \|M^{m+1} - M^m\|_{L^2} \to 0. \end{aligned} \tag{2.34}$$

By further exploiting the information in equation (2.31), one has

$$\nabla_{\tilde{k}} F(M^n, k^{n+1}) \cdot \delta\tilde{k} := \int_X \left[-\left(\frac{M^n}{k^{n+1}}\right)^2 + (w'')^2 \right] \delta\tilde{k} dx = 0 \tag{2.35}$$

and

$$\nabla_{\tilde{M}} F(M^{n+1}, k^{n+1}) \cdot \delta\tilde{M} := \int_X \left(\frac{M^{n+1}}{k^{n+1}} - w''\right) \delta\tilde{M} dx = 0 \tag{2.36}$$

By continuity, it is inferred from equations (2.34) and (2.35) that

$$\nabla_{\tilde{k}} F(M^{n+1}, k^{n+1}) \cdot \delta\tilde{k} \to F(M^n, k^{n+1}) \cdot \delta\tilde{k} = 0, \text{ as } n \to \infty. \tag{2.37}$$

Next, it is concluded from equations (2.36) and (2.37) that

$$\lim_{n\to\infty} \begin{pmatrix} \nabla_{\tilde{M}} F(M^n, k^n) \cdot \delta\tilde{M} \\ \nabla_{\tilde{k}} F(M^n, k^n) \cdot \delta\tilde{k} \end{pmatrix} = \begin{pmatrix} 0 \\ 0 \end{pmatrix} \tag{2.38}$$

By Taylor expansion at the minimizer (M_h, k_h), one can have

$$\begin{aligned} \begin{pmatrix} \nabla_{\tilde{M}} F(M^n, k^n) \cdot \delta\tilde{M} \\ \nabla_{\tilde{k}} F(M^n, k^n) \cdot \delta\tilde{k} \end{pmatrix} &= \begin{pmatrix} \nabla_{\tilde{M}} F(M_h, k_h) \cdot \delta\tilde{M} \\ \nabla_{\tilde{k}} F(M_h, k_h) \cdot \delta\tilde{k} \end{pmatrix} \\ &+ \begin{pmatrix} M^n - M_h \\ k^n - k_h \end{pmatrix}^T \cdot J(M_\xi, k_\zeta) \cdot \begin{pmatrix} \delta\tilde{M} \\ \delta\tilde{k} \end{pmatrix} \\ &= \begin{pmatrix} M^n - M_h \\ k^n - k_h \end{pmatrix}^T \cdot J(M_\xi, k_\zeta) \cdot \begin{pmatrix} \delta\tilde{M} \\ \delta\tilde{k} \end{pmatrix} \end{aligned} \tag{2.39}$$

where (M_ξ, k_ζ) is the linear interpolation between (M^n, k^n) and (M_h, k_h), $J(M_\xi, k_\zeta)$ is the Hessian matrix of $F(\cdot,\cdot)$ at (M_ξ, k_ζ). Trivially, inserting $\delta\tilde{M} = M^n - M_h$ and $\delta\tilde{k} = k^n - k_h$ into equation (2.39) and noticing the fact that $J(M_\xi, k_\zeta)$ is positive definite due to the strict convexity of $F(\cdot,\cdot)$ in the vicinity of (M_h, k_h), it eventually follows from equations (2.38) and (2.39) that

$$\lim_{n\to\infty} \|M^n - M_h\|_{L^2} = 0, \ \lim_{n\to\infty} \|k^n - k_h\|_{L^2} = 0. \tag{2.40}$$

□

The convergence theorem above is for the min-CRE approach using only one set of static measurement data, nevertheless, it can be easily extended to the min-CRE approach with more than one set of static measurements and the modified-CRE approach; these will not be specified any more. As regards the case of more than one set of static measurements, a similar algorithm to that in **Table 2.1** can be established as shown in **Table 2.2**. For more generalized mathematical proof on the convergence of the AM method, the reader is referred to [49].

Table 2.2 The AM method for min-CRE approach under multiple sets of static measurements w

---

• Given the initial stiffness k^0 and the initial bending moment $M^{(1)0}, M^{(2)0}, \dots$, i.e.

$M^{(1)0} = \text{Force\_Method}(k^0, \Im^{(1)}, \mathfrak{U}^{(1)})$,

$M^{(2)0} = \text{Force\_Method}(k^0, \Im^{(2)}, \mathfrak{U}^{(2)})$,

$\dots$

• Successively determine $(k^{n+1}, M^{(1)n+1}, M^{(2)n+1}, \dots)$ from $(k^n, M^{(1)n}, M^{(1)n}, \dots)$ by the following two steps,

step 1: $k_i^{n+1} = \{\sqrt{\dfrac{\int_{X_i} \sum_j r_j (M^{(j)n})^2 dx}{\int_{X_i} \sum_j r_j (w^{(j)\prime\prime})^2 dx}},\ x \in X_i,\ i = 1, 2, ..., N\}$

step 2: $M^{(1)n+1} = \text{Force\_Method}(k^{n+1}, \Im^{(1)}, \mathfrak{U}^{(1)})$

$M^{(2)n+1} = \text{Force\_Method}(k^{n+1}, \Im^{(2)}, \mathfrak{U}^{(2)})$

$\dots$

• Test of convergence with given error tolerance TOL,

$$\sqrt{\frac{\int_X (k^{n+1} - k^n)^2 dx}{\int_X (k^0)^2 dx}} + \sqrt{\frac{\int_X (M^{(1)n+1} - M^{(1)n})^2 dx}{\int_X (M^{(1)0})^2 dx}} + \sqrt{\frac{\int_X (M^{(2)n+1} - M^{(2)n})^2 dx}{\int_X (M^{(2)0})^2 dx}} + \dots \le \text{TOL}$$

Modified min-CRE approach

Turning to the modified CRE functional (2.21), it is found that minimization over $\tilde{k}$ would result in the same constitutive-relation step (2.27) with those in the min-CRE approach. The difference lies in the introduction of a new unknown quantity $\tilde{w}$. Minimization of the CRE functional (2.21) over $\tilde{M}$ and $\tilde{w}$ yields

$$\int_X \delta\tilde{M}\left(\frac{\tilde{M}}{\tilde{k}} - \tilde{w}''\right) dx + \int_X \delta\tilde{w}''(\tilde{k}\tilde{w}'' - \tilde{M}) dx + \sum_{i \in \wp} \alpha_i \delta\tilde{w}_i(\tilde{w}_i - \hat{w}_i) = 0 \tag{2.41}$$

where $\tilde{M} = \tilde{M}_r + \hat{M}_p$ with $\tilde{M}_r = \boldsymbol{N}_r \tilde{\boldsymbol{F}}_r$ being the bending moment produced by the unknown redundant forces $\tilde{\boldsymbol{F}}_r$ and the corresponding shape functions $\boldsymbol{N}_r$, and $\hat{M}_p = \boldsymbol{N}_p \hat{\boldsymbol{F}}_p$ the bending moment caused by the given external loads $\hat{\boldsymbol{F}}_p$ and the corresponding shape functions $\boldsymbol{N}_p$. Indeterminate structures have more unknowns that can be directly solved using equilibriums. The extra unknowns are called redundant forces $\tilde{\boldsymbol{F}}_r$. Selected external reactions are used as redundant forces $\tilde{\boldsymbol{F}}_r$ in this research. For instance, consider a beam with the left end simply supported and the right end fixed under a uniform load $\hat{\boldsymbol{F}}_p = q$, there would be one redundant force $\tilde{\boldsymbol{F}}_r$ as the support reaction force at the left end. Then, for this beam, there is $\tilde{M}_r = \boldsymbol{N}_r \tilde{\boldsymbol{F}}_r = x \cdot \tilde{\boldsymbol{F}}_r$, where x is the distance between the left end and the position of $\tilde{M}_r$, and $\hat{M}_p = \boldsymbol{N}_p \hat{\boldsymbol{F}}_p = \frac{1}{2}(xl - x^2)p$, where l is the length of beam. Based on this, equation (2.41) could be rearranged into

$$\begin{aligned}\int_X \begin{pmatrix} \delta\tilde{M}_r \\ \delta\tilde{w}'' \end{pmatrix}^T \begin{pmatrix} \frac{1}{\tilde{k}} & -I \\ -I & \tilde{k} \end{pmatrix} \begin{pmatrix} \tilde{M}_r \\ \tilde{w}'' \end{pmatrix} dx + \sum_{i\in\wp} \alpha_i \begin{pmatrix} \delta\tilde{M}_r \\ \delta\tilde{w}_i \end{pmatrix}^T \begin{pmatrix} 0 \\ \tilde{w}_i \end{pmatrix} \\ = \sum_{i\in\wp} \alpha_i \begin{pmatrix} \delta\tilde{M}_r \\ \delta\tilde{w}_i \end{pmatrix}^T \begin{pmatrix} 0 \\ \hat{w}_i \end{pmatrix} + \int_X \begin{pmatrix} \delta\tilde{M}_r \\ \delta\tilde{w}_i \end{pmatrix}^T \begin{pmatrix} -\frac{1}{\tilde{k}} \\ I \end{pmatrix} \hat{M}_p dx\end{aligned} \tag{2.42}$$

where I is the identify operator. To go further, the displacement field $\tilde{w}$ is often represented by the cubic Hermit interpolation of nodal deflections $\{w_j\}$ and slopes $\{\theta_j\}$, that is to say, for an arbitrary element e with two nodes i, j whose coordinates are $x_i < x_j$, the following approximation is adopted,

$$\tilde{w} = \begin{pmatrix} H_1 & H_2 & H_3 & H_4 \end{pmatrix} \tilde{\boldsymbol{V}}^e, \tilde{\boldsymbol{V}}^e = [w_i, \theta_i, w_j, \theta_j] \tag{2.43}$$

where the superscript e denotes the restriction into element e and the polynomial interpolation functions H_1, H_2, H_3, H_4 are of the following forms,

$$\begin{aligned}&\begin{cases} H_1(\xi) = \frac{1}{2}(\xi+2)(\xi-1)^2, H_2(\xi) = \frac{1}{4}(\xi+1)(\xi-1)^2\frac{h^e}{2}, \\ H_3(\xi) = \frac{1}{2}(2-\xi)(\xi+1)^2, H_2(\xi) = \frac{1}{4}(\xi-1)(\xi+1)^2\frac{h^e}{2}, \end{cases} \\ &h^e = x_j - x_i, \xi = \frac{2(x-x_i)}{h^e} - 1.\end{aligned} \tag{2.44}$$

For brevity, the total finite element approximation is designated as

$$\tilde{w} = \boldsymbol{H}\tilde{\boldsymbol{V}} \tag{2.45}$$

where $\boldsymbol{H}$ forms the finite element space and $\tilde{\boldsymbol{V}}$ collects all the displacement DOFs.

Above all, equation (2.42) can yield,

$$
\begin{aligned}
&\begin{pmatrix} \boldsymbol{S} & -\boldsymbol{C} \\ -\boldsymbol{C}^T & \boldsymbol{K} \end{pmatrix} \begin{pmatrix} \tilde{\boldsymbol{F}}_{\boldsymbol{r}} \\ \tilde{\boldsymbol{V}} \end{pmatrix} = \begin{pmatrix} \boldsymbol{a} \\ \boldsymbol{b} \end{pmatrix} \\
&\boldsymbol{S} = \int_X \boldsymbol{N}_r^T \frac{1}{k} \boldsymbol{N}_r dx \\
&\boldsymbol{K} = \int_X \boldsymbol{H}''^T k \boldsymbol{H}'' dx + \boldsymbol{\alpha}, \boldsymbol{\alpha} \text{ a diagonal matrix with } \boldsymbol{\alpha}(i,i) = \begin{cases} \alpha_i, i \in \wp \\ 0, i \notin \wp \end{cases} \\
&\boldsymbol{C} = \int_X \boldsymbol{N}_r^T \boldsymbol{H}'' dx \\
&\boldsymbol{a} = -\int_X \boldsymbol{N}_r^T \frac{1}{k} \tilde{M}_r dx, \boldsymbol{b} = \int_X \boldsymbol{H}''^T \hat{M}_p dx + \boldsymbol{p}, \boldsymbol{p}(i) = \begin{cases} \alpha_i \hat{w}_i, i \in \wp \\ 0, i \notin \wp \end{cases}
\end{aligned}
\tag{2.46}
$$

This step is called the UMF (update the mechanical field) step which is designated to recover full-field displacement and bending moment data from incomplete finite-point displacement data. For simplicity, this step is designated as $(M, w) = \text{recovery}(\tilde{k}, \Im, \mathfrak{U}, \{\hat{w}_i, i \in \wp\})$.

As a consequence, a new AM method (to that in **Table 2.1** or **Table 2.2**) for the modified min-CRE approach with multiple sets of measurement data can be established in **Table 2.3**.

2.3 Numerical verification

To show the effectiveness of the proposed damage identification approach, four beams are studied. They are a propped cantilever beam, a simply supported beam, a three-span continuous beam and a plane frame respectively. For application of the AM method (in **Table 2.1**, **Table 2.2** and **Table 2.3**), the convergence tolerance is practically set to TOL$= 1 \times 10^{-6}$.

2.3.1 Propped cantilever beam

A propped cantilever beam of continuously varying stiffness $k(x) = k_0(1 + x/L)^2$ with $k_0 = 1$ (see **Figure 2.2**) is studied in this example to examine the capacity and identifiability of the proposed min-CRE approach for damage identification in general beams.

Table 2.3 The AM method for the modified min-CRE approach under multiple sets of static measurements w

• Given the initial stiffness k^0, the initial displacements $w^{(1)0}, w^{(2)0}, \ldots$ and the initial bending moment $M^{(1)0}, M^{(2)0}, \ldots$, i.e. $(M^{(1)0}, w^{(1)0}) = \mathrm{recovery}(k^0, \Im^{(1)}, \mathfrak{U}^{(1)}, \{\hat{w}_i^{(1)}, i \in \wp\})$, $(M^{(2)0}, w^{(2)0}) = \mathrm{recovery}(k^0, \Im^{(2)}, \mathfrak{U}^{(2)}, \{\hat{w}_i^{(2)}, i \in \wp\})$, $\ldots$ • Successively determine $(k^{n+1}, M^{(j)n+1}, w^{(j)n+1})$ from $(k^n, M^{(j)n}, w^{(j)n})$ by the following two steps, step 1: $k_i^{n+1} = \left\{ \sqrt{\frac{\int_{X_i} \sum_j r_j (M^{(j)n})^2 dx}{\int_{X_i} \sum_j r_j (w^{(j)n''})^2 dx}},\ x \in X_i,\ i = 1, 2, ..., N \right\}$ step 2: $(M^{(1)n+1}, w^{(1)n+1}) = \mathrm{recovery}(k^{n+1}, \Im^{(1)}, \mathfrak{U}^{(1)}, \{\hat{w}_i^{(1)}, i \in \wp\})$, $(M^{(2)n+1}, w^{(2)n+1}) = \mathrm{recovery}(k^{n+1}, \Im^{(2)}, \mathfrak{U}^{(2)}, \{\hat{w}_i^{(2)}, i \in \wp\})$, $\ldots$ • Test of convergence with given error tolerance TOL, $\sqrt{\frac{\int_X (k^{n+1} - k^n)^2 dx}{\int_X (k^0)^2 dx}} + \sqrt{\frac{\int_X (M^{(1)n+1} - M^{(1)n})^2 dx}{\int_X (M^{(1)0})^2 dx}} + \sqrt{\frac{\int_X (M^{(2)n+1} - M^{(2)n})^2 dx}{\int_X (M^{(2)0})^2 dx}} + \ldots$ $+ \sqrt{\frac{\int_X (w^{(1)n+1} - w^{(1)n})^2 dx}{\int_X (w^{(1)0})^2 dx}} + \sqrt{\frac{\int_X (w^{(2)n+1} - w^{(2)n})^2 dx}{\int_X (w^{(2)0})^2 dx}} + \ldots \leq \mathrm{TOL}$

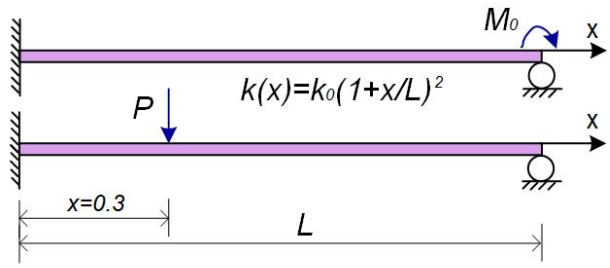

Figure 2.2 Geometry and loads for a propped cantilever beam

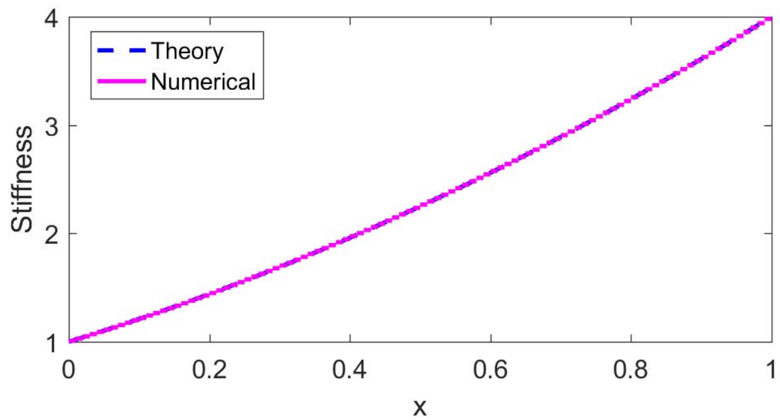

Figure 2.3 Damage identification in propped cantilever beam using two sets of static measurements

The geometric parameter is $L = 1$. Two sets of static measurements are used: a concentrated moment $M_0 = 1$ at the right end and a unit concentrated force at $x = 0.3$. The beam is uniformly partitioned into 100 elements and each node's displacement is obtained directly from analytical solution.

The algorithm in **Table 2.2** is adopted with an initial stiffness being $k^0(x) = 1$. Eventually, the piecewise constant stiffness can be identified as exhibited in **Figure 2.3**. As we can see, the stiffness can be well identified.

In addition, to show the convergence of the proposed min-CRE approach, the bending moment at the left end of the beam $M(x = 0)$ is observed at each iteration step. Detailed results are displayed in **Figure 2.4**. It is seen that the bending moment converges only after 20 iterations, verifying the convergence of the AM method.

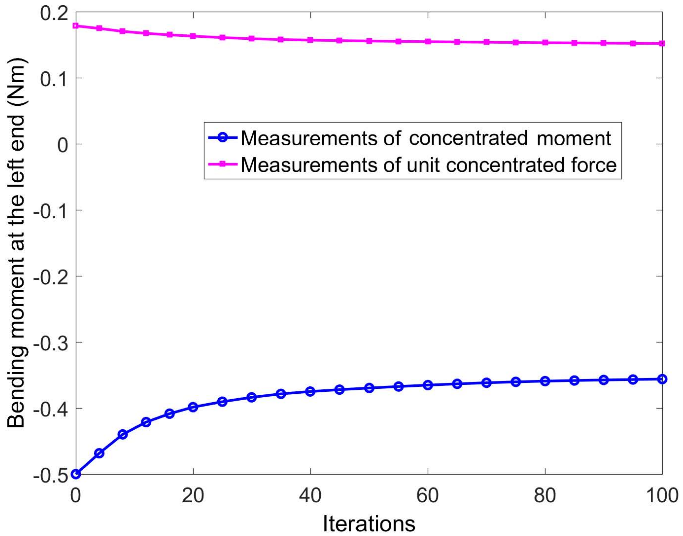

Figure 2.4 Convergence of bending moment at left end of propped cantilever beam

2.3.2 Three-span continuous beam

Damage in an equi-spaced three-span continuous and statically indeterminate beam (see **Figure 2.5**) is to be identified in this example. Length of each span is $L = 2$m and the stiffness of the intact beam over the whole beam is $k^0 = 8.33 \times 10^4$Nm^2. In this numerical test, measurement points are so distributed that each span is uniformly partitioned into four elements and the specific enumeration of points and elements are also shown in **Figure 2.5**.

Two damage cases are taken into account, including:

- Large damage case D1: stiffness reduced to 60%, 40% and 80% in elements 1, 4 and 10, respectively; and
- Small damage case D2: stiffness reduced to 95%, 90% and 85% in elements 1, 4 and 10, respectively.

To enhance the identifiability of the algorithm, nine sets of load cases are considered and for each case, a concentrated force is enforced on one of the nodes 2-4, 6-8 and 10-12. Accordingly, nine sets of static displacements at the same nine points are measured. This kind of measurement can often be seen in damage detection of bridges for which a moving truck (or load) is used to generate the multiple load cases.

The simulated displacement data is acquired through finite element computation. A uniform distribution noise is added to the simulated response as

$$\text{noise}(x) = uniform \cdot a \tag{2.47}$$

where $uniform$ is a number pertains to the uniform distribution in the range $[-1, 1]$ and a is the applied noise level. Noises of levels 0.05mm, 0.1mm and 0.2mm (relatively $0.5\%, 1\%, 2\%$ to the maximum displacement response) are considered in this example. For the sake of convenience, the Damage Index (DAI) is introduced to represent the scaled damage in the beam, i.e.

$$\text{DAI}_i = k_i^{damage}/k_i^0 \tag{2.48}$$

for the ith element where k_i^{damage} is the damaged stiffness in element i.

By performing the iterative algorithm in **Table 2.3** with the initial stiffness setting to the stiffness of the intact beam, the modified min-CRE approach for damage identification can proceed. Good identification performance for the statically indeterminate structure is achieved when the measurement noise is not greater than 0.2mm in the large damage case and 0.1mm in the small damage case as shown in **Figure 2.6**. To visualize the convergence of the algorithm for large damage case D1, detailed results on the damage indices (see equation (2.48) at each iteration step under 0.05mm noise are given in **Figure 2.7**. Obviously, all the quantities converge within 200 iterations verifying the convergence of the proposed AM method. The displacement fields for the large damage case D1 are also rebuilt based on this approach. As can be seen from **Figure 2.8**, the 'uncertainties' due to the 0.2mm noise in the discrete displacement boundary are much more overcome in these superior rebuilt fields, resulting in good identification for the damage.

2.3.3 Plane frame structure

A plane frame structure as shown in **Figure 2.9**(a) is to be studied to demonstrate the robustness of the proposed min-CRE approach. The axial displacement u_x and tension force N are additionally considered in this case. The damage parameter is set to be $E(x)$ instead of $EI(x)$. The height and width of the frame are $H = L \times 2 = 8$m and $L = 4$m, respectively, with the inertial moment for planar bending $I = 5 \times 10^{-9}\text{m}^4$ and cross-sectional area $A = 1 \times 10^{-7}\text{m}^2$. For the undamaged frame, the Young's modulus

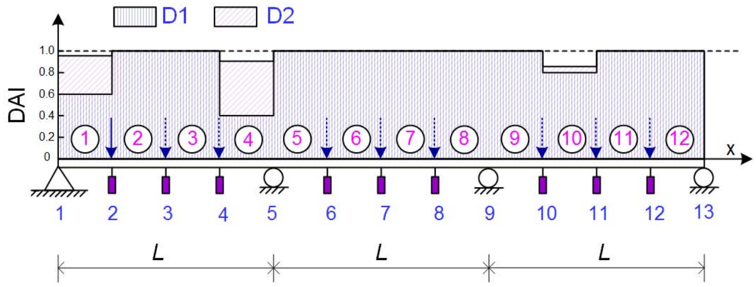

Figure 2.5 Geometry, damage location and load cases of three-span continuous beam (D1-damage case 1, D2-damage case 2)

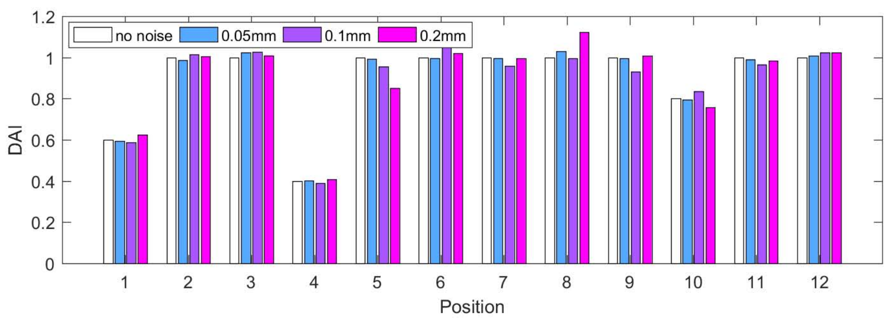

(a) large damage case D1

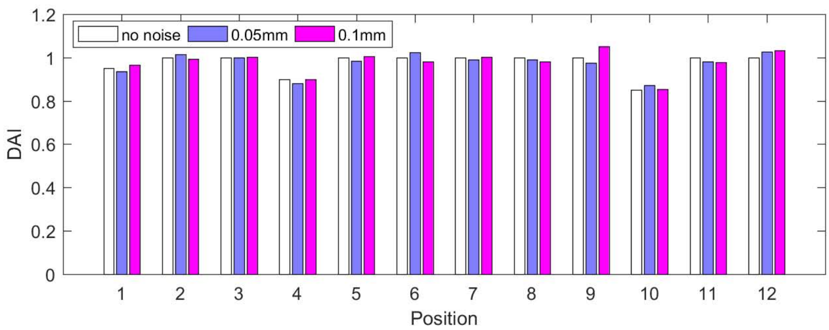

(b) small damage case D2

Figure 2.6 Damage identification with measurement noises of three-span continuous beam

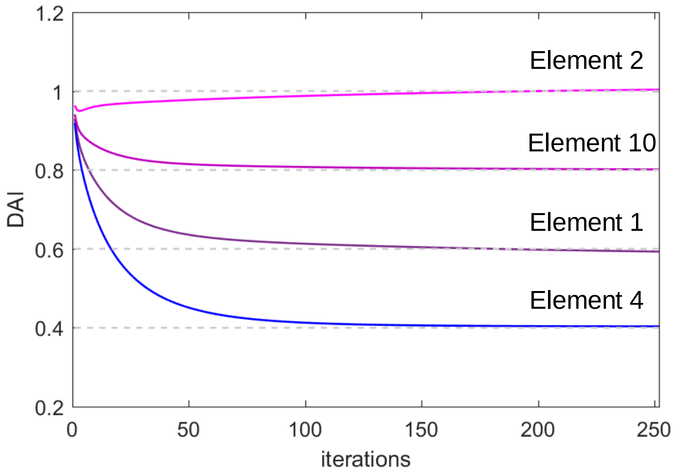

Figure 2.7 Convergence of the damage indices of three-span continuous beam under D1

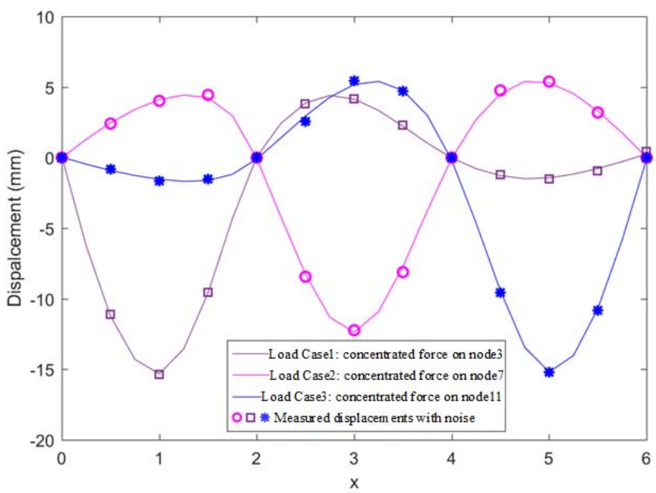

Figure 2.8 Displacement fields rebuilt by modified min-CRE approach comparing to the measured displacements with noises

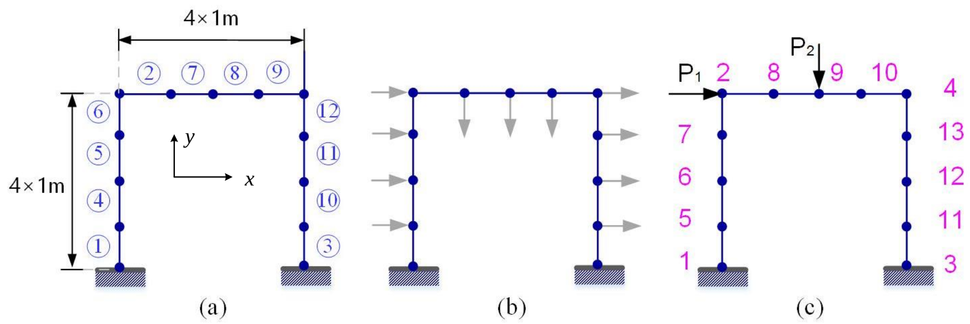

Figure 2.9 Geometry, measurement points and load cases of plane frame structure

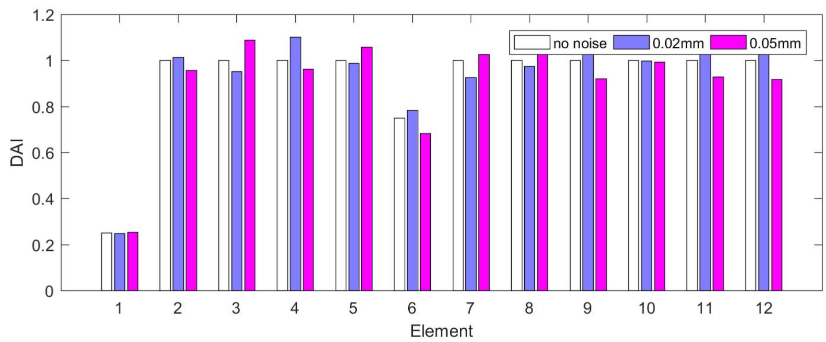

Figure 2.10 Damage identification with measurement noise of plane frame

is $E = 2 \times 10^8$N/m. The plane frame consists of 12 Euler-Bernoulli beam elements with 13 nodes, each with three degrees of freedom. The displacement measurement locations and corresponding direction are illustrated in **Figure 2.9**(b). Damages were enforced by reducing the Young's modulus E to 25% in element 1 and 75% in element 6. Two sets of load cases are considered: a unit concentrated force P_1 at node 2 in x direction and P_2 at node 9 in negative y direction (**Figure 2.9**(c)). The uniform distribution noise described in equation (2.48) is used and noises of level 0.02mm and 0.05mm are considered in this example.

As shown in **Figure 2.10**, the good identification performance is achieved for the damage scenario even under the noise of level 0.05mm.

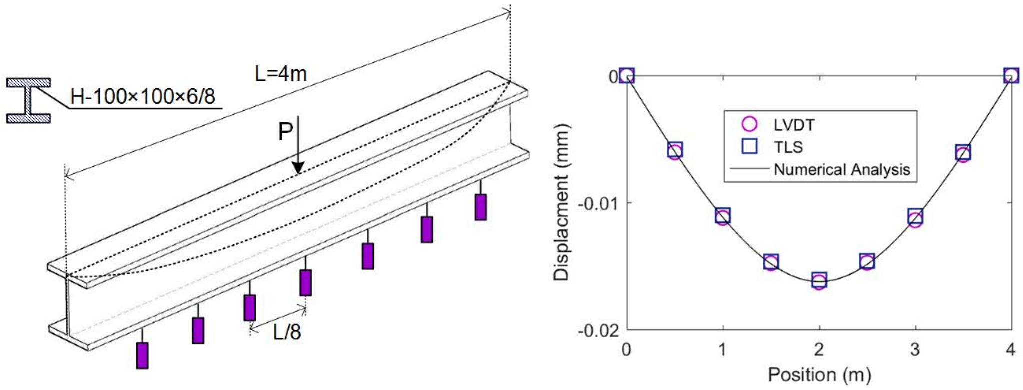

Figure 2.11 Geometry and experimental displacements of simply supported beam

2.4 Experimental verification

2.4.1 Simply supported experimental beam

In this example, experimental finite-point measurements are used for stiffness identification to testify the applicability of the modified min-CRE approach. The beam model is taken from the experimental bending test in [50]. Parameters of the experimental uniform beam are: length $L = 4$m, Young's modulus $E = 206$GPa and the $H - 100 \times 100 \times 6/8$ section with depth of 100mm, flange width of 100mm, web thickness of 6mm and flange thickness of 8mm. Only one load case is enforced in the experiment with a concentrated force $P = 9.66$kN at the middle point of the beam as shown in **Figure 2.11**. Experimental displacements attained by respective the linear variable-differential transformers (LVDT) and the Terrestrial Laser Scanning (TLS) [50] are shown in **Figure 2.11**.

Using these displacement data, the distributive stiffness of the beam can be identified by the modified min-CRE approach and detailed results are presented in **Figure 2.12**. The value of the initial uniform inertial moment is set to 400cm^4. Obviously, the distributive stiffness is well identified with respect to the beam's theoretical inertial moment 383cm^4 (**Figure 2.12**); the relative errors are less than 3% for both the LVDT data and the TLS data.

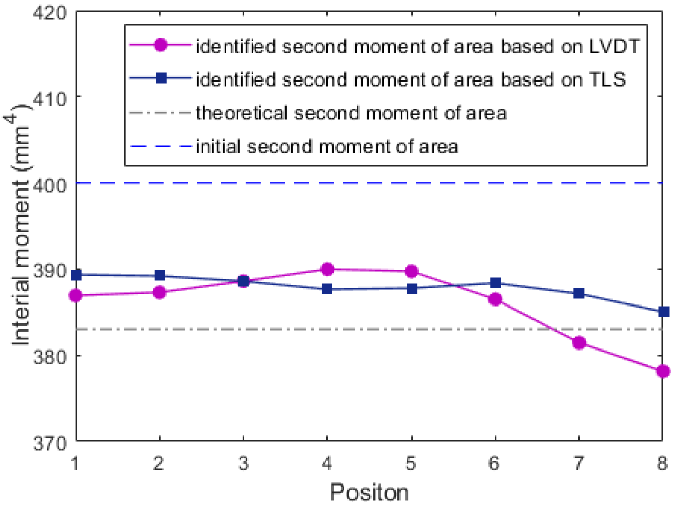

Figure 2.12 Inertial moment identified by modified min-CRE approach comparing to the theoretical inertial moment of simply supported beam

2.5 Conclusions

Two new approaches based on the minimum constitutive relation error (CRE) principle have been proposed for static damage identification in Euler-Bernoulli beams, i.e. the min-CRE approach for full-field measurements and the modified min-CRE approach for finite-point measurements, respectively. The difference between the two approaches is whether to use additional penalty terms for enforcement of the experimental displacement data or not. The robustness of these approaches could be guaranteed by applying multiple sets of static measurements. Numerical tests have been carried out to verify these approaches. The sound performance of these proposed approaches in the following aspects have been observed:

1. The convexity of the CRE function has been proved and this guarantees the existence of the minimizer to the identification problem.

2. For full-field displacement measurements, the CRE functional is directly treated as the objective functional while in case of finite-point measurement data, the CRE functional along with additional penalty terms for treatment of the finite-point displacement measurements is defined as the objective functional.

3. Multiple loads and associated sets of measurements could improve the identifiability and robustness of the procedure.

4. The alternative minimization (AM) method has been established to fulfil the practical implementation and its convergence has been proved.

5. The approaches are well applicable to both statically determinate and indeterminate beam structures for stiffness/damage identification and bending moment reconstruction.

6. Even large damage could be well identified.

7. The approaches perform well under measurement noise.

8. The approaches converge well in practice.

Therefore, it is believed that the proposed approach can serve as an effective tool for practical structural damage identification.

3

Damage identification using modal data

3.1 Problem statement

3.1.1 Baseline model

Consider an Euler-Bernoulli beam occupying the physical domain $x \in X$. Let $(u_i(x)$,$\theta_i(x))$ denote the deflection and rotation of the ith mode shape and $M_i(x), Q_i(x)$ the corresponding bending moment and shear force. The flexural stiffness and mass per unit length are denoted by EI and ρA as shown in **Figure 3.1**. The support displacements satisfy the homogeneous Dirichlet boundary conditions, or mathematically $u_i(x) \in \mathfrak{U}_0$, $\mathfrak{U}_0 = \{u_i \in H^2(X) : u_i$ satisfy the homogeneous Dirichlet boundary conditions$\}$ and $(M_i(x), Q_i(x))$ satisfy the homogeneous Neumann boundary conditions, or mathematically $M_i(x) \in \Im_0$, $\Im_0 = \{M_i'' \in L^2(X) : M_i$ satisfy the homogeneous Neumann boundary conditions$\}$. As is noteworthy, H^2 is the Sobolev space defined with the derivatives up to the second order being square-integrable and it is usually known as containing the C^1-continuous functions and L^2 is the Lebesgue space of square-integrable functions. With these notations, the free vibration of the Euler-Bernoulli beam is divided into three parts.

- **Kinematic constraints**

$$u_i(x) \in \mathfrak{U}_0 \tag{3.1}$$

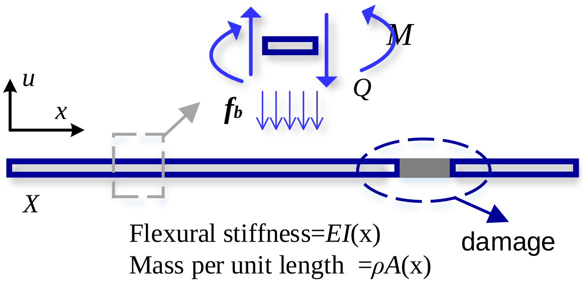

Figure 3.1 Model of Euler-Bernoulli beam

- **Equilibrium equations**

$$f_{bi}(x) + M_i''(x) = 0 \tag{3.2}$$

where $f_{bi}(x)$ is the transversal inertial force per unit length and $M_i(x) \in \Im_0$. Moreover, the equilibrium equations as well as the boundary conditions (by principle of virtual work) could also be expressed as

$$\int_x f_{bi}(x)\delta u_i dx + \int_x M_i(x)\delta u_i'' dx = 0, \forall \delta u_i \in \mathcal{U}_0. \tag{3.3}$$

- **Constitutive relations**

$$M_i(x) = EIu_i''(x)\text{—Hooke's law,} \tag{3.4a}$$

$$f_{bi}(x) = \rho A\ddot{u}_i(x)\text{—Newton's law.} \tag{3.4b}$$

By the use of the relations $\ddot{u}_i(x) = -\omega_i^2 u_i(x)$ in free vibration analysis, where ω_i is the ith circular natural frequency, equation (4b) could be simplified as $f_{bi}(x) = -\omega_i^2 \rho A u_i(x)$.

3.1.2 CRE function for a given mode

To define the constitutive relation error for the ith mode shape, consider an admissible displacement solution $\mathcal{W}_i = u_i(x) \in \mathcal{U}_0$, an admissible force solution $\mathcal{F}_i = M_i(x) \in \Im_0$ which satisfies equilibrium equations (3.2) and the admissible structural parameters $\mathcal{K} \in \mathcal{C}$ which may include some model's parameters such as Young's modulus, mass density and cross-section information of the beam. It is easily known that, if the constitutive relation (3.4) is additionally satisfied, the above solution would be the exact eigenmodes of this structure.

As a result, to measure the distance of the admissible solutions to the exact solutions in the energy product, the constitutive relation error for the ith mode of the beam is defined by

$$e_{CRE}(\mathcal{W}_i, \mathcal{F}_i, \mathcal{K}) = \frac{r}{2}\int_X \frac{(M_i - EIu_i'')^2}{EI}dx + \frac{1-r}{2}\int_X \frac{(f_{bi} + \omega_i^2\rho A u_i)^2}{\omega_i^2\rho A}dx \tag{3.5}$$

where $r \in [0, 1]$ is the corresponding weight which depends on the relative reliability between the constitutive relation (3.4) based on the *Hooke's law* and based on the *Newton's law* and is fixed to be $r = 0.5$ in this paper.

For this free vibration problem, further considering the equilibrium equations (3.2), the CRE in (3.5) could be simplified into:

$$e_{CRE}(\mathcal{W}_i, \mathcal{F}_i, \mathcal{K}) = \frac{r}{2}\int_X \frac{(M_i - EIu_i'')^2}{EI}dx + \frac{1-r}{2}\int_X \frac{(M_i'' - \omega_i^2\rho A u_i)^2}{\omega_i^2\rho A}dx \tag{3.6}$$

Then the parameter identification formulation based on the given complete mode data u_i is established as:

$$\begin{aligned} &F_i(\mathcal{W}_i, \mathcal{F}_i, \mathcal{K}) := e_{CRE}(\mathcal{W}_i, \mathcal{F}_i, \mathcal{K}) \\ &(\mathcal{F}_i, \mathcal{K}) = \arg\min_{\mathcal{F}\in\Im_0, \mathcal{K}\in\mathcal{C}} F_i(\mathcal{W}_i, \mathcal{F}_i, \mathcal{K}) \end{aligned} \tag{3.7}$$

which is known as the min-CRE principle for inverse identification problems and $F_i(\mathcal{W}_i, \mathcal{F}_i, \mathcal{K})$ is the objective function.

In many situations, the complete or full-field mode data u_i is often hardly available, rather, the incomplete modal displacement data measured by finite sensors is obtained. Herein, an additional penalty term is incorporated into the constitutive relation error function (3.7) in order to simply enforce the conditions of the measured data. Such a penalty term can also account for the different level of reliability or measurement noise of the experimental measurement data. More specially, the objective function for damage identification using the ith mode data is modified as follows

$$\hat{F}_i(\mathcal{W}_i, \mathcal{F}_i, \mathcal{K}) := e_{CRE}(\mathcal{W}_i, \mathcal{F}_i, \mathcal{K}) + \sum_{k\in\wp} \frac{\alpha_k}{2}\left(u_{ki} - \hat{u_{ki}}\right)^2 \tag{3.8}$$

where $\{\hat{u_{ki}}, k \in \wp\}$ is the measured displacement modal data on the set of points $\{k \in \wp\}$ and u_{ki} is the admissible modal displacement at kth position for the ith mode. Values of $\{\alpha_k > 0, k \in \wp\}$ could be tuned according to the confidence of the corresponding displacement data: $\{\alpha_k \to +\infty\}$ means completely trust of this data, while $\{\alpha_k \to 0\}$ means completely untrust.

3.1.3 CRE function for multiple modes

In order to identify the damage parameters, multiple modal data $\{(u_{ki}, \omega_i), i \in S\ k \in \wp\}$ are often measured, where S denotes the set of all modal data. The objective function (CRE function) for multiple modes is defined as follows

$$F(\mathcal{W}, \mathcal{F}, \mathcal{K}) = \sum_{i \in S} t_i \hat{F}_i(\mathcal{W}_i, \mathcal{F}_i, \mathcal{K}) = \sum_{i \in S} t_i \left(e_{CRE}(\mathcal{W}_i, \mathcal{F}_i, \mathcal{K}) + \sum_{k \in \wp} \frac{\alpha_k}{2} |u_{ki} - \hat{u}_{ki}|^2 \right) \tag{3.9}$$

where t_i is the corresponding weight coefficient and $\mathcal{W} = \{\mathcal{W}_i, i \in S\}, \mathcal{F} = \{\mathcal{F}_i, i \in S\}$. Herein, the weight coefficient t_i should be chosen based on the reliability of each mode.

3.2 Damage identification by min-CRE and sparse regularization

Section 3.1 presents the basic background of the min-CRE principle for beam structures. In practice, the amount of the measured modal data is always limited and this may make the damage identification problem ill-posed. To properly circumvent the ill-posedness, the sparse regularization technique is reasonably introduced and the AM method is proposed to practically solve the nonlinear optimization problem in this section. Particular attention is paid to estimation of the regularization parameters for the sparse regularization.

3.2.1 AM method

- step 1 (UMF Step): Update the mechanical field $(\mathcal{W}_i, \mathcal{F}_i)$ for the ith mode with the given material parameters $\mathcal{K}^n$

$$(\mathcal{W}_i^{n+1}, \mathcal{F}_i^{n+1}) = \arg \min_{\mathcal{W} \in \mathcal{U}_0, \mathcal{F} \in \Im_0} \hat{F}(\mathcal{W}_i, \mathcal{F}_i, \mathcal{K}^n), i \in S. \tag{3.10}$$

- step 2 (UDP Step): Update the damage parameters or stiffness $\mathcal{K}$ based on the mechanical fields $(\mathcal{W}_i^{n+1}, \mathcal{F}_i^{n+1})$ obtained in step 1.

$$\mathcal{K}^{n+1} = \arg\min F(\mathcal{W}^{n+1}, \mathcal{F}^{n+1}, \mathcal{K}) = \arg \min_{\mathcal{K} \in \mathcal{C}} \left(\sum_{i \in S} t_i \hat{F}(\mathcal{W}_i^{n+1}, \mathcal{F}_i^{n+1}, \mathcal{K}) \right). \tag{3.11}$$

UMF Step

The mechanical field $(\mathcal{W}_i, \mathcal{F}_i)$ is recovered from the measured data and the given stiffness matrix $\mathcal{K}$ individually for every mode. The sparse regularization term is not involved in this step. Specifically, the minimization over $\mathcal{F}_i$ yields the equation:

$$\int_x \left\{ r\frac{\delta M_i M_i}{EI} + (1-r)\frac{\delta M_i'' M_i''}{\omega_i^2 \rho A} - \delta M_i'' u_i) \right\} dx = 0,\ \forall \delta M_i \in \Im_0 \tag{3.12}$$

and the minimization over $\mathcal{W}_i$ yields

$$\int_x \{rEI\delta u_i'' u_i'' + (1-r)\omega_i^2 \rho A \delta u_i u_i - \delta u_i M_i''\} dx + \sum_{k\in\wp} \alpha_i \delta u_{ki}\left(u_{ki} - \hat{u}_{ki}\right) = 0,\ \forall \delta u_i \in \mathcal{U}_0 \tag{3.13}$$

From equations (3.12) and (3.13), the mechanical field $(\mathcal{W}_i, \mathcal{F}_i)$ can be updated simultaneously. Practically, equations (3.12) and (3.13) are dealt with in the finite element setting as follows.

A finite dimensional space $\Im_0^h \subset \Im_0$ and $\mathcal{U}_0^h \subset \mathcal{U}_0$ are constructed at first with h denoting the characteristic mesh size. For each mode, the nodal forces (Q_i, M_i) and displacements (θ_i, u_i) at an arbitrary node i are naturally selected as the basic DOFs to solve the admissible force solution and displacement solution, respectively. Then, for an arbitrary element e with two nodes i, j whose coordinates are $x_i < x_j$, the following approximation (Q_h, M_h) and (θ_h, u_h) are adopted for the force and displacement finite element computation,

$$\begin{aligned} M_h^e &= \begin{pmatrix} H_1 & H_2 & H_3 & H_4 \end{pmatrix} \boldsymbol{F}^e, \boldsymbol{F}^e = [Q_i, M_i, Q_j, M_j] \\ u_h^e &= \begin{pmatrix} H_1 & H_2 & H_3 & H_4 \end{pmatrix} \boldsymbol{W}^e, \boldsymbol{W}^e = [\theta_i, u_i, \theta_j, u_j] \end{aligned} \tag{3.14}$$

where the superscript e denotes the restriction into element e and the polynomial interpolation functions H_1, H_2, H_3, H_4 are of the following forms,

$$\begin{aligned} &\begin{cases} H_1(\xi) = \frac{1}{2}(\xi+2)(\xi-1)^2, H_2(\xi) = \frac{1}{4}(\xi+1)(\xi-1)^2\frac{h^e}{2}, \\ H_3(\xi) = \frac{1}{2}(2-\xi)(\xi+1)^2, H_4(\xi) = \frac{1}{4}(\xi-1)(\xi+1)^2\frac{h^e}{2}, \end{cases} \\ &h^e = x_j - x_i, \xi = \frac{2(x-x_i)}{h^e} - 1. \end{aligned} \tag{3.15}$$

For brevity, the total finite element approximation is designated as

$$M_h = \hat{\boldsymbol{\Phi}}\boldsymbol{F}, u_h = \boldsymbol{\Phi}\boldsymbol{W} \tag{3.16}$$

where $\boldsymbol{F}$ and $\boldsymbol{W}$ collect all the DOFs with *a priori* satisfaction of the Neumann boundary condition and Dirichelet boundary condition respectively. For a complete exposition of the displacement and fore based beam element, the reader is referred to the **Appendix** A. Using the finite element approximation (3.16), the discrete formulation of equations (3.12) and (3.13) is obtained

$$\begin{aligned}
&\begin{pmatrix} \boldsymbol{A}_0 & -\boldsymbol{C}_0 \\ -\boldsymbol{C}^T{}_0 & \boldsymbol{B}_0 \end{pmatrix} \begin{pmatrix} \boldsymbol{F} \\ \boldsymbol{W} \end{pmatrix} = \begin{pmatrix} \boldsymbol{a} \\ \boldsymbol{b} \end{pmatrix} \\
&\boldsymbol{A} = \int_X \left\{ r\frac{\hat{\boldsymbol{\Phi}}^T\hat{\boldsymbol{\Phi}}}{EI} + (1-r)\frac{\hat{\boldsymbol{\Phi}}^{T''}\hat{\boldsymbol{\Phi}}''}{\omega^2\rho A} \right\} dx \\
&\boldsymbol{B} = \int_X \{ r\boldsymbol{\Phi}^{T''} EI \boldsymbol{\Phi}'' + (1-r)\boldsymbol{\Phi}^T\omega^2\rho A\boldsymbol{\Phi} \} dx + \boldsymbol{P} \\
&\boldsymbol{P} \text{ a diagonal matrix with } \boldsymbol{P}(k,k) = \begin{cases} \alpha_k, k \in \wp \\ 0, k \notin \wp \end{cases} \\
&\boldsymbol{C} = \int_X \hat{\boldsymbol{\Phi}}''^{\mathrm{T}} \boldsymbol{\Phi} dx \\
&\boldsymbol{a} = \boldsymbol{0}, \boldsymbol{b} = \boldsymbol{p}, \boldsymbol{p}(k) = \begin{cases} \alpha_k \hat{u}_k, k \in \wp \\ 0, k \notin \wp \end{cases}
\end{aligned} \tag{3.17}$$

where $\boldsymbol{A}_0$,$\boldsymbol{B}_0$ and $\boldsymbol{C}_0$ are the reduced forms of $\boldsymbol{A}$,$\boldsymbol{B}$ and $\boldsymbol{C}$ after applying the homogeneous boundary conditions.

UMP Step

The damage parameters for the Euler-Bernoulli beam structure in this paper is set to be $\mathcal{K} = EI(x)$ and, the sparse regularization term is involved and needs to be properly tackled. The sparsity assumption that the number of damage locations of a structure is as few as possible is sensible for the practical damage identification problem. Properly enforcing the sparsity assumption could improve the robustness of the identification results [51] and this shall be easily reached by the sparsity regularization technique as mentioned in Chapter 1.

Assume that the stiffness EI is piecewise constant, that is to say $EI(x) = \{EI_p, x \in X_p, p = 1, 2, ..., N\}$, where $\{X_p, p = 1, 2, ..., N\}$ is the non-overlapping decomposition of the whole domain X. Then, with the sparse regularization, the objective function is reformulated as

$$\begin{aligned} L_1 = & \textstyle\sum_{i\in S} \int_{X_p} t_i \Big\{ \frac{r}{2} \frac{(M_i - EI_p u_i'')^2}{EI_p} + \frac{1-r}{2} \frac{(M_i'' - \omega_i^2 \rho A u_i)^2}{\omega_i^2 \rho A} \Big\} dx \\ & + \lambda l_p \parallel EI_p - EI_{0p} \parallel_1^1, \; p = 1, 2, ..., N \end{aligned} \tag{3.18}$$

where $\{l_p, p = 1, 2, ..., N\}$ is the length of EI_p and EI_{0p} is set to be the stiffness of the structure before damage. $\parallel EI_p - EI_{0p} \parallel_1^1$ is the sparse regularization term with $\|x\|_1 = |x|$ being the ℓ_1-norm. $\lambda > 0$ is the regularization parameter which controls the trade-off between the sparsity and the residual norm. Furthermore, the partial differential equation of equation (3.18) for $\{EI_p, x \in X_p, p = 1, 2, ..., N\}$ takes the form

$$\frac{\partial L_1}{\partial EI} = \sum_{i\in S} \int_{X_p} t_i r \Big\{ \frac{M_i^2}{{EI_p}^2} - (u_i'')^2 \Big\} dx - \lambda l_p \{\text{sign}(EI_p - EI_{0p})\} dx = 0. \tag{3.19}$$

Finally, one has

$$EI_p = \begin{cases} \sqrt{\dfrac{b_p}{a_p + \lambda l_p}} \text{ , if } \lambda < \Lambda_p \\ \sqrt{\dfrac{b_p}{a_p - \lambda l_p}} \text{ , if } \lambda < -\Lambda_p \\ EI_{0p} \text{ , if } \lambda \geq |\Lambda_p| \end{cases}, \; p = 1, 2, ..., N \tag{3.20}$$

where

$$\Lambda_p = \frac{1}{l_p} \sum_{i\in S} \int_{X_p} t_i r \Big\{ \frac{M_i^2}{{EI_{0p}}^2} - (u_i'')^2 \Big\} dx = \frac{1}{l_p} \left(\frac{b_p}{EI_{0p}^2} - a_p \right) \tag{3.21}$$

and

$$a_p = \sum_{i\in S} \int_{X_p} t_i r (u_i'')^2 dx, \; b_p = \sum_{i\in S} \int_{X_p} t_i r M_i^2 dx \tag{3.22}$$

Datailed explanations of Λ_p are discussed in the next section. From equations (3.19) and (3.20), the sparse regularization term would introduce little computational complexity and the minimization over the damage parameters along with the sparse regularization term is solved immediately by the closed-form solution in equation (3.20) for the sparse-regularized min-CRE approach. However, in the sensitivity-based approaches[51], the sparse regularization term in each sensitivity step must be dealt with in a costly manner by iterative algorithms, e.g., the linear programming method or the interior point method. Moreover, no sensitivity analysis is involved in the proposed approach. All of these have constituted the advantages of the proposed min-CRE approach

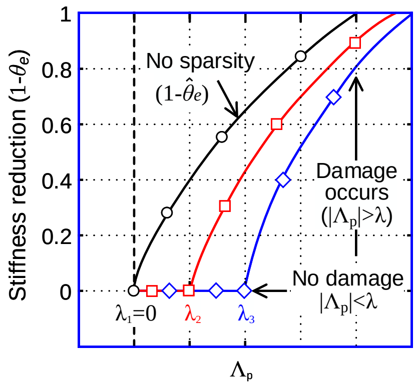

Figure 3.2 Sparsity with different valuses of λ

over the conventional sensitivity-based approaches, due to the employment of the AM method.

To get a better perspective of equation (3.20) and the sparsity-promoting nature of ℓ_1-norm regularization, $\hat{EI}_p$ (dotted line in **Figure 3.2**) is introduced for the situation when no sparsity is considered ($\lambda = 0$)

$$\hat{EI}_p = \sqrt{\frac{\sum_i \int_{X_p} t_i M_i^2 dx}{\sum_i \int_{X_p} t_i (u_i'')^2 dx}} = \sqrt{\frac{b_p}{a_p}}, \; p = 1, 2, ..., N \tag{3.23}$$

Based on equations (3.20) and (3.23), **Figure 3.2** illustrates the relationship between EI_p and $\hat{EI}_p$ with different values of λ_i ($i = 1, 2, 3$). As it is shown, the value of EI_p is prone to be unchanged from the initial value EI_{0p} when $\lambda \geq |\Lambda_p|$ while EI_p begins to deviate from EI_{0p} to $\hat{EI}_p$ when $\lambda < |\Lambda_p|$. EI_p is equal to $\hat{EI}_p$ when $\lambda_1 = 0$ (red line in **Figure 3.2**). Besides, when $\lambda_3 > \lambda_2$, EI_p is more difficult to get deviated from EI_{0p}. That is to say, the regularization parameter λ determines whether damage occurs: as long as $\lambda < |\Lambda_p|$, the pth element would admit stiffness change or damage; otherwise if $\lambda \geq |\Lambda_p|$, the damage would be found to not occur in the pth element.

3.2.2 Regularization parameter estimation

As shown in many refernces [52, 53], the regularization parameter λ plays an important role in the quality of the damage identification results, especially in cases where high levels of noise are present in the data. In this section, a novel and simple strategy, named 'threshold setting method', for estimating the optimal regularization parameter λ_{est}, is devised.

For each iterative step, $\mathbf{\Lambda} = \{|\Lambda_p|, p = 1, 2, ..., N\}$ could be obtained for each element by equation (3.21). From **Figure 3.2**, one could see a close relationship between λ and $\mathbf{\Lambda}$. In fact, λ is used to distinguish the damaged elements from the undamaged elements and $\mathbf{\Lambda}$ reflects the difference between the stiffness obtained directly from the CRE objective function without sparsity ($\hat{EI}_p$) and the undamaged stiffness (EI_{0p}) for each element. It is easily known that if this difference is large enough ($|\Lambda_p| > \lambda$), damage is reasonably assumed to occur. In other words, elements with higher values of $|\Lambda_p|$ are likely to be damaged with stronger possibility while lower values indicate undamaged and perturbation errors. Thus, setting one of the values in $\mathbf{\Lambda}$ as threshold could separate the damaged and undamaged elements.

As a result, a simple procedure to estimate the optimal regularization parameter $\lambda_{\text{est}} = \text{TSM}(\mathbf{\Lambda}, l_{\max}, \alpha)$ is proposed for each iterative step as follows:

1. Get $\mathbf{\Lambda}$ from equation (3.21) and sort the absolute values in descending order, leading to $\{\hat{\Lambda}_1 \geq \hat{\Lambda}_2 \geq ...\}$;

2. Fix the maximum threshold setting rank $l_{\max}$ and the discriminating ratio α;

3. Obtain the optimal regularization parameter λ_{est}: for each $l = 1, ..., l_{\max} - 1$,

$$\lambda_{\text{est}} = \begin{cases} \hat{\Lambda}_{l+1}, & \text{if } \hat{\Lambda}_l \geq \alpha \cdot \hat{\Lambda}_{l+1} \\ \hat{\Lambda}_{l_{\max}}, & \text{else} \end{cases} \tag{3.24}$$

The maximum threshold setting rank $l_{\max}$ limits the maximum number of possible damages and principally one tends to choose a relatively small value of $l_{\max}$ to guarantee the sparsity of the identification results. On the other hand, it is conceivable that the general undamaged elements have relatively small values of $|\Lambda_p|$ corresponding to the noise level and would be quite away from $|\Lambda_p|$ of the damaged elements. As a result, the discrimination ratio α measures the distance between the minimum error caused by possible damages and the maximum error purely invoked by the measurement noise level. If $\hat{\Lambda}_l$ is much greater than $\hat{\Lambda}_{l+1}$ ($\hat{\Lambda}_l \geq \alpha \cdot \hat{\Lambda}_{l+1}$), element l is identified as damaged. The maximum threshold setting rank $l_{\max}$ gives possible maximum number (initial guess) of damages while the discrimination ratio α narrow it down. The choice

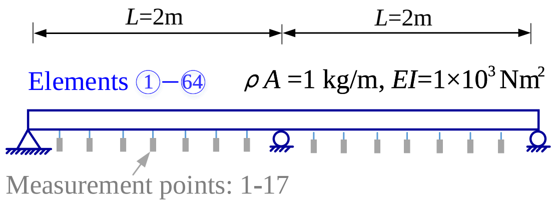

Figure 3.3 Model and measurement points of two-span continuous beam

of α should be very careful in the multiple damage case because it directly affects the identified number of damages. Nevertheless, the identification process tends to be reasonably robust with a broad selection of α, which is illustrated in detail in the following numerical example.

A numerical equi-spaced two-span continuous beam was studied to test the proposed threshold setting method. The first three modal responses of this beam were generated using finite element software. For detailed information on the geometry and boundary of the structure as well as the specific enumeration of the 17 equidistant measurement points, refer to **Figure 3.3**. 64 Euler-Bernoulli beam elements were used both for the modal evaluation model and the identification model. Damages were enforced by reducing the stiffness of the corresponding elements. Two damage cases are taken into account, including:

- Single damage case D1: stiffness EI reduced to 50% in element 21; and
- Multiple damage case D2: stiffness EI reduced to 90%, 80% and 85% in elements 16, 22 and 46 respectively.

Figure 3.4 shows the identification results in cases D1 and D2, using the proposed sparse-regularized min-CRE approach with threshold setting method to select the optimal regularization parameter λ_{est}. Noise is not considered herein. Good identification performance for this two-span continuous beam structure is achieved. The optimal regularization parameter λ_{est} from the threshold setting method in Section3.2.4 is 6.57×10^{-06} for D1 and 1.84×10^{-04} for D2 for the convergence step.

Next, to have an impression on how the regularization parameter λ affects the identification results in the min-CRE approach and testify the efficiency of the threshold setting method, changes in EI with different regularization parameters λ are additionally plotted in **Figure 3.5** for both single damage case D1 and multiple damage case

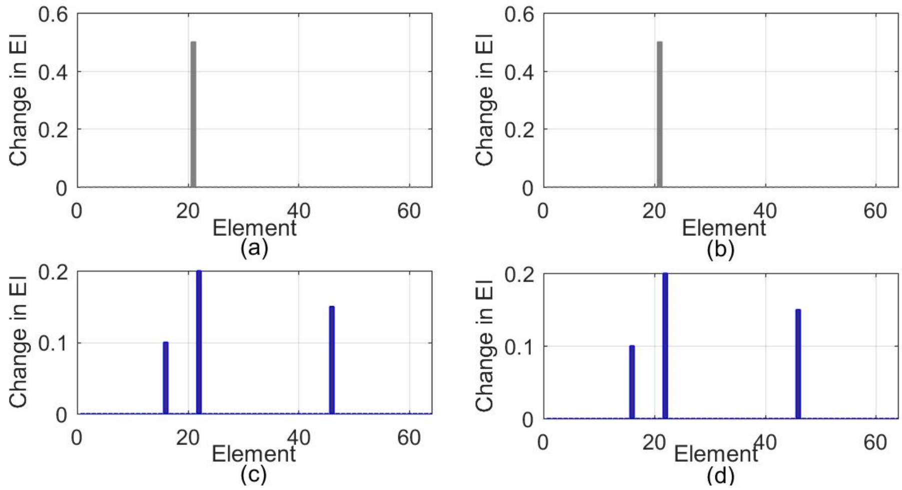

Figure 3.4 (a) actual damage for D1; (b) damage identification result for D1 using min-CRE approach with threshold setting method; (c) actual damage for D2; (d) damage identification result for D2 using min-CRE approach with threshold setting method

D2. As is observed, smaller value of λ or say, weaker enforcement of sparsity renders the identified results more sensitive to the error and uncertainty in modeling and simulation while very large value of λ or stronger enforcement of sparsity may fail in identifying damages or produce biased damage extents. **Figure 3.5** shows that $\lambda \in [10^{-6}, 10^{-3}]$ in D1 and $\lambda \in [10^{-4}, 10^{-3}]$ in D2 could result in satisfactory identified results, coinciding well with the good identification results from the threshold setting method as in **Figure 3.4** and again verifying the effectiveness of the threshold setting method. In addition, **Figure 3.5** exhibits a broader selection of λ in the single damage case D1 than in the multiple damage case D2. The choice of the regularization parameter λ must be paid more attention for multiple damage cases consequently.

To testify the robustness of the threshold setting method, a normal distribution noise is added to the simulated modal response as

$$\text{noise}(x) = randn \cdot a \cdot \phi(x) \tag{3.25}$$

where $randn$ is the normal distribution with zero mean and unit deviation, a is the applied noise level and $\phi(x)$ is the measured modal displacements at a certain point x. Noises of level 3% (Signal-to-Noise-Ratio, SNR=15dB) as well as 5% (SNR=13dB) for both of the cases D1 and D2 are considered in this example. As the natural frequencies

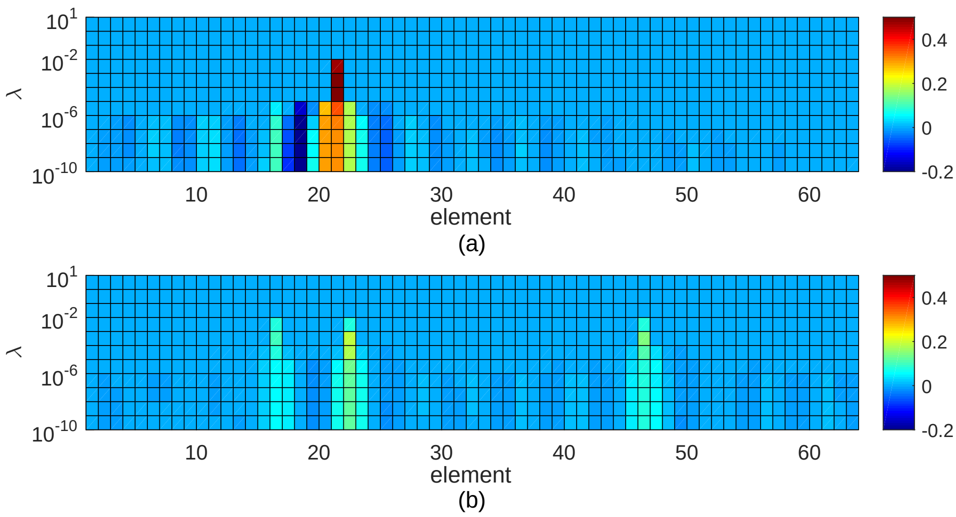

Figure 3.5 Reduction in EI with different vaules of regularization parameter λ: (a)D1 (b)D2

can be often measured with negligible error compared with the mode shapes, noise for natural frequencies is not considered herein.

As shown in **Figure 3.6**, damages are identified successfully when the measurement noise is not greater than 5% in single damage case D1 with a value of $\lambda_{\text{est}} = 0.1644$. In contrast, multiple damage case D2 seems to be more sensitive to the noise: under 3% noise level, actual damages in elements 16, 22 and 46 were properly identified but unwanted yet acceptable stiffness change at element 55 was also observed (**Figure 3.6**(c)); while under 5% noise level, the actual damage in element 46 was missed but false positions near element 60 were observed (**Figure 3.6**(d)). This phenomenon is attributable to the different effectiveness of the sparse regularization. Single damage is apparently more in conformity with the sparsity assumption while multiple damages reduce sparsity in intensity and rely more on the data fidelity. Consequently, damages occurring at less locations achieve better identification results by the sparse-regularized min-CRE approach.

Figure 3.7 compares the evolution of CRE for each of the iterative step with different levels of noise. The error decreases with the number of iterations increases and most of the damages are identified after 30 steps, verifying the convergence of the present method. Moreover, escapes from local minima could also be observed from this

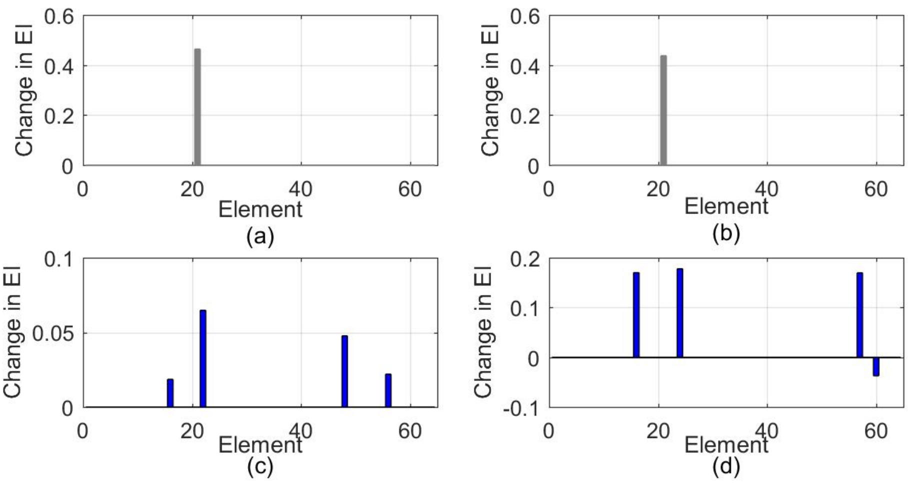

Figure 3.6 (a) damage identification result for D1 with 3% noise; (b) damage identification result for D1 with 5% noise; (c) damage identification result for D2 with 3% noise; (d) damage identification result for D2 with 5% noise

figure.

To get a better picture on how the discriminating ratio α in the threshold setting method works when determining λ_{est}, further simulations are performed. Noise of level 3% for both of the cases D1 and D2 are considered herein. **Figure 3.8** shows the obtained optimal regularization parameter λ_{est} (in purple) with various values of the parameter α. As is expected, the choice of higher value of α may result in improper damage identification in the single damage case D1 while lower value of α leads to incomplete damage identification in the multiple damage case D2. The main reason for this observation lies in **Eq.** (3.24): larger value of α makes the condition $\hat{\Lambda}_l \geq \alpha \cdot \hat{\Lambda}_{l+1}$ more difficult to be satisfied, implying that greater l is gained and less spare identification results are achieved. The appropriate ranges are $\alpha \in [1, 18]$ in D1 and $\alpha \in [3, 20]$ in D2. As is seen, the identification process is fairly robust for the choice of $\alpha \in [3, 18]$ and therefore, $\alpha = 4$ and $l_{\max} = 5$ are used for the following examples in this paper.

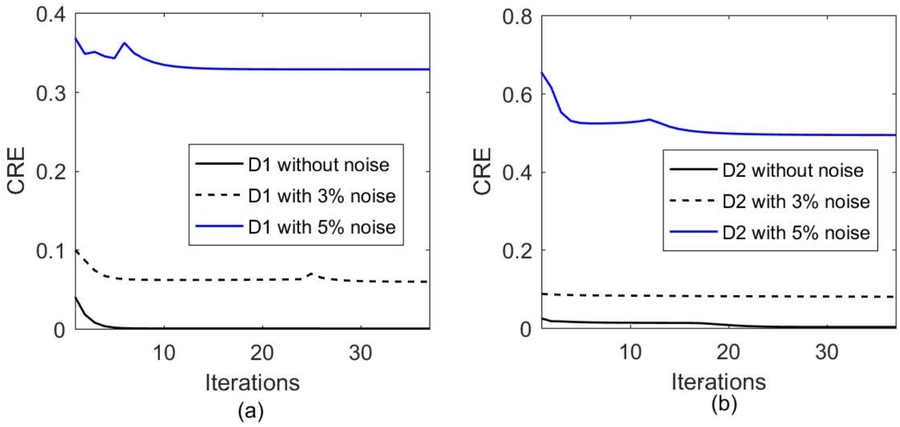

Figure 3.7 CRE vs iterations: (a)D1;(b)D2

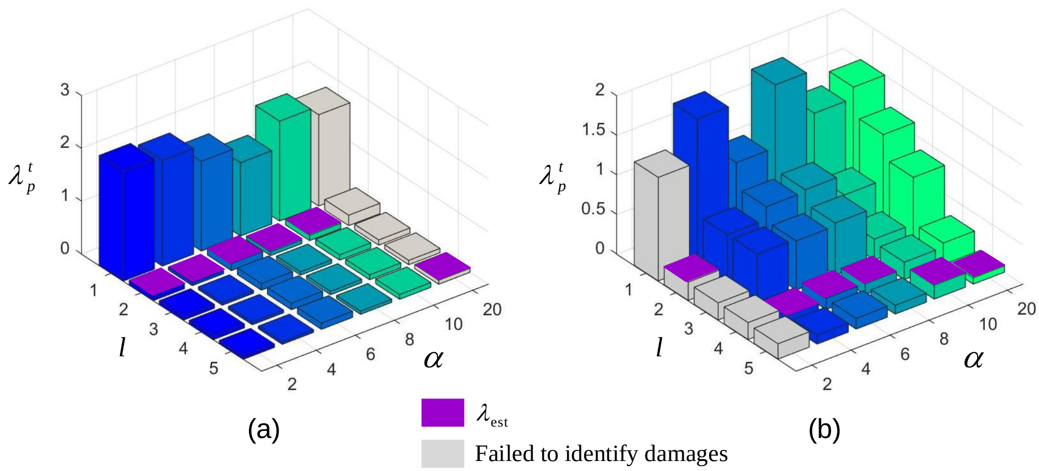

Figure 3.8 Adaptive choice of α (a)D1;(b)D2

Table 3.1 Measured frequencies and modal displacements of cracked simply supported beam

Case-order	Frequency(Hz)	x/L=0.1	0.2	0.3	0.4	0.5	0.6	0.7	0.8	0.9
CL1-1	11.162	0.632	1.182	1.585	1.843	1.927	1.836	1.576	1.169	0.614
CL1-2	43.857	1.168	1.839	1.766	1.035	0.055	-1.118	-1.808	-1.847	-1.154
CL2-1	11.019	0.635	1.208	1.598	1.842	1.912	1.820	1.557	1.159	0.612
CL2-2	42.701	1.170	1.839	1.766	0.959	-0.122	-1.146	-1.805	-1.821	-1.139
CL3-1	10.746	0.664	1.254	1.640	1.85	1.901	1.791	1.531	1.134	0.604
CL3-2	40.825	1.170	1.909	1.737	0.879	-0.209	-1.220	-1.813	-1.777	-1.094

3.3 Numerical verification

In the following, several numerical simulations are used to test the proposed sparse-regularized min-CRE approach. The performance of the threshold setting method to give the regularization parameter and the effectiveness and superior identifiability for structures with different damage severities by the sparse-regularized min-CRE approach are demonstrated in Section 3.3.1 and Section 3.3.2 shows that the sparse regularization can significantly improve the robustness of the identification results from Monte Carlo simulations.

3.3.1 Single cracked simply supported beams

Simply supported post-tensioned beams with different damage extents are to be identified in this example (see the reference [54] for details of the structure). Parameters of the simply supported beam are: length L = 3.6m, rectangular cross-section $t \times H = 0.1\text{m} \times 0.125\text{m}$, stiffness of the beam before damaged $k^0 = EI = 2.44 \times 10^5 \text{Nm}^2$ and mass per unit length $\rho A = 29.44$ kg/m. As shown in **Figure 3.9**, damage was simulated by a designed crack-depth ($a/H = 0.09, 0.27, 0.45$) for each damage case (CL1,CL2,CL3) and located at 0.89m(x/L=0.248) from the left edge. The first two modal responses of these structures were obtained by the 3D FE models from the reference [55]. The 3D FE model, with totally 28,512 block elements (288 elements along the length of the beam) used for the modal analysis, was generated using the commercial software ANSYS and damage was inflicted by reducing the stiffness of the appropriate elements. The vibration amplitude was measured at nine equally spaced positions, each of which was 36cm between two adjacent locations.

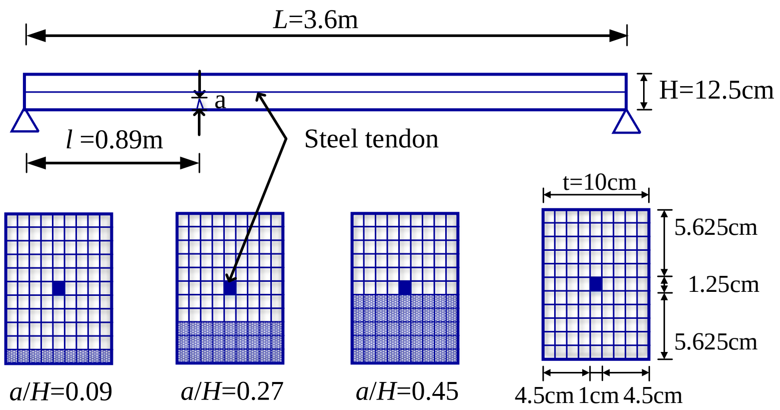

Figure 3.9 3D finite element model with different damage severities for modal responses

In reference [55], a mode-shape-based damage detection method based on the sensitivity approach, using the Euler-Bernoulli beam model with 288 elements of equal size, was used to identify the damage, while the model for damage detection in the min-CRE approach consists of 50 beam elements.

Damage identification results for each damage case obtained by the min-CRE approach as well as the sensitivity approach in reference [55] are summarized in **Table 3.2**. It is shown that the min-CRE approach could give nearly the same results for damage localization as well as damage extent assessment in CL2 (middle damage case) and even superior results in CL3 (large damage case) when compared with the results in reference [55]. The accuracy of the damage localization by the present approach was evaluated by measuring the localization error, ranged from 5% to 19% and the accuracy of damage severity is from 21% to 33%. For CL1 (small damage case), the identified results obtained by the present min-CRE approach are reasonable and slightly less satisfactory than the results by the sensitivity approach. This is mostly caused by the fact that under small damage, the difference/error between the displacement-based FE model and the force-based FE model may be in the same level with the discrepancy of the derived modal data between the damaged and undamaged structures.

To visualize the convergence of the min-CRE approach for the large damage case, detailed results on the damage index of the most probable damaged element 11 and its nearest elements 8-10 at each iteration step, are given in **Figure 3.10**. Obviously, all the quantities converge within 27 iterations verifying the convergence of the proposed two-step substitution algorithm even for the large damage case.

Table 3.2 Damage identification of simply supported beam compared to the results in reference

Damage case -method	Damage Index (FE model)	Predicted Damage Range Elements(x/L)	Most Probable Element(Location)	Damage Index (Identified)	λ_{est}
CL1-CRE	0.76	6-10(0.1-0.2)	10(0.20)	0.973	0.230
CL1-reference[55]	0.76	55-81(0.191-0.280)	67(0.233)	0.926	\
CL2-CRE	0.41	11-15(0.2-0.3)	13(0.26)	0.62	0.300
CL2-reference[55]	0.41	55-80(0.191-0.277)	67(0.233)	0.636	\
CL3-CRE	0.22	11-15(0.2-0.3)	11(0.22)	0.29	0.466
CL3-reference[55]	0.22	55-81(0.191-0.277)	67(0.233)	0.491	\

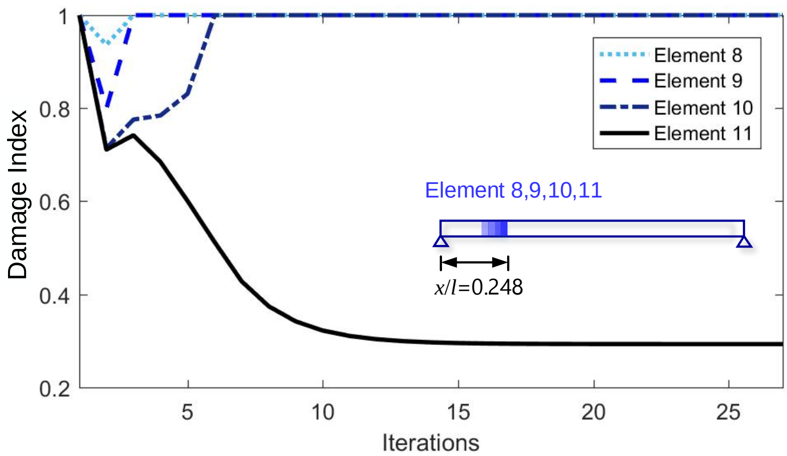

Figure 3.10 Convergence of Damage Index for simply supported beam in CL3

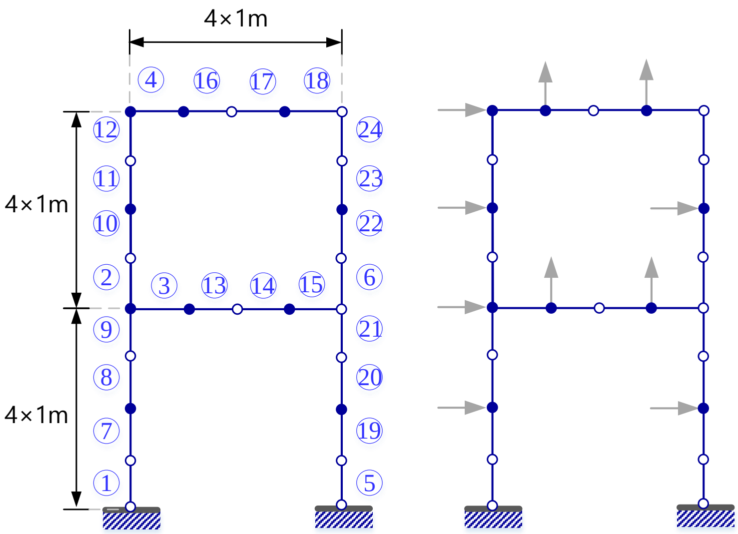

Figure 3.11 Model and measurement points of plane frame structure

3.3.2 Plane frame structure

A plane frame structure[56] as shown in **Figure 3.11** is to be studied to demonstrate the robustness of the proposed sparse regularization technique. The axial displacement u_x, tension force N and the corresponding longitudinal inertial force f_t are addtionally considered in this case. The damage paremeter is set to be $\mathcal{K} = E(x)$ instead of $EI(x)$. The height and width of the frame are $H = L \times 2 = 8$m and $L = 4$m, respectively, with the inertial moment for planar bending $I = 5 \times 10^{-9}\text{m}^4$ and cross-secional area $A = 1 \times 10^{-7}\text{m}^2$. For the undamaged frame, the mass density of the material is $\rho = 10^7\text{kg/m}^3$, the Poisson's ratio is $\nu = 0.3$ and the Young's modulus is $E = 2 \times 10^8\text{N/m}^2$. The plane frame consists of 24 Euler-Bernoulli beam elements with 24 nodes, each with three DOFs. The vibration amplitude measurement locations and corresponding direction are also illustrated in **Figure 3.11** and the measured modal displacements are normalized with respect to the maximum vibration amplitude. Herein, the Young's modulus of each element is identified and no damage pattern is needed to be assumed before the identifcation process, which is different from reference [56].

Two damage cases are considered: damages were enforced by reducing the Young's modulus E to 25% in element 1 and 75% in element 9 in case D1 and to 85% in element 1 and 85% in element 9 in case D2. According to reference [56], damage case D1 with

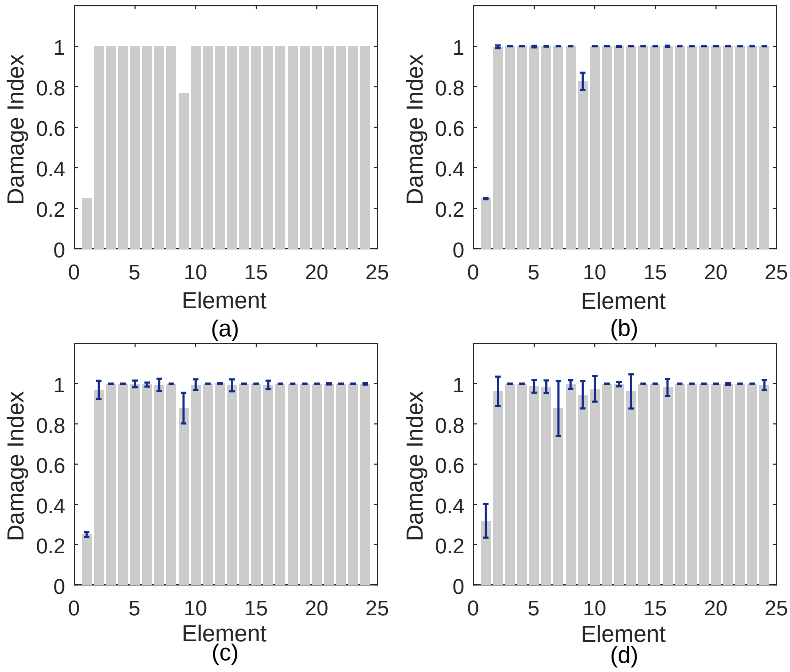

Figure 3.12 Mean values and standard deviations of Damage Index for: (a) no noise; (b) 2% noise; (c) 5% noise; (d) 10% noise in D1

large stiffness differences for close elements was selected based on the experience due to its hard identifiability. The first three modes and their frequencies are used herein and all modes are equally weighted. The normal distribution noise described in Equation (3.25) is used and noises of level 2%, 5% and 10% (SNR=17dB, 13dB and 10dB) are considered in this example. Again, noise for natural frequencies are not considered herein.

As shown in **Figure 3.12**(a) and **Figure 3.13**(a), good identification performance is achieved when there is no noise. The optimal regularization parameter λ_{est} is 3.4×10^{-4} and 1.1×10^{-4}. To get a better picture for the cases with noise, statistical analysis was performed. Mean values and standard deviations of damage index over 100 Monte Carlo trials with different levels of noise are presented in **Figure 3.12**(b)(c)(d) and **Figure 3.13**(b)(c)(d). The mean of the optimal regularization parameters is 1.7×10^{-3}, 2.3×10^{-3} and 6.0×10^{-3} for D1 and 1.3×10^{-3}, 2.7×10^{-3} and 5.5×10^{-3} for D2. Satisfactory identification results are observed even under the noise level 10%.

Figure 3.14 compares the results obtained by the min-CRE approach in D1 with

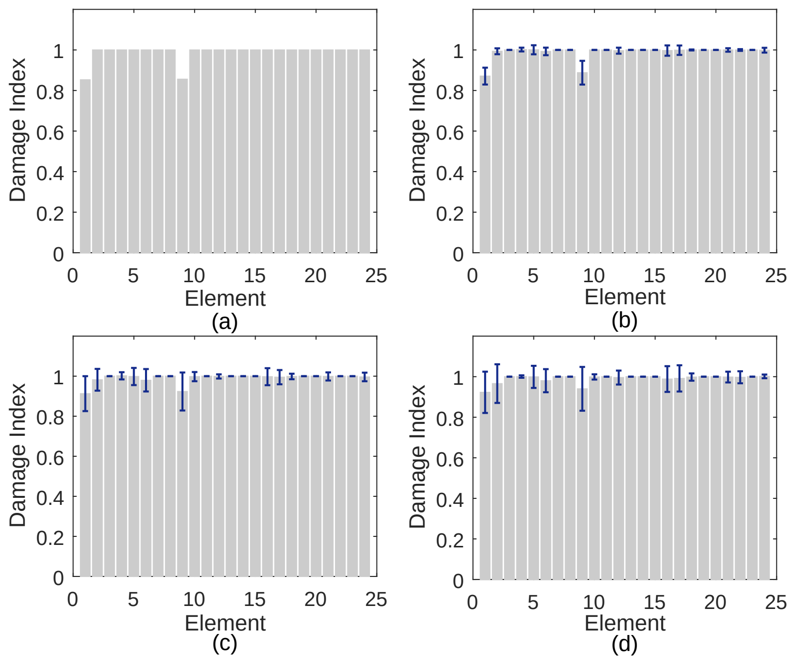

Figure 3.13 Mean values and standard deviations of Damage Index for: (a) no noise; (b) 2% noise; (c) 5% noise; (d) 10% noise in D2

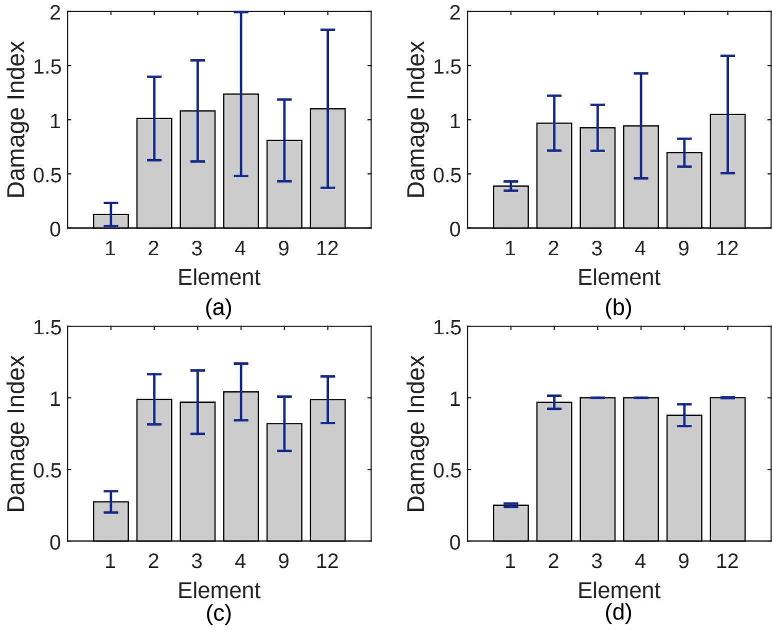

Figure 3.14 Identification results with 5% noise by: (a) reference without regularization; (b) min-CRE without regularization;(c) reference with regularization; (d) min-CRE with regularization

the identification results in reference [56], where a sensitivity-based approach with Tikhonov regularization was used. Obviously, the sparse-regularized min-CRE approach gives the best estimation of the damage parameters in terms of the mean values and standard deviations of the damage indices. The reason for different levels of standard deviation is possibly because some elements are more sensitive to perturbation errors than others. Moreover, it is clear that the sparse regularization greatly improves the identifiability and robustness of the min-CRE approach by comparing the results between **Figure 3.14**(b)(min-CRE approach without regularization) and (d)(min-CRE approach with regularization).

To visualize how the sparse-regularized min-CRE approach proceeds, the iterative procedure for the case of 5% noise is shown in **Figure 3.15**. Although it seems to take a little more steps to get the convergence, this approach would still be an efficient tool for structural damage identification.

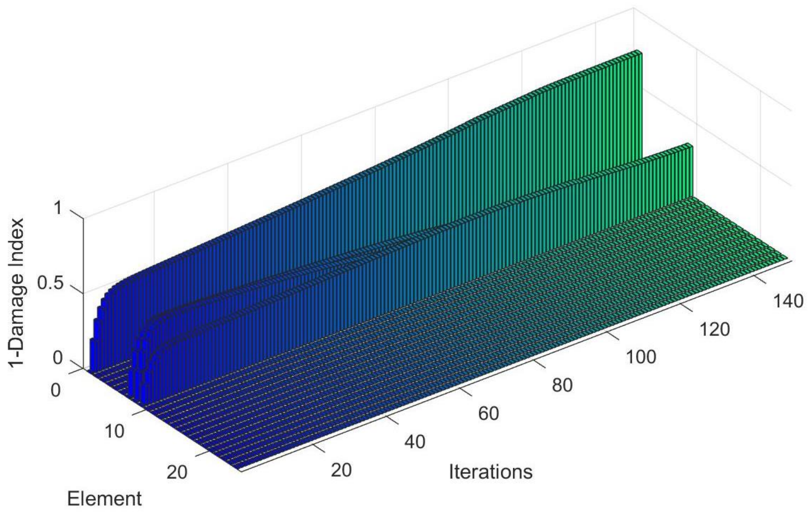

Figure 3.15 Damage identification procedure of plane frame structure

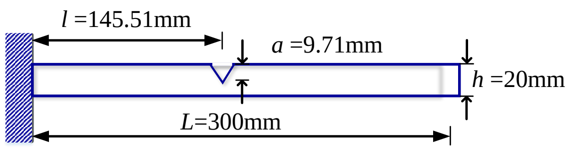

Figure 3.16 The cracked cantilever beam specimen

3.4 Experimental verification

3.4.1 Crack identification in a cantilever beam

A single cracked cantilever beam as shown in **Figure 3.16** is adopted as the first experimental verification example. The crack is assumed to remain a continuum and the mechanical properties (stiffness EI in beam model or Young's modulus E in plane stress model) are modified to account for the effect of cracking, that is, the following models do not account for discontinuities in the topology of the FE mesh for this kind of general damage identification problem.

The length of the beam is $L = 300$mm with square cross-section $h \times d = 20\text{mm} \times 20\text{mm}$. The stiffness of beam is $k_0 = EI = 2.75 \times 10^3\text{Nm}^2$ and the mass per unit length is taken to be $\rho A = 3.12$ kg/m. The crack is located at $l = 145.51$mm from the clamped end with depth $a = 9.71$mm. The crack was initiated with a thin saw-cut and

Table 3.3 Measured frequencies and modal displacements of cracked cantilever beam

Order	Frequency(Hz)	x/L=0.1	0.2	0.3	0.4	0.5	0.6	0.7	0.9	1.0
1	171	0.027	0.063	0.109	0.156	0.236	0.354	0.487	0.778	0.940
2	987	0.069	0.149	0.276	0.444	0.516	0.400	0.200	-0.455	-0.899
3	3034	0.033	0.103	0.221	0.288	0.011	-0.387	-0.498	-0.203	0.435

propagated to the desired depth by fatigue loading. The crack depth was measured directly and verified with an ultrasonic detector for uniformity and actual depth. The measured natural frequencies and modal responses were obtained experimentally [57]. Electromagnetic vibrator, amplifier and accelerometer were utilized in the experiment. Harmonic excitation was applied and only one mode at a time was investigated. The signal generator could be tuned to the natural frequency of interest automatically by using a frequency hunting circuit.

The vibration amplitude was measured at the positions 30mm, 60mm, 90mm, 120mm, 150mm, 180mm, 210mm, 270mm and 300mm. The amplitude of motion at 240mm was not measured. The vibration signal was transferred to a vibration analyzer and a recorder to give plots of vibration amplitude versus frequency. The first three mode shapes were measured by using two calibrated accelerometers mounted on the beam. One accelerometer was kept at the clamped end of the beam to measure the mode amplitude. The data used in this case is summarized in **Table 3.3**. It should be noted that the modal displacements herein contain not only the measurement errors but also digitized process errors when extracted from the published paper [57] (see also the reference [58]).

By performing the two-step substitution algorithm in Section 3.2, the min-CRE approach for damage identification can be used. The optimal regularization parameter obtained by the threshold setting method is $\lambda_{\text{est}} = 197.97$. Well identification performance for the structure is achieved by the proposed sparse-regularized approach with comparision to the identification results in the reference [58] and detailed results are shown in **Figure 3.17**. In the reference [58], the same frequencies and modal displacements data in **Table 3.3** were used and an algorithm was proposed considering changes in estimated constitutive properties of the finite element model with an output-error parameter estimation algorithm to localize the damage. Two models were used for damage detection in the reference [58]

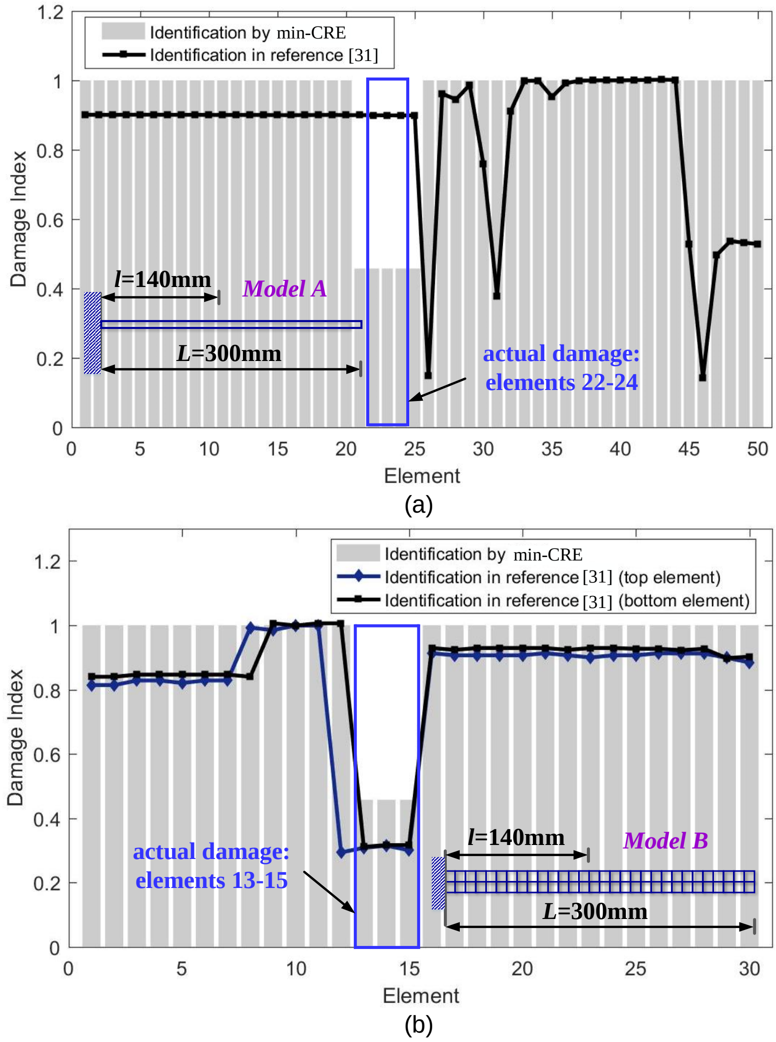

Figure 3.17 Identification results using sparse-regularized min-CRE approach compared to the results in reference (model A and model B)

- model A: structure modeled by 50 Euler-Bernoulli beam elements;
- model B: structure modeled by 60 two-dimensional plane stress square four-node elements without geometric defects (30 elements on the top row and 30 elements on the bottom row).

Accordingly, structure with 50 Euler-Bernoulli beam elements, compared with Model A in the reference and structure with 30 Bernoulli-Euler beam elements, compared with Model B are established for damage identification in the sparse-regularized min-CRE approach.

For the beam model case, although the crack was identified by model A in the reference [58], elements at other locations such as element 31 and 46 were also detected as damaged. The crack actually lied between element 22 and 24 and the results from the min-CRE approach clearly identify a range of elements 21-25. Model B in reference [58] offered a much better result than model A: elements 12-15 on the top row and 13-15 on the bottom row were detected as damages, while the beam model of the min-CRE approach again exhibits a very good identification performance: the crack lies between element 13 and 15, which are the exact damage locations. Obviously, the distributive stiffness is well identified with limited and incomplete experimental modal data by the sparse-regularized min-CRE approach.

3.4.2 Crack identification in a beam with two fixed ends

The proposed damage identification algorithm was also applied to an aluminum beam with two fixed ends [59] as shown in **Figure 3.18**. The parameters are set as follows: $E = 70\text{GPa}$, $\nu = 0.3$ and $\rho = 2.7\times10^3\text{kg/m}^3$. A saw-cut damage was applied by cutting two cracks on the top and bottom surface of the intact beam with a depth of quarter of the total thickness of the beam for each crack. Experimental modal data were obtained by the impact excitation and only one accelerometer was employed at the center of the beam to measure the deflection response. Modal responses were attained through one line in the transfer function matrix. More details of this experiment could be found in reference [59]. The first three-order frequencies and mode shapes of the damaged beam are used herein (**Figure 3.18**). Based on the FEM computation from reference [59], the saw-cut damage could be simulated using 87.5% reduction of the bending stiffness in the ninth element.

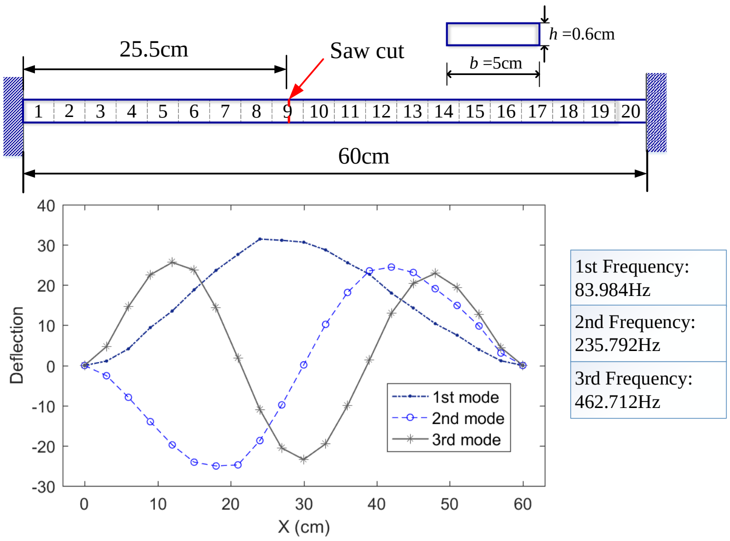

Figure 3.18 A beam with two fixed ends and its first three order measured modes (damaged)

Two identification methods which are similar in concept to the best achievable eigenvector tehcnique were proposed in reference [59]. The first one (DDNKM) does not employ the analytical global stiffness and mass matrices completely; the second one (DDNK) uses the analytical global mass matrix only. These approaches first locate the damages using a special subspace rotation algorithm, and then identify the magnitude of damage using the quadratic programming technique.

By employing the first two orders of measured modal data, the identification results using DDNKM, DDNK and min-CRE approach are shown in **Figure 3.19**(a), (b) and (c) respectively. It can be found that the damaged element 9 can be detected very clearly from the min-CRE approach. The damage extent of the min-CRE approach is reasonable, although not as accurate as DDNK. The reason that the proposed algorithm exhibits such strong capability in damage location is that the sparsity could extract the most important features from the measured information (the damage) while suppress the less important ones which seems to be introduced by the noise. The optimal regularization parameter obtained by the threshold setting method is $\lambda_{\text{est}} = 738.76$, suggesting an strong enforcement of sparsity and hence the identified damage extent is slightly biased. The same phenomenon could be seen from the case employing the first three orders of measured modal data (**Figure 3.20**). In this case, the sparse-

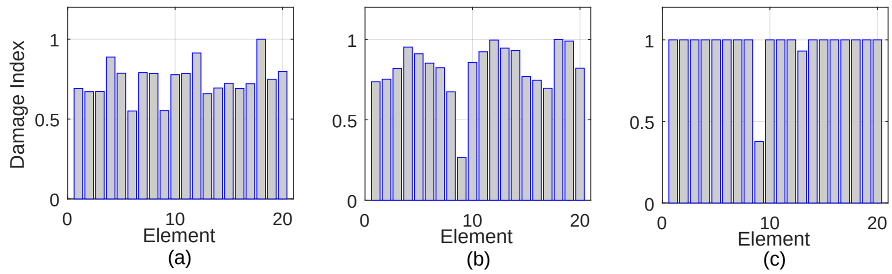

Figure 3.19 Identification results by employing the first two orders of measured modal data: (a)DDNKM (b)DDNK (c)sparse-regularized min-CRE

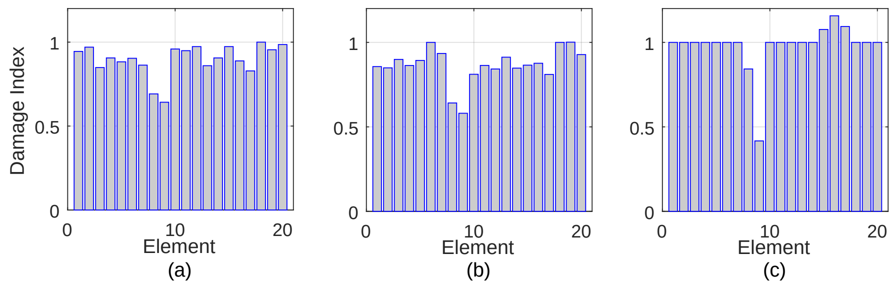

Figure 3.20 Identification results by employing the first three orders of measured modal data: (a)DDNKM (b)DDNK (c)sparse-regularized min-CRE

regularized min-CRE approach offers a much better identification results than the other two methods in reference [59], no matter in regard to the assessment of the damage localization or the damage extent. However, compared with the results from the min-CRE approach based on the first two orders of measured modal data, no obvious improvement seems to be attained for this case. The reason is that the first two modes are already enough to detect the damage and higher level measured error may be invoked in the third mode. A relatively small weight coefficient is suggested to be chosen for the third mode in this situation as mentioned in Section 3.1.3.

For further comparison, the recently developed damage identification approach via sparse representation (SR) classification in reference [60] is also called to identify the damage in the beam. Note from the above analysis that using the first two modes have led to better identification results than using the first three modes and therefore, only the first two modes are adopted for damage identification by the SR approach herein. In doing so, two stages are involved:

Table 3.4 Predefined damage classes of the beam for Stage 1

Class	1	2	3	$\cdots$	19	20
Damage location	Element 1	Element 2	Element 3	$\cdots$	Element 19	Element 20
Damage extent	50%	50%	50%	$\cdots$	50%	50%
Obtained incomplete mode shapes	$\Phi_1 \in \mathrm{R}^{19\times 2}$	$\Phi_2 \in \mathrm{R}^{19\times 2}$	$\Phi_3 \in \mathrm{R}^{19\times 2}$	$\cdots$	$\Phi_{19} \in \mathrm{R}^{19\times 2}$	$\Phi_{20} \in \mathrm{R}^{19\times 2}$
Reference matrix	$\Psi_1 = [\Phi_1, \Phi_2, \cdots, \Phi_{19}, \Phi_{20}] \in \mathrm{R}^{19\times 40}$					

- Stage 1. Identification of damage location

  1. Predefine damage classes of the beam (see **Figure 3.18**) with all possible damage locations and then, details are presented **Table 3.4**. For each damage class, get the first two incomplete mode shapes that correspond to the measured first two mode shapes. Then, collect the first two incomplete mode shapes of all damage classes to form the reference matrix.
  2. For each of the two measured mode shapes, use ℓ_1 minimization to obtain the sparse solution. Then, the recovery error $\varepsilon = \sum_{i\in S} \sum_{k\in\wp} (u_{ki} - \hat{u}_{ki})^2$ of each damage class in reference [60] has been calculated. Detailed results on the recovery error are displayed in **Figure 3.21**(a). Clearly, damage location at element 9 is well identified because the damage class with the smallest recovery error is in principle the desired one for the beam.

- Stage 2. Identification of damage extent

  1. Predefine damage classes of the beam with predefined damage location at element 9 and all possible damage extents for which the details are listed in **Table 3.5**.
  2. Repeat Stage 1 except that the predefined damage classes only consider the reference structural FEM model damaged at the identified location with all possible damage extents. Results on the recovery error under different damage extents are obtainable as depicted in **Figure 3.21**(b). Obviously, the damage extent of 70% is identified.

To conclude, damage location at element 9 of extent 70% has been well identified in the beam by the two-step SR approach in reference [60]. Comparing the identification results in Figure 19(c) by the proposed sparse-regularized min-CRE approach with the identification results by the two-step SR approach, both approaches have given rise

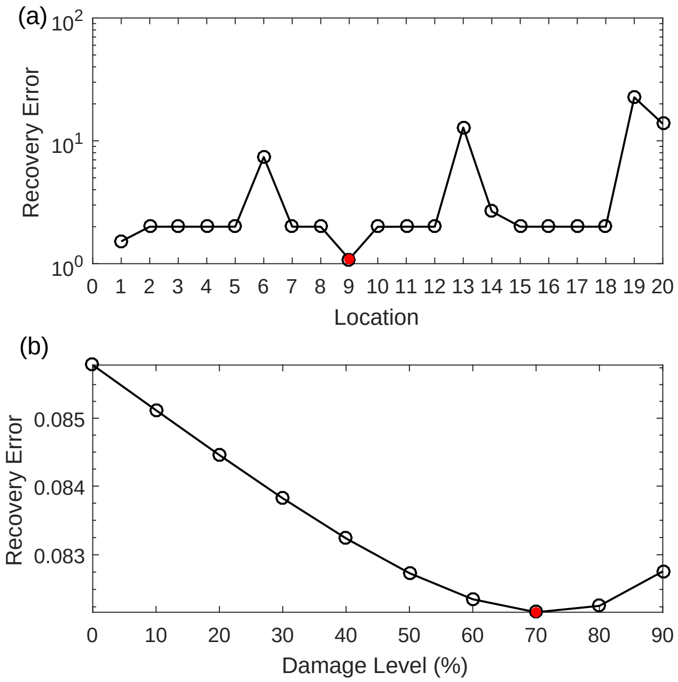

Figure 3.21 Identification results by SR of (a) damage location and (b) damage extent

Table 3.5 Predefined damage classes of the beam for Stage 2

Class	1	2	3	$\cdots$	9	10
Damage location	Element 9	Element 9	Element 9	$\cdots$	Element 9	Element 9
Damage extent	0%	10%	20%	$\cdots$	80%	90%
Obtained incomplete mode shapes	$\Phi_1 \in \mathrm{R}^{19\times 2}$	$\Phi_2 \in \mathrm{R}^{19\times 2}$	$\Phi_3 \in \mathrm{R}^{19\times 2}$	$\cdots$	$\Phi_9 \in \mathrm{R}^{19\times 2}$	$\Phi_{10} \in \mathrm{R}^{19\times 2}$
Reference matrix	$\Psi_2 = [\Phi_1, \Phi_2, \cdots, \Phi_9, \Phi_{10}] \in \mathrm{R}^{19\times 20}$					

to satisfactory identification of the damage: damage location at element 9 is perfectly detected with almost no fictious damage locations while damage extent around 0.7 is also reasonably identified. The good performance of both approaches shall be benefit from the sparsity assumption—sparsity of damage locations for the proposed sparse-regularized min-CRE approach and sparsity of damage classes for the two-step SR approach. Correspondingly, the importance of the sparsity in damage identification is recognized. It should be noted that the SR approach is efficient and robust for both single and multiple damage cases, but it is found that this approach is incapable of identifying small damage with very limited sensors [60]. However, as shown in the numerical example, the proposed sparse-regularized min-CRE approach can well identify small damages if the damage locations are scarce enough. In other words, in case when small damages occur at a single or scarce location, the proposed approach is recommended.

3.5 Conclusions

A modal-based damage identification approach by the minimum constitutive relation error (min-CRE) principle and the sparse regularization was proposed in this paper. To this end, a (separately) convex objective function, also known as the CRE, to measure the residual of the constitutive equations connecting between the admissible stress field and the admissible displacement field has been established and the sparse regularization has been enforced to enhance the robustness of the damage identification with insufficient modal data. The alternating minimization (AM) method was then applied to practically get the solution and a simple strategy for automatically selecting the regularization parameter was presented. Results show that:

1. The objective CRE function is separately convex, and therefore, large damages become identifiable.

2. The sparse regularization is enforced such that incomplete as well as noisy modal data can also lead to good identification and it indeed enhances the robustness of the damage identification procedure.

3. The present threshold setting method to get the regularization parameter is effective. The identification process is fair robust for the choice of the parameters α and $l_{\max}$ in the threshold setting method.

4. The present sparse-regularized min-CRE approach can give good identification results of the damage locations and severities for damage with relatively few damage locations, while for damage with multiple damage locations, identification of the damage location is still satisfactory.

5. The present damage identification approach performs well in both numerical and experimental tests.

6. Though the sparse regularization has already been incorporated into the sensitivity-based approaches, the incorporation is not straightforward at all, because minimization of the linearized objective function along with the sparse regularization term at every sensitivity-based iteration should again resort to an iterative procedure. In contrast, minimization of the CRE objective function along with the sparse regularization over the damage parameters can be directly solved at once with closed-form solutions.

7. No sensitivity analysis needs to be called in the present sparse-regularized min-CRE approach, and the exact order, for example, first/second of the mode shape, which must be known in the sensitivity-based approaches, is not required in the min-CRE approach.

8. Comparing the identification by the proposed min-CRE approach with the identification results by the two-step SR approach, both approaches have given rise to satisfactory identification of the damage, which benefits from the sparsity assumption.

Thus, it is believed that the proposed approach can serve as an effective tool for practical structural damage identification using incomplete modal data.

4

Damage identification using frequency domain data

The previous chapter is based on use of modal parameters. As modal parameters are indirectly-measured test data, they could be contaminated by measurement errors as well as modal extraction errors. In addition, modal test often requires a large number of sensors so as to obtain enough modal data. To avoid disadvantages of using modal data, the frequency response function (FRF) data, directly extracted from the dynamic test, are used as the measured data in this chapter. The FRF expresses the frequency domain relationship between an input signal and output signal of a linear, time-invariant system. The input excitation can be of a selected frequency band, stepped sinusoid, transient or periodic. It is usually measured by a force transducer at the driving point while the output is measured by accelerometers or other sensors. Vibration-based damage identification using FRF measurements has been studied by a number of references [61] and it has been proved that FRF data are more reliable and practical to provide abundant information at limited measured degrees of freedom and at a great number of desired frequencies [62]. In a broad sense, those methods using modal data are discrete versions of the methods using FRF data [63].

In order to have consistent notations with other chapters, symbols in this chapter are defined as follows. Given input and output time histories, the FRF can be calculated through the output/input Fourier Transform ratio:

$$\text{Receptance FRF} = \frac{\boldsymbol{U}(\omega)}{\boldsymbol{F}(\omega)} = \frac{\boldsymbol{A}(\omega)}{-\omega^2 \boldsymbol{F}(\omega)}$$

where $\boldsymbol{F}(\omega)$ is the Fourier Transform of the input excitation and $\boldsymbol{U}(\omega)$, $\boldsymbol{A}(\omega)$ is the Fourier Transform of the measured displacements and accelerations, respectively. The FRF could also be estimated by cross power spectral density and power spectral density of the input and output signal [64].

As FRF could be viewed as the response of the system for unit sinusoidal input $\boldsymbol{e}$, the displacement field $\boldsymbol{u}$ and traction field $\boldsymbol{t}$ in the following sections are expressed as

$$\boldsymbol{u} = \text{Receptance FRF}, \;\; \boldsymbol{t} = \boldsymbol{e}.$$

4.1 Problem statement

4.1.1 Baseline model

Consider an elastic structure occupying the open domain Ω and bounded by the boundary $\partial\Omega$. The vibration of this linear elastic problem in frequency domain is divided into three sets of differential equations for the displacement field $\boldsymbol{u}$ and the stress field $\boldsymbol{\sigma}$.

- **Kinematic constraints**

$$\boldsymbol{u} \in \mathfrak{U} := \begin{cases} \boldsymbol{\varepsilon} = \boldsymbol{B}\boldsymbol{u} \text{ in } \Omega \\ \boldsymbol{u} = \boldsymbol{u}_p \text{ over } \partial\Omega_u \end{cases} \tag{4.1}$$

  where $\boldsymbol{B}$ is a suitable linear differential operator and $\boldsymbol{u}_p$ is the prescribed value of the displacement filed $\boldsymbol{u}$ on the Dirichlet boundary $\partial\Omega_u$. $\boldsymbol{\varepsilon}$ represents the deformation tensor.

- **Equilibrium equations**

$$\boldsymbol{\sigma} \in \mathfrak{S} := \begin{cases} \boldsymbol{\mathcal{L}}\boldsymbol{\sigma} + \boldsymbol{b} = \boldsymbol{\tau} \text{ in } \Omega \\ \boldsymbol{n}\boldsymbol{\sigma} = \boldsymbol{t} \text{ over } \partial\Omega_f \end{cases} \tag{4.2}$$

  where $\boldsymbol{\mathcal{L}}$ is the divergence operator on stress filed $\boldsymbol{\sigma}$ and $\boldsymbol{n}$ the external unit vector normal to the Neumann boundary $\partial\Omega_f$. Over $\partial\Omega_f$, the traction field $\boldsymbol{t}$ is prescribed. In addition, $\boldsymbol{b}$ denotes the body force and $\boldsymbol{b} = \boldsymbol{0}$ herein. $\boldsymbol{\tau}$ is the inertial force.

- **Constitutive relations**

$$\begin{cases} \boldsymbol{\sigma} = \boldsymbol{D}\boldsymbol{\varepsilon} \text{—Hooke's law,} \\ \boldsymbol{\tau} = -\omega^2 \rho \boldsymbol{u} \text{—Newton's law.} \end{cases} \tag{4.3}$$

where $\boldsymbol{D} \in \mathcal{C}$ is an elastic matrix with appropriate material properties and ρ is the density which is assumed to be constant in this research. It should be noted that only the case of forced vibrations problems are considered and the equations are written in the frequency domain with ω being the angular frequency herein.

4.1.2 CRE function

To define the constitutive relation error (CRE), consider an admissible physical pair $(\boldsymbol{u}, \boldsymbol{\sigma})$, of which the displacements $\boldsymbol{u}$ satisfy the kinematic constrains (4.1) ($\boldsymbol{u} \in \mathcal{U}$) and the stresses $\boldsymbol{\sigma}$ satisfy the equilibrium equations (4.2) ($\boldsymbol{\sigma} \in \Im$), respectively. It is easily known that, if the constitutive relations (4.3) are additionally satisfied with an elastic modulus matrix $\boldsymbol{D}(\boldsymbol{\theta})$ ($\boldsymbol{\theta} \in \mathcal{A} \subseteq \mathbb{R}^{m+}$), where $\mathcal{A}$ denotes the admissible damage parametric space with $\theta_e = 1$ meaning no damage of the eth element, the above admissible solution trio $(\boldsymbol{u}, \boldsymbol{\sigma}, \boldsymbol{\theta})$ would be the exact solution $(\boldsymbol{u}_{\text{ex}}, \boldsymbol{\sigma}_{\text{ex}}, \boldsymbol{\theta}_{\text{ex}})$.

As a result, to measure the distance from the admissible solution to the exact solution in the energy product, the CRE for a given frequency is expressed as

$$\begin{aligned} e_{CRE}(\boldsymbol{u}, \boldsymbol{\sigma}, \boldsymbol{\theta}) = \frac{1}{2} \int_{\Omega} \Big\{ & r_1 \left[\boldsymbol{\sigma} - \boldsymbol{D}(\boldsymbol{\theta})\boldsymbol{\varepsilon}(\boldsymbol{u})\right]^{\mathrm{T}} \boldsymbol{D}(\boldsymbol{\theta})^{-1} \left[\boldsymbol{\sigma} - \boldsymbol{D}(\boldsymbol{\theta})\boldsymbol{\varepsilon}(\boldsymbol{u})\right] + \\ & r_2 (\rho\omega^2)^{-1} \left[\boldsymbol{\tau}(\boldsymbol{\sigma}) + \rho\omega^2 \boldsymbol{u}\right]^{\mathrm{T}} \left[\boldsymbol{\tau}(\boldsymbol{\sigma}) + \rho\omega^2 \boldsymbol{u}\right] \Big\} \, d\Omega \end{aligned} \tag{4.4}$$

where r_1, r_2 are the corresponding weight coefficients ($r_1 + r_2 = 1$). The values of these coefficients depend on the relative reliability between the constitutive relations based on the Hooke's law and based on the Newton's law and are fixed to be $r_1 = r_2 = 0.5$ in this work.

Further considering the kinematic constrains and the equilibrium equations, the CRE in equation (4.4) could be rewritten as

$$\begin{aligned} e_{CRE}(\boldsymbol{u}, \boldsymbol{\sigma}, \boldsymbol{\theta}) = \frac{1}{2} \int_{\Omega} \Big\{ & r_1 \left[\boldsymbol{\sigma} - \boldsymbol{D}(\boldsymbol{\theta})\boldsymbol{B}\boldsymbol{u}\right]^{\mathrm{T}} \boldsymbol{D}^{-1} \left[\boldsymbol{\sigma} - \boldsymbol{D}(\boldsymbol{\theta})(\boldsymbol{\theta})\boldsymbol{B}\boldsymbol{u}\right] + \\ & r_2 (\rho\omega^2)^{-1} \left[(\boldsymbol{\mathcal{L}}\boldsymbol{\sigma} + \boldsymbol{b} + \rho\omega^2 \boldsymbol{u})^{\mathrm{T}} (\boldsymbol{\mathcal{L}}\boldsymbol{\sigma} + \boldsymbol{b} + \rho\omega^2 \boldsymbol{u})\right] \Big\} \, d\Omega \end{aligned} \tag{4.5}$$

For the structure which is of interest in a frequency range $[\omega_{\min}, \omega_{\max}]$, the frequency weighting factor $z(\omega)$ is introduced

$$\int_{\omega_{\min}}^{\omega_{\max}} z(\omega) = 1, \;\; z(\omega) > 0 \tag{4.6}$$

Then the total CRE in the given frequency range is established as

$$\hat{F}(\boldsymbol{u}, \boldsymbol{\sigma}, \boldsymbol{\theta}) := \int_{\omega_{\min}}^{\omega_{\max}} e_{CRE}(\boldsymbol{u}, \boldsymbol{\sigma}, \boldsymbol{\theta}) z(\omega) d\omega \tag{4.7}$$

Based on the equations above, the damage identification problem is formulated as

$$\begin{aligned} &\arg\min \hat{F}(\boldsymbol{u}, \boldsymbol{\sigma}, \boldsymbol{\theta}) \\ &\text{subject to } \boldsymbol{u} \in \mathcal{U}, \boldsymbol{\sigma} \in \Im, \boldsymbol{\theta} \in \mathcal{A}, \boldsymbol{u} = \hat{\boldsymbol{u}}_k, k \in \wp \end{aligned} \tag{4.8}$$

where $\{\hat{\boldsymbol{u}}_k, k \in \wp\}$ is the incomplete frequency response data measured by finite sensors on the set of points $\{k \in \wp\}$. Equation (4.8) is known as the min-CRE principle for inverse identification problems [40, 43] and $\hat{F}(\boldsymbol{u}, \boldsymbol{\sigma}, \boldsymbol{\theta})$ is known as the CRE objective function. For each frequency ω_i, $z(\omega_i)$ is taken equally herein. The CRE function is chosen as the objective function in this research due to the following crucial features,

- Separate convexity: the separately convex property of the proposed objective function is of critical importance for the application of the alternating minimization(AM) method because only then, each alternating step become well-posed[49]. (Refer to section 4.2.2)

- Decoupling with respect to the damage parameters: under the constant stiffness assumption in every element, the CRE objective function is decoupled with respect to the damage parameters, or specifically, minimization of the CRE objective function over the damage parameters gives rise to a series of single-variable minimization problems. With the decoupled objective function, the sparse regularization, which is to be introduced later, will be easily tackled by the closed-form solution with little additional computational efforts. (Refer to section 4.2.2)

4.1.3 Discrete formulation of the CRE function

In the following, the inverse identification problem is solved in a finite element environment which requires to discretize the CRE objective function at first. A typical finite element, e, is defined by local nodes $i, j, k, ...$ and for each frequency, the displacement $\boldsymbol{u}$ and stress $\boldsymbol{\sigma}$ and the trial counterparts $\delta\boldsymbol{u}$ and $\delta\boldsymbol{\sigma}$ within the element e is approximated as

$$\begin{cases} \boldsymbol{u} \approx \boldsymbol{N}_1 \tilde{\boldsymbol{u}}^e, \ \delta u \approx \boldsymbol{N}_1 \delta \tilde{\boldsymbol{u}}^e \\ \boldsymbol{\sigma} \approx \boldsymbol{N}_2 \tilde{\boldsymbol{q}}^e = \boldsymbol{N}_2 \tilde{\boldsymbol{q}}_0^e + \boldsymbol{N}_2 \tilde{\boldsymbol{q}}_p^e, \ \delta\boldsymbol{\sigma} \approx \boldsymbol{N}_2 \delta \tilde{\boldsymbol{q}}^e = \boldsymbol{N}_2 \delta \tilde{\boldsymbol{q}}_0^e \end{cases} \tag{4.9}$$

where $\boldsymbol{N}_1$ and $\boldsymbol{N}_2$ are called shape functions (or interpolation functions) corresponding to nodal displacement vector $\tilde{\boldsymbol{u}}^e$ and nodal force vector $\tilde{\boldsymbol{q}}^e$ separately. The nodal force $\tilde{\boldsymbol{q}}^e$, obtained from a mathematical integration of stress $\boldsymbol{\sigma}$, is dynamically equivalent to the addition of the boundary forces $\tilde{\boldsymbol{q}}_p^e$ and the remaining homogeneous forces $\tilde{\boldsymbol{q}}_0^e$. As is noteworthy, the inhomogeneous part $\boldsymbol{N}_2^p \tilde{\boldsymbol{q}}_p^e$ vanish in the virtual stress $\delta\boldsymbol{\sigma}$. Additionally, the nodal force $\tilde{\boldsymbol{q}}^e$ should contain the same number of components as the corresponding nodal displacement $\tilde{\boldsymbol{u}}^e$ and be ordered in the appropriate corresponding directions. For three-dimensional beam elements, details on the expressions for the nodal displacement vector $\tilde{\boldsymbol{u}}^e$ and the nodal force vector $\tilde{\boldsymbol{q}}^e$ and the derivation for the shape functions $\boldsymbol{N}_1$ and $\boldsymbol{N}_2$ are given in **Appendix** A.

Using equations (4.1) and (4.2), one could also obtain the following expression.

$$\begin{cases} \boldsymbol{\varepsilon} = \boldsymbol{B}\boldsymbol{u} \approx \boldsymbol{B}\boldsymbol{N}_1 \tilde{\boldsymbol{u}}^e = \boldsymbol{B}_1 \tilde{\boldsymbol{u}}^e \\ \mathcal{L}\boldsymbol{\sigma} \approx \mathcal{L}\boldsymbol{N}_2 \tilde{\boldsymbol{q}}^e = \boldsymbol{B}_2 \tilde{\boldsymbol{q}}^e \end{cases} \tag{4.10}$$

With these preparations and further considering the CRE in equation (4.5), one can have the discrete form of the CRE as follows.

$$\begin{aligned} e_{CRE}(\tilde{\boldsymbol{u}}, \tilde{\boldsymbol{q}}, \boldsymbol{\theta}) = \frac{1}{2} \int_{\Omega} \big\{ & r_1 (\boldsymbol{N}_2 \tilde{\boldsymbol{q}} - \boldsymbol{D}(\boldsymbol{\theta}) \boldsymbol{B}_1 \tilde{\boldsymbol{u}})^T \boldsymbol{D}(\boldsymbol{\theta})^{-1} (\boldsymbol{N}_2 \tilde{\boldsymbol{q}} - \boldsymbol{D}(\boldsymbol{\theta}) \boldsymbol{B}_1 \tilde{\boldsymbol{u}}) + \\ & r_2 \, (\rho\omega^2)^{-1} (\boldsymbol{B}_2 \tilde{\boldsymbol{q}} + \boldsymbol{b} + \rho\omega^2 \boldsymbol{N}_1 \tilde{\boldsymbol{u}})^T (\boldsymbol{B}_2 \tilde{\boldsymbol{q}} + \boldsymbol{b} + \rho\omega^2 \boldsymbol{N}_1 \tilde{\boldsymbol{u}}) \big\} \, d\Omega \end{aligned} \tag{4.11}$$

As for the damage parameters $\boldsymbol{\theta}$, it is assumed to be linearly implicated in the elastic matrix $\boldsymbol{D}$, or in other words, the elastic matrix $\boldsymbol{D}$ is an affine function of the damage parameters θ, i.e., $\boldsymbol{D} = \boldsymbol{D}(\tilde{\boldsymbol{\theta}}) := \theta_e \boldsymbol{D}_e$ for element e where $\boldsymbol{D}_e$ is termed the elemental elastic matrix of the intact structure. Obviously, for an intact structure, there is $\tilde{\boldsymbol{\theta}} = \tilde{\boldsymbol{\theta}}_0 := [1; 1; ...; 1]$. As a result, equation(4.11) can be equally described as

$$\begin{aligned} e_{CRE}(\tilde{\boldsymbol{u}}, \tilde{\boldsymbol{q}}, \tilde{\boldsymbol{\theta}}) = \frac{1}{2} \sum_{e=1}^{N} \int_{\Omega^e} \big\{ & r_1 (\boldsymbol{N}_2 \tilde{\boldsymbol{q}}^e - \theta_e \boldsymbol{D}_e \boldsymbol{B}_1 \tilde{\boldsymbol{u}}^e)^T (\theta_e \boldsymbol{D}_e)^{-1} \\ & (\boldsymbol{N}_2 \tilde{\boldsymbol{q}}^e - \theta_e \boldsymbol{D}_e \boldsymbol{B}_1 \tilde{\boldsymbol{u}}^e) + r_2 (\rho\omega^2)^{-1} (\boldsymbol{B}_2 \tilde{\boldsymbol{q}}^e + \boldsymbol{b} + \rho\omega^2 \boldsymbol{N}_1 \tilde{\boldsymbol{u}}^e)^T \\ & (\boldsymbol{B}_2 \tilde{\boldsymbol{q}}^e + \boldsymbol{b} + \rho\omega^2 \boldsymbol{N}_1 \tilde{\boldsymbol{u}}^e) \big\} \, d\Omega \end{aligned} \tag{4.12}$$

With these notification, it is obvious that the CRE objective function (4.12) is decoupled with respect to the damage parameters $\tilde{\boldsymbol{\theta}}$, i.e., in every single equation of the equation (4.12), only one of the parameters $\tilde{\boldsymbol{\theta}}$ arises. Such a decoupling will act as a particular role in later analysis when the sparse regularization is considered.

4.2 Damage identification by min-CRE and sparse regularization

4.2.1 Sparse regularization

In practice, the amount of the measured data is always limited and this may make the damage identification problem ill-posed and very sensitive to the measurement noise. To circumvent the ill-posedness and improve the robustness, the sparse regularization technique is reasonably introduced. The main prerequisite is that the change of damage parameters $\tilde{\boldsymbol{\theta}} - \tilde{\boldsymbol{\theta}}_0$ must be sparse and no other information regarding the damage is required. By incorporating the sparse regularization into the objective function, the damage identification problem is reformulated as

$$F(\tilde{\boldsymbol{u}}, \tilde{\boldsymbol{q}}, \tilde{\boldsymbol{\theta}}) = \hat{F}(\tilde{\boldsymbol{u}}, \tilde{\boldsymbol{q}}, \tilde{\boldsymbol{\theta}}) + \lambda \parallel \boldsymbol{\Delta} \left(\tilde{\boldsymbol{\theta}} - \tilde{\boldsymbol{\theta}}_0 \right) \parallel_1^1 \tag{4.13}$$

where $\boldsymbol{\Delta} = \text{diag}\left([\Delta_1, ..., \Delta_N]\right)$ is the diagonal matrix of elemental length/area/ volume for beam/plate/solid element respectively. The ℓ_1-norm $\|\boldsymbol{x}\|_1 = \sum\limits_{e=1}^{N} |x_e|$ defines the sparse regularization term and $\lambda > 0$ is the corresponding regularization parameter which controls the trade-off between the sparsity and the residual norm. For detailed estimating the proper value of the regularization parameter λ, the reader is referred to Section 3.2.2. In the next section, the AM method is called to get the solution of the sparse-regularized CRE objective function (4.13).

4.2.2 AM method

In this section, the AM method is again proposed to practically solve this nonlinear optimization problem (4.13). Given the initial damage parameters $\tilde{\boldsymbol{\theta}}_0$ as those of the intact structure, the solution is obtained successively for $n = 1, 2, ...$ as follows

- step 1 (UMF step): Update the mechanical field $(\tilde{\boldsymbol{u}}, \tilde{\boldsymbol{q}})$ with the given damage parameters $\tilde{\boldsymbol{\theta}}^n$ for each given frequency

$$(\tilde{\boldsymbol{u}}^{n+1}, \tilde{\boldsymbol{q}}^{n+1}) = \arg \min_{\boldsymbol{u} \in \mathfrak{U}, \boldsymbol{\sigma} \in \mathfrak{S}, \boldsymbol{u} = \hat{\boldsymbol{u}}_k, k \in \wp} F(\tilde{\boldsymbol{u}}, \tilde{\boldsymbol{q}}, \tilde{\boldsymbol{\theta}}^n) \tag{4.14}$$

- step 2 (UDP step): Update the damage parameters $\tilde{\boldsymbol{\theta}}$ by the mechanical fields $(\tilde{\boldsymbol{u}}^{n+1}, \tilde{\boldsymbol{q}}^{n+1})$ obtained in step 1.

$$\tilde{\boldsymbol{\theta}}^{n+1} = \arg \min_{\tilde{\boldsymbol{\theta}}} F(\tilde{\boldsymbol{u}}^{n+1}, \tilde{\boldsymbol{q}}^{n+1}, \tilde{\boldsymbol{\theta}}) \tag{4.15}$$

UMF Step

The mechanical field $(\tilde{\boldsymbol{u}}, \tilde{\boldsymbol{q}})$ is recovered from the measured data and the given damage parameters $\tilde{\boldsymbol{\theta}}$ (given elastic matrix $\boldsymbol{D}$) individually for each given frequency. The sparse regularization term is not involved in this step. Specifically, the minimization over $\tilde{\boldsymbol{q}}$ yields the equation:

$$\begin{aligned} \int_\Omega \{ & r_1 \left(\boldsymbol{N}_2^T \boldsymbol{D}^{-1} \boldsymbol{N}_2 \tilde{\boldsymbol{q}} - \boldsymbol{N}_2^T \boldsymbol{B}_1 \tilde{\boldsymbol{u}} \right) + \\ & r_2 \left((\rho\omega^2)^{-1} \boldsymbol{B}_2^T \boldsymbol{B}_2 \tilde{\boldsymbol{q}} + \boldsymbol{B}_2^T \boldsymbol{N}_1 \tilde{\boldsymbol{u}} + (\rho\omega^2)^{-1} \boldsymbol{B}_2^T \boldsymbol{b} \right) \} = 0 \end{aligned} \tag{4.16}$$

and the minimization over $\tilde{\boldsymbol{u}}$ yields

$$\int_\Omega \left\{ r_1 \left(\boldsymbol{B}_1^T \boldsymbol{D} \boldsymbol{B}_1 \tilde{\boldsymbol{u}} - \boldsymbol{B}_1^T \boldsymbol{N}_2 \tilde{\boldsymbol{q}} \right) + r_2 \left(\rho\omega^2 \boldsymbol{N}_1^T \boldsymbol{N}_1 \tilde{\boldsymbol{u}} + \boldsymbol{N}_1^T \boldsymbol{B}_2 \tilde{\boldsymbol{q}} + \boldsymbol{N}_1^T \boldsymbol{b} \right) \right\} = 0 \tag{4.17}$$

From equations (4.16) and (4.17), the mechanical field $(\tilde{\boldsymbol{u}}, \tilde{\boldsymbol{q}})$ can be updated simultaneously. Moreover, equation (4.17) could be simplified as

$$\begin{pmatrix} (r_1 \boldsymbol{C}_0 + \frac{r_2}{\omega^2} \boldsymbol{H}_0) & \boldsymbol{A}_0 \\ \boldsymbol{A}_0^T & (r_1 \boldsymbol{K}_0 + r_2 \omega^2 \boldsymbol{M}_0) \end{pmatrix} \begin{pmatrix} \tilde{\boldsymbol{q}} \\ \tilde{\boldsymbol{u}} \end{pmatrix} = \begin{pmatrix} \boldsymbol{d}_1 \\ \boldsymbol{d}_2 \end{pmatrix} \tag{4.18}$$

where

$$
\begin{aligned}
\boldsymbol{C} &= \int_\Omega \boldsymbol{N}_2^T \boldsymbol{D}^{-1} \boldsymbol{N}_2 d\Omega, \\
\boldsymbol{H} &= \int_\Omega \frac{1}{\rho} \boldsymbol{B}_2^T \boldsymbol{B}_2 d\Omega, \\
\boldsymbol{M} &= \int_\Omega \rho \boldsymbol{N}_1^T \boldsymbol{N}_1 d\Omega, \\
\boldsymbol{K} &= \int_\Omega \boldsymbol{B}_1^T \boldsymbol{D} \boldsymbol{B}_1 d\Omega, \\
\boldsymbol{A} &= \int_\Omega \left(-r_1 \boldsymbol{N}_2^T \boldsymbol{B}_1 + r_2 \boldsymbol{B}_2^T \boldsymbol{N}_1\right) d\Omega, \\
\boldsymbol{d}_1 &= \int_\Omega \left\{-r_2(\rho\omega^2)^{-1} \boldsymbol{B}_2^T \boldsymbol{b} - \left(r_1 \boldsymbol{N}_2^T \boldsymbol{D}^{-1} \boldsymbol{N}_2 + r_2 (\rho\omega^2)^{-1} \boldsymbol{B}_2^T \boldsymbol{B}_2\right) \tilde{\boldsymbol{q}}_p\right\} d\Omega, \\
\boldsymbol{d}_2 &= \int_\Omega \left\{-r_2 \boldsymbol{N}_1^T \boldsymbol{b} - \left(-r_1 \boldsymbol{B}_1^T \boldsymbol{N}_2 + r_2 \boldsymbol{N}_1^T \boldsymbol{B}_2\right) \tilde{\boldsymbol{q}}_p\right\} d\Omega.
\end{aligned}
\tag{4.19}
$$

In equation (4.19), $\boldsymbol{A}_0$, $\boldsymbol{C}_0$, $\boldsymbol{K}_0$, $\boldsymbol{M}_0$ and $\boldsymbol{H}_0$ are the reduced forms of $\boldsymbol{A}$, $\boldsymbol{C}$, $\boldsymbol{K}$, $\boldsymbol{M}$ and $\boldsymbol{H}$ after applying the homogeneous boundary conditions.

To enforce the incomplete measured data, the displacements vector $\tilde{\boldsymbol{u}}$ will now be partitioned symbolically into unmeasured displacement $\tilde{\boldsymbol{u}}^U$ and measured displacement $\hat{\boldsymbol{u}}^M$. For the sake of convenience, in the following equations superscript U and M represent the corresponding unmeasured and measured DOFs of the array respectively. As a result, equation (4.18) can be rewritten as

$$
\boldsymbol{L}(\tilde{\boldsymbol{\theta}}) \left(\tilde{\boldsymbol{q}}^{\mathrm{T}}, \left(\tilde{\boldsymbol{u}}^U\right)^{\mathrm{T}}\right)^{\mathrm{T}} = \boldsymbol{S}(\tilde{\boldsymbol{\theta}}) \tag{4.20}
$$

where

$$
\begin{aligned}
\boldsymbol{L}(\tilde{\boldsymbol{\theta}}) &= \begin{pmatrix} r_1 \boldsymbol{C}_0 + \frac{r_2}{\omega^2} \boldsymbol{H}_0 & \boldsymbol{A}_0 \\ \boldsymbol{A}_0^{TU\cdot} & \left(r_1 \boldsymbol{K}_0 + r_2 \omega^2 \boldsymbol{M}_0\right)^{UU} \end{pmatrix}, \\
\boldsymbol{S}(\tilde{\boldsymbol{\theta}}) &= \left(\boldsymbol{d}_1^{\mathrm{T}}, \left(\boldsymbol{d}_2'^U\right)^{\mathrm{T}}\right)^{\mathrm{T}}, \\
\boldsymbol{d}_2'^U &= \boldsymbol{d}_2^U - \left(r_1 \boldsymbol{K}_0 + r_2 \omega^2 \boldsymbol{M}_0\right)^{UM} \hat{\boldsymbol{u}}^M
\end{aligned}
\tag{4.21}
$$

UDP Step

Due to the decoupling of the CRE objective function (4.7) as mentioned in Section4.1.4, the UDP step is tackled by solving a series of single-variable optimization problems, that is, minimization of equation (4.13) with respect to θ_e for each element $e\,(e = 1, 2, ..., N)$ takes the form

$$\begin{aligned}&\int_{\Omega^e} \frac{r_1}{2}\left\{(\boldsymbol{N}_2\tilde{\boldsymbol{q}}^e)^T \frac{(\boldsymbol{D}_e)^{-1}}{(\theta_e)^2}(\boldsymbol{N}_2\tilde{\boldsymbol{q}}^e) - (\boldsymbol{B}_1\tilde{\boldsymbol{u}}^e)^T \boldsymbol{D}_e(\boldsymbol{B}_1\tilde{\boldsymbol{u}}^e)\right\}dx \\ &- \lambda\Delta^e\{\mathrm{sign}(\theta_e - 1)\}dx = 0.\end{aligned} \tag{4.22}$$

Finally, one has

$$\theta_e = \begin{cases} \sqrt{\dfrac{b_e}{a_e + \lambda\Delta^e}}\ , \text{if } \lambda < \Lambda_e \\ \sqrt{\dfrac{b_e}{a_e - \lambda\Delta^e}}\ , \text{if } \lambda < -\Lambda_e \\ 1\ , \text{if } \lambda \geq |\Lambda_e| \end{cases}, \quad e = 1, 2, ..., N \tag{4.23}$$

where

$$\begin{aligned}\Lambda_e &= \frac{1}{\Delta^e}\int_{\Omega_e} \frac{r_1}{2}\left\{(\boldsymbol{N}_2\tilde{\boldsymbol{q}}^e)^T (\boldsymbol{D}_e)^{-1} (\boldsymbol{N}_2\tilde{\boldsymbol{q}}^e) - (\boldsymbol{B}_1\tilde{\boldsymbol{u}}^e)^T \boldsymbol{D}_e(\boldsymbol{B}_1\tilde{\boldsymbol{u}}^e)\right\} d\Omega \\ &= \frac{1}{\Delta^e}(b_e - a_e)\end{aligned} \tag{4.24}$$

and

$$a_e = \int_{\Omega_e} \frac{r_1}{2}(\boldsymbol{B}_1\tilde{\boldsymbol{u}}^e)^T \boldsymbol{D}_e(\boldsymbol{B}_1\tilde{\boldsymbol{u}}^e)d\Omega,\ b_e = \int_{\Omega_e} \frac{r_1}{2}(\boldsymbol{N}_2\tilde{\boldsymbol{q}}^e)^T (\boldsymbol{D}_e)^{-1} (\boldsymbol{N}_2\tilde{\boldsymbol{q}}^e)d\Omega \tag{4.25}$$

Detailed explanations of Λ_e are discussed in the next section. Based on equation (4.23) , the value of θ_e is found to be prone to be unchanged from the initial value 1 when $|\Lambda_e| \leq \lambda$ while θ_e begin to deviate from 1 to $\hat{\theta}_e$ when $|\Lambda_e| \geq \lambda$. That is to say, the regularization parameter λ determines whether damage occurs: as long as $\lambda < |\Lambda_e|$, the eth element would admit stiffness change or damage; otherwise if $\lambda \geq |\Lambda_e|$, the damage would be found to not occur in the eth element.

Moreover, from equations (4.22) and (4.23), the sparse regularization term would introduce little computational complexity and the minimization over each damage parameter along with the sparse regularization term is solved immediately by the closed-form solution in equation (4.23). This advantage benefits from the decoupling of the CRE objective function with respect to the damage parameters.

4.2.3 Summary of the proposed damage identification approach

By combining the UMF step in Section 4.2.2 and the UDP step in Section 4.2.2, using the proposed threshold setting method so as to estimate the optimal regularization parameter λ in Section 3.2.2, the damage identification algorithm by min-CRE and sparse regularization can be established as shown in **Table 4.1**. It should be noted that different analysis models could be applied in the UMF step and the UDP step. In the UMF step, more elements are recommended so as to avoid the discretization error for the mechanical field analysis, while less elements could be used in the UDP step to mitigate the ill-posed problem if acquiring less damage parameters. Nevertheless, as the sparse regularization could indeed circumvent the possible ill-posedness caused by more damage parameters, refined elements for the UDP step is also possible in the proposed damage identification approach, which would be illustrated in the following numerical examples.

4.3 Numerical verification

In the following, three numerical simulations are used to test the proposed sparse-regularized min-CRE approach using FRF data. Damage identification results obtained by three identification approaches are compared in Section 4.3.1 and Section 4.3.2, namely the min-CRE approach with sparse regularization (C1), the sensitivity approach with Tikhonov regularization (S2) and the sensitivity approach with sparse regularization (S1). The advantage of being efficient for the proposed min-CRE approach is strongly substantiated. The example in Section 4.3.1 further considers some modeling errors in the mass matrix so as to testify the robustness of the identification results. Section 4.3.3 shows that the sparse regularization can significantly improve the accuracy of the identification results for a more general three-dimensional structure. For application of the iteration algorithm, the convergence tolerance is practically set to TOL$= 1 \times 10^{-6}$.

4.3.1 Simply supported beam structure

In this example, a simply supported beam is utilized to compare the accuracy and efficiency between the proposed min-CRE approach and sensitivity approaches with

Table 4.1 Summery of the proposed AM method

Initial algorithm setting
◦ set initial damage parameters $\tilde{\boldsymbol{\theta}}_{(0)} = \tilde{\boldsymbol{\theta}}_0$ as those of the intact structure ◦ set values of the maximum threshold setting rank l_{max} and the discriminating ratio α for the threshold setting method ◦ define the convergence tolerance TOL and the maximum number of iterations Z_{max} ◦ load the measured FRF data
Alternating minimization approach (for $j = 1 : Z_{max}$)
◦ Refer to the UMF step in Section 4.2.2 to obtain the updating mechanical field $(\tilde{\boldsymbol{q}}, \tilde{\boldsymbol{u}}^U)^T_{(j)} = \boldsymbol{L}(\tilde{\boldsymbol{\theta}}_{(j-1)})^{-1}\boldsymbol{S}(\tilde{\boldsymbol{\theta}}_{(j-1)})$ ◦ Choose the optimal regularization parameter λ_{est} according to the threshold setting method in Section 3.2.2 from – for $e = 1 : N$ – $a_e = \int_{\Omega_e} \frac{r_1}{2}(\boldsymbol{B}_1\tilde{\boldsymbol{u}}^e_{(j)})^T\boldsymbol{D}_e(\boldsymbol{B}_1\tilde{\boldsymbol{u}}^e_{(j)})d\Omega$, – $b_e = \int_{\Omega_e} \frac{r_1}{2}(\boldsymbol{N}_2\tilde{\boldsymbol{q}}^e_{(j)})^T\,(\boldsymbol{D}_e)^{-1}\,(\boldsymbol{N}_2\tilde{\boldsymbol{q}}^e_{(j)})d\Omega$ – $\Lambda_e = \frac{1}{\Delta^e}\,(b_e - a_e)$, end for – $\lambda_{\text{est}} = \text{TSM}(\boldsymbol{\Lambda}, l_{\text{max}}, \alpha)$ ◦ Refer to the UDP step in Section 4.2.2 to obtain the updating damage parameter $\theta_{e(j)}$ for each element: – if $\lambda_{\text{est}} < \Lambda_e$ then $\theta_{e(j)} = \sqrt{\frac{b_e}{a_e+\lambda_{\text{est}}\Delta^e}}$, – else if $\lambda_{\text{est}} < -\Lambda_e$ then $\theta_{e(j)} = \sqrt{\frac{b_e}{a_e-\lambda_{\text{est}}\Delta^e}}$, – else $\theta_{e(j)} = \theta_{e0} = 1$ ◦ Convergence criterion – if $\parallel \tilde{\boldsymbol{\theta}}_{(j)} - \tilde{\boldsymbol{\theta}}_{(j-1)} \parallel / \parallel \tilde{\boldsymbol{\theta}}_{(0)} \parallel \leq$ TOL break.

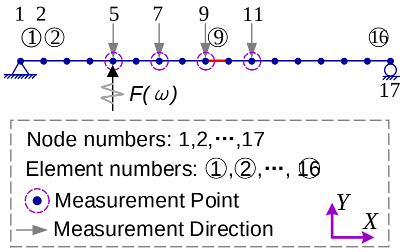

Figure 4.1 Model of simply supported beam structure

different regularization techniques. The total length of the beam is 1m and the mass-per-length and bending stiffness are estimated as 1kg/m and 1Nm^2, respectively. As with finite element modelling, the beam is uniformaly divided into 16 Eular-Bernoulli beam elements with 17 nodes each with two degrees of freedom (see **Figure 4.1** for more details). The damage scenario admits the damage in element 9 with 20% stiffness reduction (damage parameter $\tilde{\theta}_0 = 0.8$). The measurement points are chosen to be node 5, 7, 9 and 11 (Y direction only). The selected frequency range is simply chosen to be $[1, 80]$Hz with 1Hz intervals. For a more complicated model, an appropriate choice of the selected frequency range could improve the identification results greatly. Detailed selecting rules are discussed in Section 4.2. The measured FRF data at kth selected excitation frequency is obtained from simulation with addition of the measurement noise as follows,

$$\text{noise}_k(s) = randn \cdot a \cdot d_k(s), k = 1, 2, \dots m \tag{4.26}$$

where $randn$ is the normal distribution with zero mean and unit deviation, a is the applied noise level and $d_k(s)$ is the measurement FRF data at certain position s. Noise level of 10% (SNR=10dB) is considered in this example. For excitation, an unit harmonic load as shown in **Figure 4.1** is enforced at node 5.

On choice of (l_{max}, α) in the threshold setting method

To have an impression on how the maximum threshold setting rank $l_{\max}$ and the discriminating ratio α work in the threshold setting method, different choices of $(l_{\max}, \alpha)$ for damage identification in different noise levels are studied herein and detailed results are displayed in **Figure 4.2**. On one hand, the identification process tends to be reasonably robust for a broad selection of (l_{max}, α) with appropriate ranges of $\alpha \in [2, 50]$ and $l_{\max} \in [2, 10]$ for the case with low level of noise (**Figure 4.2**(a), (b)). On the

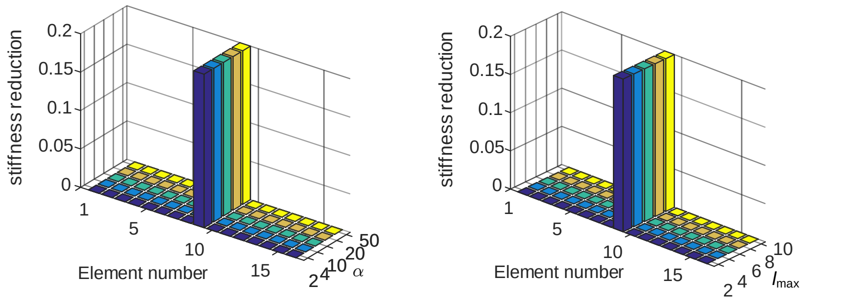

(a) Fixing l_{max} =5 and varying α (no noise) (b) Fixing α =4 and varying l_{max} (no noise)

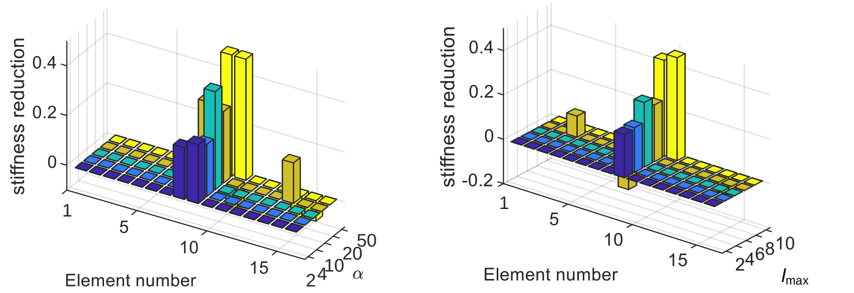

(c) Fixing l_{max} =5 and varying α (10% noise) (d) Fixing α =4 and varying l_{max} (10% noise)

Figure 4.2 Damage identification results under different choice of (l_{max}, α)

other hand, the choice of $(l_{\max}, \alpha)$ should be paid more attention for the case with high level of noise (**Figure 4.2**(c), (d)). Damage locations are badly identified for $\alpha = 2$ and $\alpha \geq 20$. This means that the discriminating ratio α should not be too small or too large. In terms of the maximum threshold setting rank $l_{\max}$, $l_{\max} \geq 8$ leads to the failure of damage identification, indicating that $l_{\max}$ shall not be too large. As a result, in the following of this example, the threshold parameters are reasonably fixed at $l_{\max} = 5$, $\alpha = 4$.

Comparison to the results by sensitivity-based algorithms

In this section, the following sensitivity-based algorithm, representing probably the most widely used techniques on the use of FRF data is considered.

Normally, the damage identification process based on the sensitivity approach is formulated as minimization of the following objective function-weighted least squares of the error in measured quantities,

$$\arg\min \parallel \hat{\boldsymbol{R}} - \boldsymbol{R}(\boldsymbol{\theta}) \parallel_{\boldsymbol{W}}^2 \tag{4.27}$$

Table 4.2 Sensitivity-based identification approaches with different regularizations

Approach	Objective function for each iteration	Solution method for each iteration	Parameter estimation method
S2[65]	$\parallel \Delta\boldsymbol{R}(\bar{\boldsymbol{\theta}}) - \boldsymbol{S}(\bar{\boldsymbol{\theta}})\Delta\boldsymbol{\theta} \parallel_{\boldsymbol{W}}^2 + \lambda \parallel \Delta\boldsymbol{\theta} \parallel_2^2$	closed-form solution $\Delta\boldsymbol{\theta} = \left[\boldsymbol{S}(\bar{\boldsymbol{\theta}})^T \boldsymbol{W} \boldsymbol{S}(\bar{\boldsymbol{\theta}}) + \lambda \boldsymbol{I}\right]^{-1} \boldsymbol{S}(\bar{\boldsymbol{\theta}})^T \boldsymbol{W} \Delta\boldsymbol{R}(\bar{\boldsymbol{\theta}})$	L-curve method
S1[38]	$\parallel \Delta\boldsymbol{R}(\bar{\boldsymbol{\theta}}) - \boldsymbol{S}(\bar{\boldsymbol{\theta}})\Delta\boldsymbol{\theta} \parallel_{\boldsymbol{W}}^2 + \lambda \parallel \Delta\boldsymbol{\theta} \parallel_1^1$	Primal-dual interior point method *Newton's method proceeds*	Using residual and solution norms[66]

where $\hat{\boldsymbol{R}}$ and $\boldsymbol{R}(\boldsymbol{\theta})$ denote the measured and analytically predicted outputs respectively. $\boldsymbol{W}$ is the positive definite weight matrix. Linearization of the above non-linear problem (4.27) at given $\bar{\boldsymbol{\theta}}$ for iterative method is as follows

$$\hat{\boldsymbol{R}} - \boldsymbol{R}(\boldsymbol{\theta}) = \Delta\boldsymbol{R}(\bar{\boldsymbol{\theta}}) - \boldsymbol{S}(\bar{\boldsymbol{\theta}})\Delta\boldsymbol{\theta} \tag{4.28}$$

where $\Delta\boldsymbol{\theta} := \boldsymbol{\theta} - \bar{\boldsymbol{\theta}}$ is the update of $\boldsymbol{\theta}$, $\Delta\boldsymbol{R}(\bar{\boldsymbol{\theta}}) := \hat{\boldsymbol{R}} - \boldsymbol{R}(\bar{\boldsymbol{\theta}})$ is the residual and $\boldsymbol{S}(\bar{\boldsymbol{\theta}})$ is the response sensitivity matrix. For the method using frequency response function, the mathematical formulation of $\boldsymbol{R}(\boldsymbol{\theta})$ and the eth column of sensitivity matrix $\boldsymbol{S}$ are often expressed as [65]:

$$\boldsymbol{R}(\boldsymbol{\theta}) = \left[-\omega^2 \boldsymbol{M}(\boldsymbol{\theta}) + \boldsymbol{K}(\boldsymbol{\theta})\right] \hat{\boldsymbol{u}}^M \tag{4.29}$$

$$\boldsymbol{S}_e = \left.\frac{\partial \boldsymbol{R}(\boldsymbol{\theta})}{\partial \theta_e}\right|_{\theta=\bar{\theta}} = \left[-\omega^2 \frac{\partial \boldsymbol{M}}{\partial \theta_e} + \frac{\partial \boldsymbol{K}}{\partial \theta_e}\right]_{\theta=\bar{\theta}} \hat{\boldsymbol{u}}^M \tag{4.30}$$

where $\hat{\boldsymbol{u}}^M$ represents the measured frequency-domain displacement response. Static condensation is needed so as to condense the above equation to the measured degrees of freedom and the weighting matrix $\boldsymbol{H}(\omega, \bar{\theta})$, the frequency response function matrix should also be considered so as to reduce the bias on the estimated parameters. To circumvent the ill-posed problem, regularization is required. Objective function, solution method for each iteration and regularization parameter estimation method for different regularization types are briefly summarized in **Table 4.2**.

The final identification results are presented in **Figure 4.3**. As is seen, all of these three approaches can well identify the damage location and extent in the beam through 10% noise level, except that false positions, although with minor degree, are also observed by the sensitivity approach with Tikhonov regularization (S2). Many researches have shown that Tikhonov regularization tends to produce over-smooth solutions because the quadratic regularizer cannot recover the sparse features of the solution.

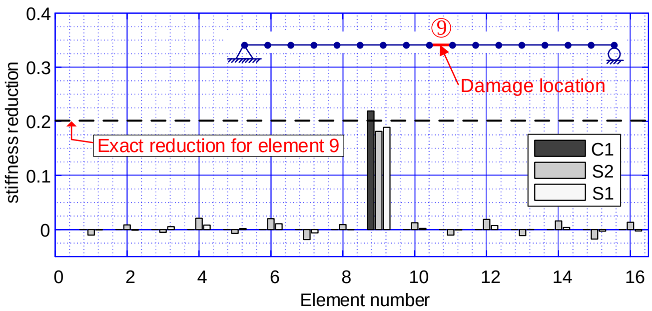

Figure 4.3 Stiffness reduction for each element using different approaches

Table 4.3 Convergence property for different identification approaches

Approach	Numbers of iterations	Total computation time (s)
C1	24	0.51
S2	6	5.41
S1	-	899.47
S1(with known λ)	9	4.89

Regarding the corresponding convergence property in **Table 4.3**, it is shown that the computational effort necessary to solve C1(0.51s) is much less than the sensitivity approaches(4.89s-899.47s), although it takes more steps for C1 to get convergent. This advantage attributes to the inherent decoupling nature of the CRE function with respect to the damage parameters, making every parameter-update-step solved as a series of single-variable optimization problems. It should be noted that due to the lack of closed-form solution for regularization parameter estimation, the computational time for S1 is huge(899.47s). For S1 with unknown λ, an appropriate range of $\lambda(2.9 - 5.4)$ is picked up by achieving balance between the residual norm and solution norm [66] as shown in **Figure 4.4**(b). With the properly chosen or experienced-based λ, the computational cost of S1 could be reduced significantly(4.89s).

Considering modelling errors

With respect to the modeling errors, simple mass modeling errors are added to the simulated beam structure. To do so, the exact mass density of element 2, 3 and 12, which are involved into the generation of the measured FRF data through simulation, are changed to 1.05kg/m, 1.05kg/m and 0.95kg/m respectively, while the mass density

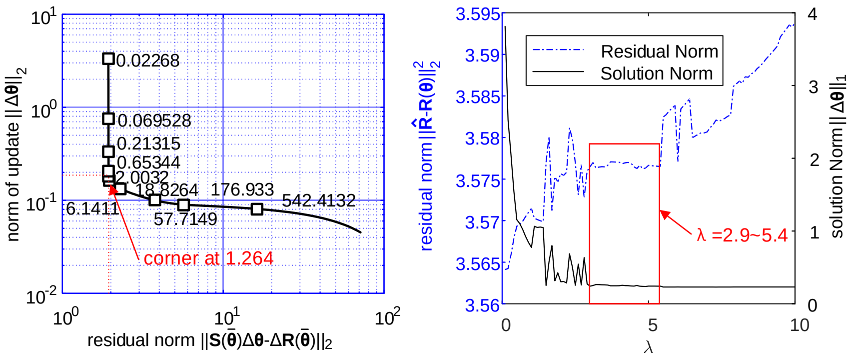

Figure 4.4 Regularization parameter selection: (a) L-curve method for Tikhonov regularization; (b) using residual and solution norms for sparse regularization

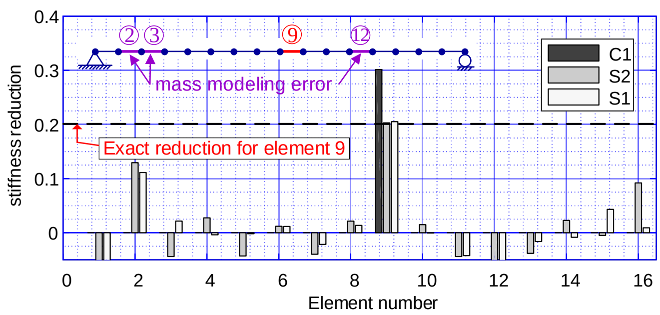

Figure 4.5 Stiffness reduction for each element using different approaches with mass modeling errors

for damage identification are still set to be 1kg/m as before. Noise level of 10% is also added into the measured FRF data. The identification results obtained by the three approaches are shown in **Figure 4.5**. As could be seen, the present approach (C1) could still identify the damage location clearly, although with a less satisfactory damage extent assessment. However, this bias can be further revised if needed by simply fixing the damage location and optimizing the extent to match the observed changes. For the sensitivity-based approaches (S2&S1), the modelling errors may deteriorate the damage identification if no additional improvement, such as optimizing the weight matrix through the model error covariance [67], is enforced.

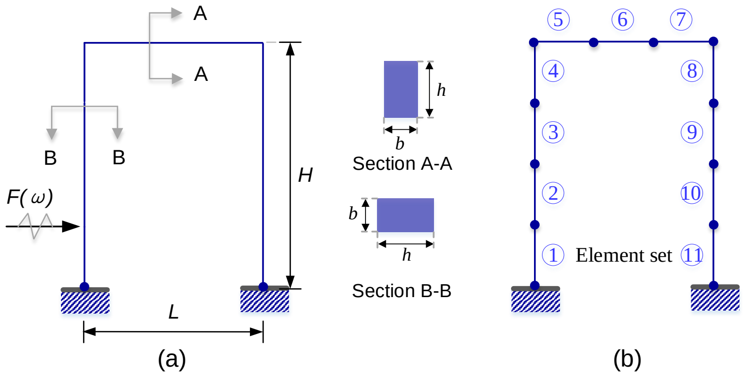

Figure 4.6 Model of plane frame structure: (a)Geometry, (b)Element sets

4.3.2 Plane frame structure

A plane frame structure as shown in **Figure 4.6** is studied in the second example (see reference [14] for detailed explanation on the target structure). The height and width of the frame are $H = 1.2\text{m}$ and $L = 0.6\text{m}$, respectively, and the rectangular cross-sectional dimensions are $b = 0.01\text{m}$ and $h = 0.02\text{m}$ with the inertial moment for planar bending $I = 6.67 \times 10^{-9}\text{m}^4$ and area $A = 2 \times 10^{-4}\text{m}^2$. For the undamaged frame, the mass density of the material is $\rho = 2.7 \times 10^3\text{kg/m}^3$, the Poisson's ratio is $\nu = 0.3$ and the Young's modulus is $E = 6.9 \times 10^{10}\text{N/m}^2$. The plane frame analysis model consists of 88 Euler-Bernoulli beam elements with 89 nodes, each with three degrees of freedom. This finer numerical model is used to obtain the mechanical field for the UMF step so that the discretization error caused by finite element model could be ignored. For the UMP step, the structure is divided in 11 sets of elements (see **Figure 4.6**(b)) and the identification procedure updates the 11 element parameters independently. A single harmonic load is applied in the x-direction of node 2. The FRF data are obtained by the discrete Fourier transform(DFT) of the corresponding numerical simulated accelerations (see **Figure 4.7** for the FRF data of node 2).

Twelve damage scenarios, including single and multiple, small and large damage, unpolluted and polluted measurements are taken into account, as listed in **Table 4.4**, where Nil stands for no noise. The measurement locations and the corresponding directions are also illustrated in **Table 4.4** and **Figure 4.8**. Herein, the stiffness parameters $\{\theta_e,\ e = 1, 2, \ldots, N\}$, standing for the Young's modulus of each element set, is identified and the identified results in the percentage error forms are presented

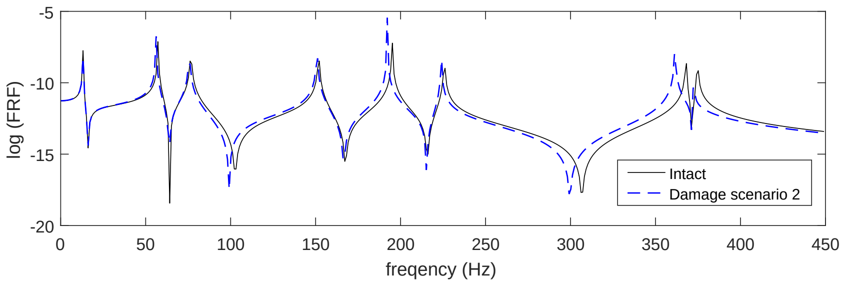

(a) Scenario 2

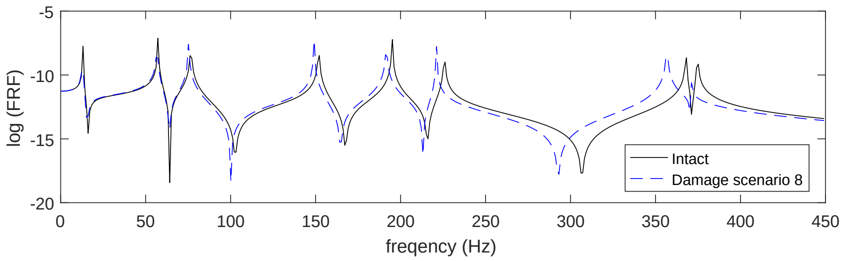

(b) Scenario 8

Figure 4.7 FRF of the plane frame structure in the x-direction of node 2

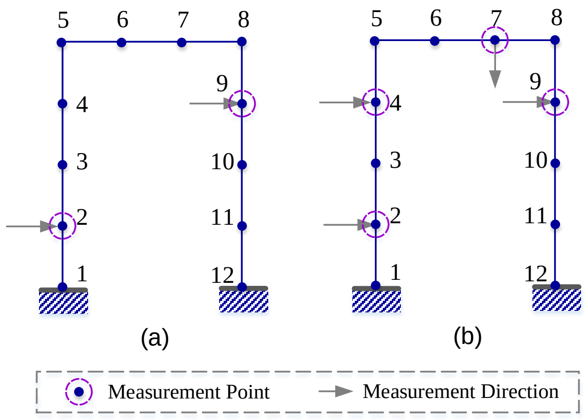

Figure 4.8 Measurement points and directions

Table 4.4 Damage scenarios for plane frame structure

Damage scenario scenario	Damage location (element set no.)	Reduction in elastic modulus (%)	Noise (%)	Measurement
1	3	10	Nil	a_{x2}, a_{x9}
2	3	20	Nil	a_{x2}, a_{x9}
3	3	40	Nil	a_{x2}, a_{x9}
4	3	10	10	a_{x2}, a_{x9}
5	3	20	10	a_{x2}, a_{x9}
6	3	40	10	a_{x2}, a_{x9}
7	4,5	10,5	Nil	a_{x2},a_{x4},a_{x9},a_{y7}
8	4,5	20,25	Nil	a_{x2},a_{x4},a_{x9},a_{y7}
9	4,5	50,50	Nil	a_{x2},a_{x4},a_{x9},a_{y7}
10	4,5	10,5	10	a_{x2},a_{x4},a_{x9},a_{y7}
11	4,5	20,25	10	a_{x2},a_{x4},a_{x9},a_{y7}
12	4,5	50,50	10	a_{x2},a_{x4},a_{x9},a_{y7}

as

$$\text{Relative error}(\%) = \frac{\theta_e^{id} - \theta_e}{\theta_e} \times 100\% \tag{4.31}$$

where θ_e^{id} and θ_e are identified and true values of the stiffness parameter for each element set, respectively. Noise level of 10% (SNR=10dB) is added to the measurements primarily.

Several practical rules for selecting excitation frequencies are

- Excitation frequencies should not be selected at resonance frequencies to prevent resonance phenomena and high sensitivity to noise.

- Dynamic response of target structure is more sensitive to damages for frequency points close to resonances than points far from resonances. Therefore, excitation frequency points near resonance frequencies are recommended for measurement [62].

- Although the response of the target structure in higher frequency ranges, which excites higher mode shapes, is more sensitive to damages, numerical analysis results are shown with less accuracy than those in lower frequency ranges [68].

- Using more frequency ranges corresponding to different resonance frequencies could improve the identification accuracy while using more frequency points near

Table 4.5 Frequency ranges (Hz) with 4Hz interval (number of frequency points)

Scenarios					
1&4	2&5	3&6	7&10	8&11	9&12
50-82 (9)	50-82 (9)	46-82 (10)	46-74 (8)	50-82 (9)	50-82 (9)
143-147 (2)	143-147 (2)	139-143 (2)	139-143 (2)	139-143 (2)	127-135 (3)
157-161 (2)	153-157 (2)	157-161 (2)	157-161 (2)	157-161 (2)	149-161 (4)
169-185 (5)	165-185 (6)	169-181 (4)	169-185 (5)	169-185 (5)	165-177 (4)
199-215 (5)	195-219 (7)	195-211 (5)	199-219 (6)	195-215 (6)	187-203 (5)
230-262 (9)	226-258 (9)	226-258 (9)	230-262 (9)	226-258 (9)	215-251 (10)
316-352 (10)	316-352 (10)	308-336 (8)	316-352 (10)	316-348 (9)	300-316 (5)
382-410 (8)	378-394 (5)	386-422 (10)	382-410 (8)	382-410 (8)	378-402 (7)
total number=(50)	(50)	(50)	(50)	(50)	(47)

one resonance frequency seems to have no significantly effect on the results for lower noise level cases.

- For higher levels of noise, presence of more frequency points near certain resonance frequency can result in a robust identification.

Based on these rules, the selected frequency ranges are given in **Table 4.5** and the sampling frequency stepping size in each frequency range is 4Hz. Consequently, identification results of each scenario are obtained using 50 frequency points, except for scenarios 9&12, where 47 frequency points are used.

As is observed in **Table 4.6** with the relative error defined in equation (4.31), for the single damage scenarios 1-6, the proposed approach could provide satisfied identification results: the maximum relative error does not exceed 0.02% in the case of no noise and 1% in the case of 10% noise. Only the horizontal acceleration response at nodes 2 and 9 is measured herein. For the multiple damages scenarios 7-12, the horizontal frequency response at node 4 and the vertical acceleration response at node 7 are additionally measured. The identification by the min-CRE approach can well identify the damage locations as well as extents with a maximum relative error 0.01% in the case of no noise and 3.7% in the case of 10% noise.

Compared with the results in the reference [14], which used an enhanced response sensitivity approach with the Tikhonov regularization under the same measurement degrees of freedom, identification results of the min-CRE approach with the sparse regularization demonstrated the superiority for all of the 12 scenarios. Most of this

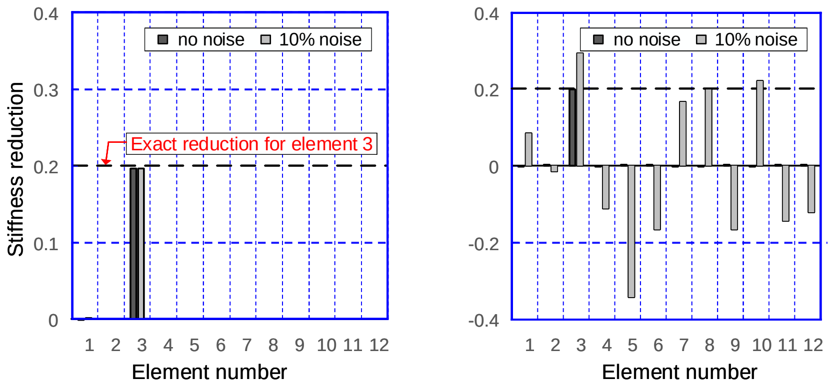

Figure 4.9 Stiffness reduction for scenario 2/5: (a) the min-CRE approach with sparse regularization; (b) the min-CRE approach without sparse regularization

superior identification accuracy is attributed to the enforced sparse regularization: the sparse regularization yields sparse damages that are more compatible with pratical damage patterns, while the Tikhonov-regularized damage identification does not result in sparse solutions, which typically have non-zero relative errors associated with all damage parameters [69]. All coincide with the existed observations where replacement of the Tikhonov regularization by the sparse regularization can indeed improve the identification accuracy and robustness for damage identification.

To get a better picture on the effectiveness of the sparse regularization, detailed identification results for scenario 5 with and without sparsity are shown in **Figure 4.9**. Obviously, when there is no measurement noise, using or not using sparse regularization would lead to the same good identification results. However, it is almost impossible to get to the reasonable identification results for the case without sparse regularization when measurement noise is enforced. It is clear that the sparse regularization greatly improves the identifiability and robustness of the CRE-approach. Furthermore, to visualize how the sparse-regularized min-CRE approach proceeds, the iterative procedure for the scenario 5 is shown in **Figure 4.10**. On the other hand, **Figure 4.11** compares the evolution of the constitutive relation error(CRE) for each of the iterative step with different levels of noise (0%, 5%, 10% and 20%) for damage scenario 5. As is observed, the error decreases with the number of iterations increases, verifying the convergence of the present method.

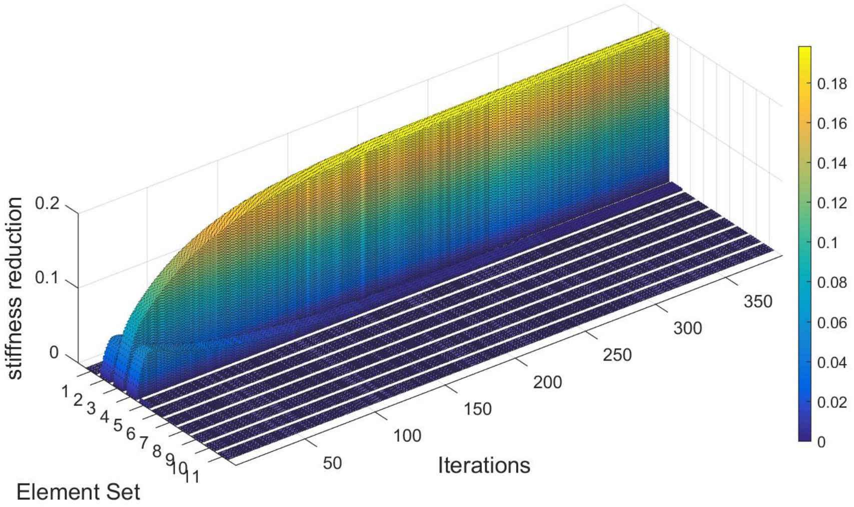

Figure 4.10 Damage identification procedure for scenario 5 of the plane frame structure

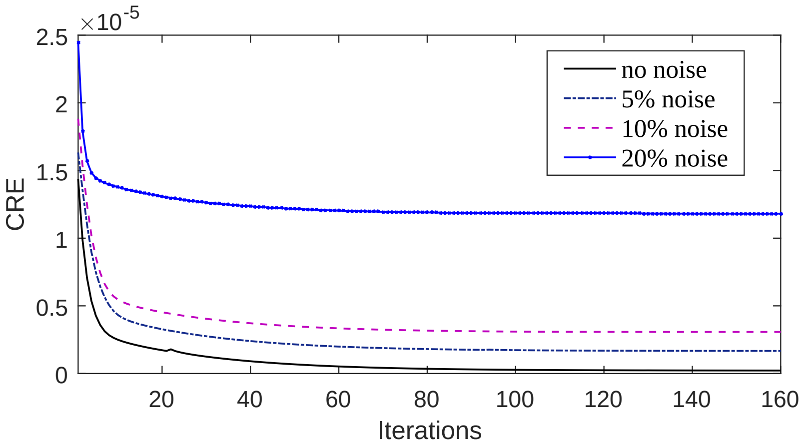

Figure 4.11 CRE vs iterations for damage scenario 5 with different levels of noise

Table 4.6 Error in the Young's modulus for each element set of damage scenarios 1-12

Damage	Error (%) in each element set by min-CRE approach											Error (%) in each element set by sensitivity approach										
scenario	1	2	3	4	5	6	7	8	9	10	11	1	2	3	4	5	6	7	8	9	10	11
1	-0.01	0.00	0.01	0.00	0.00	0.00	0.00	0.00	0.00	0.00	0.00	0.02	-0.10	-0.12	0.20	0.23	-0.05	-0.34	-0.05	0.26	0.00	-0.07
2	-0.01	0.00	0.02	0.00	0.00	0.00	0.00	0.00	0.00	0.00	0.00	0.07	-0.29	-0.43	0.59	0.75	-0.17	-1.38	0.01	0.96	-0.07	-0.21
3	0.00	0.00	0.01	0.00	0.00	0.00	0.00	0.00	0.00	0.00	0.00	0.02	-0.19	-0.25	0.60	0.25	-0.23	-1.59	0.31	1.05	-0.24	-0.14
4	0.00	0.00	-0.18	0.00	0.00	0.00	0.00	0.00	0.00	0.00	0.00	-0.08	1.81	0.82	-0.80	-2.70	-0.88	1.49	-0.32	-0.58	-1.10	0.83
5	-0.27	0.00	0.23	0.00	0.00	0.00	0.00	0.00	0.00	0.00	0.00	0.09	1.55	0.42	-0.44	-2.20	-1.12	1.47	0.34	0.59	-1.87	0.06
6	-1.00	0.00	0.45	0.00	0.00	0.00	0.00	0.00	0.00	0.00	0.00	0.02	0.73	0.52	1.70	-2.83	-0.85	-0.70	-0.21	2.06	-2.00	-0.21
7	0.00	0.00	-0.01	0.00	0.01	0.01	0.00	0.00	0.00	0.00	0.00	0.10	-0.26	-0.33	0.23	0.76	-0.04	-0.32	-0.24	0.29	0.13	-0.17
8	0.00	0.00	-0.01	0.00	0.01	0.01	0.00	0.00	0.00	0.00	0.00	0.10	-0.19	-0.35	0.14	0.75	-0.04	-0.20	-0.33	0.11	0.22	-0.10
9	0.00	0.00	0.00	0.01	0.00	0.00	0.00	0.00	0.00	0.00	0.00	0.02	-0.03	-0.10	-0.03	0.26	-0.01	0.13	-0.18	-0.11	0.11	0.00
10	0.00	0.00	0.00	1.01	2.57	0.00	-1.98	0.00	0.00	0.00	0.00	-0.61	0.95	1.83	-1.01	-2.71	0.66	0.73	0.36	-2.29	0.13	1.27
11	0.00	0.69	-1.74	-0.81	3.69	0.00	-1.70	0.00	0.00	2.60	0.00	-0.99	1.63	1.36	-2.25	-0.78	1.42	1.28	-0.76	-3.93	0.98	2.23
12	-1.26	0.00	0.00	3.42	-3.71	0.00	0.00	0.00	0.00	0.00	0.00	0.27	-0.52	-2.15	-0.19	4.82	-0.66	3.02	-2.22	-0.46	0.22	-0.45

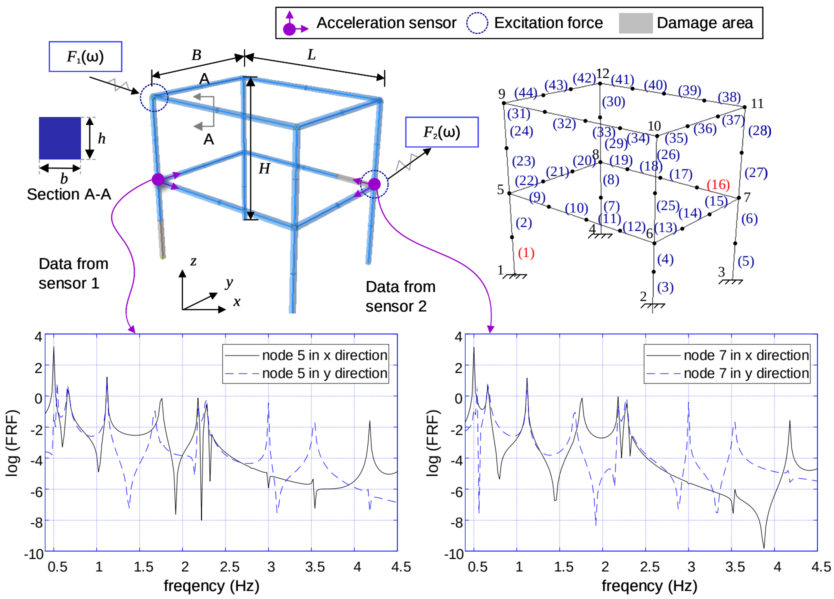

Figure 4.12 Schematic diagram showing the numerical structure and the directions of system output measurements and input excitations

4.3.3 Three-dimensional frame structure

The performance of the presented approach is also illustrated by using a three-dimensional structure. It is a 2-story, 1-bay by 1-bay frame structure as shown schematically in **Figure 4.12**. Parameters of this frame are: height $H = 4$m, length $L = 4$m, width $B = 3$m, rectangular cross-section $h \times b = 0.01\text{m} \times 0.01\text{m}$, intact Young's modulus $E = 2.1 \times 10^{11}$Pa, Poisson's ratio $\nu = 0.3$ and mass density $\rho = 7860\text{kg/m}^3$. Shear modulus G for this structure is taken as $E/(2(1+\nu))$ herein. Simulated dynamic FRF data are used in this study. Two synthetic harmonic load is applied at node 7 and node 9. Node 5(x,y direction) and node 7(x,y direction) are selected as two measurement points. These input data are contaminated by normal distribution noise with the noise level 10% (SNR=10dB) according to equation (4.26). The selected frequency range in this example is $[0.4, 4.5]$Hz with 0.05Hz intervals. Some of the excitation frequencies are ignored based on the selection rules as stated in Section 4.2. To clearly understand the spatial motion over the entire model, displacement fields for different frequencies are depicted in **Figure 4.13**.

Damages are enforced by reducing the Young's modulus E to 70% in element 1 ($\tilde{\theta}_1 = 0.7$) and 80% in element 16 ($\tilde{\theta}_{16} = 0.8$). As shown in **Figure 4.14**(a),

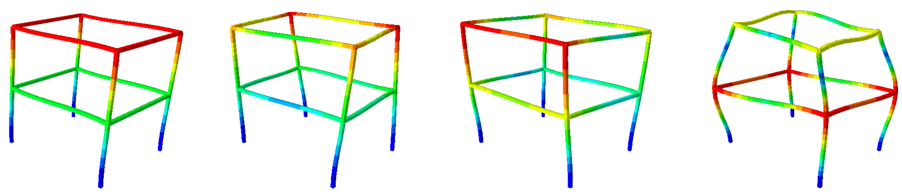

Figure 4.13 Displacement fields for different frequency

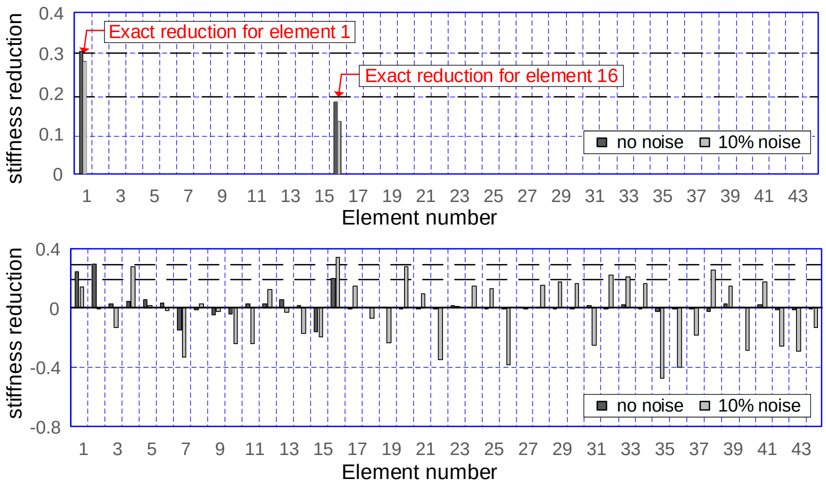

Figure 4.14 Stiffness reduction for each element: (a) the min-CRE approach with sparse regularization; (b) the min-CRE approach without sparse regularization

good identification performance is achieved when noise level is up to 10%. The optimal regularization parameters are $\lambda_{\text{est}} = 1.45422 \times 10^{-13}$ for the no noise case and $\lambda_{\text{est}} = 3.72452 \times 10^{-13}$ for the 10% noise case. Again, identification results with and without sparsity are additionally compared in **Figure 4.14**. From the results of the identified stiffness reduction under the measurement noise and without the sparse regularization (**Figure 4.14**(b)), damage locations and extents became almost unidentifiable, while the sparse regularization substantially improves the accuracy and robustness of the identification procedure (**Figure 4.14**(a)). The proposed damage identification approach with sparsity is shown to be well applicable to the identification in 3D frames.

To show the convergence of the proposed spare-regularized min-CRE approach,

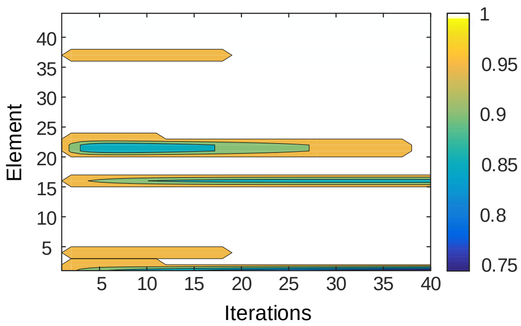

Figure 4.15 Contour plot of damage parameters for each element

filled contour plot of the damage parameters $\tilde{\boldsymbol{\theta}}$ was drawn in **Figure 4.15**. As it is seen, damages in Element 1 and element 16 are identified after 35 steps, verifying the convergence of the present method. Besides, escapes from local minima could also be found in Elements 21-23 and Element 37. Algorithm without sparsity would encounter divergence or convergence difficulty with the same amount of input measurement data. This phenomenon is attributable to the fact that sparse regularization provides a flexible and parsimonious reconstructing process for high-dimensional model parameters from limited incomplete input data.

4.4 Conclusions

This research is focused on the damage identification approach with incomplete frequency response data using the minimum constitutive relation error (min-CRE) principle and the sparse regularization. The identification process is a nonlinear optimization problem and the corresponding objective function is set to measure the residual of the constitutive equations connecting the admissible stress field and the admissible displacement field. Numerical examples are conducted to verify the present approach and the results show that:

1. The CRE function is chosen as the objective function due to its separate convexity and decoupling with respect to the damage parameters.

2. FRF data are more reliable and practical to provide abundant information at measured degrees of freedom and at a great number of desired frequencies.

3. Particular attention should be paid to properly select the frequency ranges of the FRF data.

4. The present damage identification approach performs well in both damage localization and extent assessment for 2D/3D frame structures with incomplete frequency response data.

5. The AM method could effectively tackle the nonlinear optimization problem.

6. The sparse regularization obviously improves the accuracy and robustness of the damage identification results.

7. The advantage of being efficient for the proposed min-CRE approach is strongly substantiated by the damage identification results obtained by three identification approaches, namely the min-CRE approach with sparse regularization, the sensitivity approach with Tikhonov regularization and the sensitivity approach with sparse regularization.

8. The sparse regularization along with the CRE objective function is shown to be more accurate than the Tikhonov regularization along with the sensitivity identification approach.

9. The proposed threshold setting method could be used to determine the sparse regularization parameter automatically and efficiently and the threshold parameters are reasonably fixed at $l_{max} = 5$ and $\alpha = 4$.

10. The proposed approach is found to be much more efficient and less sensitive to the mass modelling errors than the sensitivity-based approaches (with the Tikhonov regularization or with the sparse regularization).

5

Damage identification using spectrum data

To our best knowledge, the min-CRE approach has not yet been applied to spectrum-driven problems and for most of the previous work, certain loads are required in order to compare the test data of real structures and that of the numerical model. Therefore, this would be impractical for large-scale engineering structures. In this chapter, a novel spectrum-driven damage identification strategy based on the min-CRE approach is introduced.

5.1 Problem statement

5.1.1 Pseudo excitation method (PEM) for forward problem

Under the action of stationary random excitations such as earthquake ground motions and random wind loads, the power spectral density matrix of structural responses is easily obtained. Accordingly, the PEM, which could reduce the structural stationary random response analysis into the structural harmonic response analysis by using the power spectral density data, has been proved computationally convenient and efficient [70, 71].

Consider a general finite element model of a linear elastic time-invariant structure, whose equation of motion can be written as

$$\boldsymbol{M}\ddot{\boldsymbol{u}} + \boldsymbol{C}\dot{\boldsymbol{u}} + \boldsymbol{K}\boldsymbol{u} = \boldsymbol{f}(t), \tag{5.1}$$

where $\boldsymbol{M}$, $\boldsymbol{K}$ and $\boldsymbol{C}$ are the system mass, stiffness and damping matrices, respectively. $\boldsymbol{C}$ is assumed to be a Rayleigh damping herein and $\boldsymbol{C} = a_1\boldsymbol{M} + a_2\boldsymbol{K}$ (a_1 and a_2 are two constants determined by two modal frequencies). $\boldsymbol{f}(t)$ is a stationary random process whose power spectrum density $S_0(\omega)$ has been specified. To solve this problem, let $\boldsymbol{f}(t) = \boldsymbol{a}\sqrt{S_0(\omega)}e^{i\omega t}$ ($\boldsymbol{a}$ is a given constant vector, ω is the circular frequency and $i = \sqrt{-1}$), then the above equation of motion is reduced into the following harmonic equation according to the PEM:

$$\boldsymbol{M}\ddot{\boldsymbol{u}} + \boldsymbol{C}\dot{\boldsymbol{u}} + \boldsymbol{K}\boldsymbol{u} = \boldsymbol{a}\sqrt{S_0(\omega)}e^{i\omega t} \tag{5.2}$$

and its stationary solution would be

$$\boldsymbol{u}_{\mathrm{E}} = \boldsymbol{H}\boldsymbol{a}\sqrt{S_0(\omega)}e^{i\omega t}, \tag{5.3}$$

where $\boldsymbol{u}_{\mathrm{E}}$ is called the excitation spectrum-based(ExS-based) solution in this research and $\boldsymbol{H}$ is the frequency response function.

Assuming that the power spectrum density of the kth structural response S^k_{uu} is known, where $\{k \in \wp\}$ is the set of points measured by incomplete finite sensors, the harmonic response $\boldsymbol{u}^k$ of the corresponding points based on these structural response spectrum can be written as

$$\boldsymbol{u}^k_{\mathrm{R}} = (\boldsymbol{c} + \boldsymbol{d}i)^k\sqrt{S^k_{uu}(\omega)}e^{i\omega t} \tag{5.4}$$

where $(c^k)^2 + (d^k)^2 = 1$ and the ratio c^k/d^k is equal to the ratio of the real part to imagery part of $(\boldsymbol{H}\boldsymbol{a})^k$. It is easily proved that $\boldsymbol{u}^k_{\mathrm{E}} = \boldsymbol{u}^k_{\mathrm{R}}$ for $k \in \wp$. Unlike the ExS-based solution $\boldsymbol{u}_{\mathrm{E}}$ in **Eq.** (5.3), which is obtained by the excitation spectrum through the forward process, the response spectrum-based (ReS-based) solution $\boldsymbol{u}_{\mathrm{R}} = (\boldsymbol{c}+\boldsymbol{d}i)^k\sqrt{S_{uu}(\omega)}e^{i\omega t}$ can be directly transformed from the structural response spectrum without the knowledge of structure damage's information. Due to this fact, it serves as the measured displacement in the following inverse solving process.

5.1.2 CRE function

To define the constitutive relation error(CRE), consider an admissible pair $(\tilde{\boldsymbol{u}}, \tilde{\boldsymbol{\sigma}})$ which satisfies the kinematic constrains ($\tilde{\boldsymbol{u}} \in \mathcal{U}$) and the equilibrium equations ($\tilde{\boldsymbol{\sigma}} \in \Im$), respectively, in the frequency domain. It is easily known that, if the constitutive relations are additionally satisfied with an admissible elastic modulus matrix $\boldsymbol{D}(\boldsymbol{\theta})(\boldsymbol{D} \in \mathcal{C})$, where $\boldsymbol{\theta}$ denotes the damage parameters with $\theta_i = 1$ meaning no damage of the ith element, the above admissible solution trio $(\tilde{\boldsymbol{u}}, \tilde{\boldsymbol{\sigma}}, \boldsymbol{D})$ would be the exact solution $(\tilde{\boldsymbol{u}}_{\text{ex}}, \tilde{\boldsymbol{\sigma}}_{\text{ex}}, \boldsymbol{D}_{\text{ex}})$. As a result, the CRE for a given frequency is established as

$$
\begin{aligned}
e_{\text{CRE}}(\tilde{\boldsymbol{u}}, \tilde{\boldsymbol{\sigma}}, \boldsymbol{\theta}) &= \frac{1}{2}\int_{\Omega} \left(\boldsymbol{D}(\boldsymbol{\theta})\boldsymbol{B}\tilde{\boldsymbol{u}} - \tilde{\boldsymbol{\sigma}}\right)^T \boldsymbol{D}(\boldsymbol{\theta})^{-1} \left(\boldsymbol{D}(\boldsymbol{\theta})\boldsymbol{B}\tilde{\boldsymbol{u}} - \tilde{\boldsymbol{\sigma}}\right) d\Omega \\
&= \frac{1}{2}\int_{\Omega} \|\boldsymbol{D}(\boldsymbol{\theta})^{-\frac{1}{2}} \left(\boldsymbol{D}(\boldsymbol{\theta})\boldsymbol{B}\tilde{\boldsymbol{u}} - \tilde{\boldsymbol{\sigma}}\right)\|^2 d\Omega,
\end{aligned}
\tag{5.5}
$$

where $\boldsymbol{B}$ is the strain-displacement matrix and Ω defines the physical domain of the structure. The elastic modulus matrix $\boldsymbol{D}(\boldsymbol{\theta})$ denotes the following diagonalization of the damage parameters $\boldsymbol{\theta} = [\theta_1; \cdots; \theta_m]$,

$$
\boldsymbol{D}(\boldsymbol{\theta}) = \begin{pmatrix} \theta_1\boldsymbol{D}_1 & \mathbf{0} & \cdots & \mathbf{0} \\ \mathbf{0} & \theta_2\boldsymbol{D}_2 & \cdots & \mathbf{0} \\ \vdots & \vdots & \ddots & \vdots \\ \mathbf{0} & \mathbf{0} & \cdots & \theta_m\boldsymbol{D}_m \end{pmatrix}, \tag{5.6}
$$

where $\boldsymbol{D}_i$ is transformed by the elasticity tensor C_{pqrs} for element $i, i = 1, \cdots, m$. The diagonal matrix $\boldsymbol{D}(\boldsymbol{\theta})$ is of size $r = \sum_{i=1}^m r_i, r_i = \text{rank}(\boldsymbol{D}_i)$.

For the structure which is of interest in a frequency range $[\omega_{\min}, \omega_{\max}]$, the frequency weighting factor $z(\omega)$ is introduced as

$$
\int_{\omega_{\min}}^{\omega_{\max}} z(\omega)d\omega = 1, z(\omega) \geq 0. \tag{5.7}
$$

$z(\omega)$ is taken equally herein. Then the total CRE in the given frequency range is

$$
F(\tilde{\boldsymbol{u}}, \tilde{\boldsymbol{\sigma}}, \boldsymbol{\theta}) := \int_{\omega_{\min}}^{\omega_{\max}} e_{CRE}(\tilde{\boldsymbol{u}}, \tilde{\boldsymbol{\sigma}}, \boldsymbol{\theta}) z(\omega) d\omega \tag{5.8}
$$

Based on the equations above, the damage identification problem can be solved by the following program (P_0)

$$
(\text{P}_0) \quad \begin{aligned} &(\tilde{\boldsymbol{u}}, \tilde{\boldsymbol{\sigma}}, \boldsymbol{\theta}) = \arg\min F(\tilde{\boldsymbol{u}}, \tilde{\boldsymbol{\sigma}}, \boldsymbol{\theta}) \\ &\text{subject to } \tilde{\boldsymbol{u}} \in \mathcal{U}, \tilde{\boldsymbol{\sigma}} \in \Im, \boldsymbol{D}(\boldsymbol{\theta}) \in \mathcal{C}, \tilde{\boldsymbol{u}} = \tilde{\boldsymbol{u}}_{\text{R}}^k, k \in \wp, \end{aligned} \tag{5.9}
$$

where $\tilde{\boldsymbol{u}}_{\text{R}}^k$ is the Fourier transform of $\boldsymbol{u}_{\text{R}}^k$ defined in equation (5.4) and $(\tilde{\boldsymbol{u}}, \tilde{\boldsymbol{\sigma}})$ is caused by the pseudo harmonic excitation $\boldsymbol{f}(t) = \boldsymbol{a}\sqrt{S_0(\omega)}e^{i\omega t}$.

5.2 Damage identification by min-CRE and sparse regularization

5.2.1 Stress field building strategy

Consider an admissible stress field $\tilde{\boldsymbol{\sigma}}$ which satisfies the equilibrium equation in the frequency domain as follows:

$$\begin{aligned} \boldsymbol{K}\tilde{\boldsymbol{u}} &= \omega^2 \boldsymbol{M}\tilde{\boldsymbol{u}} - i\omega \boldsymbol{C}\tilde{\boldsymbol{u}} + \tilde{\boldsymbol{f}} = \boldsymbol{B}^T\tilde{\boldsymbol{\sigma}} \\ \Rightarrow \boldsymbol{B}^T\tilde{\boldsymbol{\sigma}} &= (1 + i\omega a_2)^{-1}\left[(\omega^2 - i\omega a_1)\boldsymbol{M}\tilde{\boldsymbol{u}} + \tilde{\boldsymbol{f}}\right]. \end{aligned} \tag{5.10}$$

To obtain the stress field $\tilde{\boldsymbol{\sigma}}$, the following remark is necessarily invoked.

Remark. *For $\boldsymbol{A} \in \mathbb{R}^{n\times r}$ and rank$(\boldsymbol{A}) = n$ ($\boldsymbol{A}$ is of full-row rank), consider a system of linear equations*

$$\boldsymbol{A}\boldsymbol{x} = \boldsymbol{b} \tag{5.11}$$

If $n = r$, equation (5.11) admits a unique solution $\boldsymbol{x} = \boldsymbol{A}^{-1}\boldsymbol{b}$. In general, for $n < r$, a vector $\boldsymbol{x}$ that solves the system may not be unique. A computationally simple and accurate way to solve this equation is by using the SVD. That is, if $\boldsymbol{A} = \boldsymbol{U}\boldsymbol{\Sigma}\boldsymbol{V}^*$ is the SVD of $\boldsymbol{A}$, where $\boldsymbol{U}$ and $\boldsymbol{V}$ are unitary matrices, $\boldsymbol{V}^*$ is the conjugate transpose of $\boldsymbol{V}$ and $\boldsymbol{\Sigma}$ is a diagonal matrix with non-negative real numbers on the diagonal, the solutions of equation 5.11 are all given by

$$\boldsymbol{x} = \boldsymbol{A}^+\boldsymbol{b} + \boldsymbol{Z}\boldsymbol{p}, \tag{5.12}$$

where $\boldsymbol{A}^+ = \boldsymbol{V}\boldsymbol{\Sigma}^+\boldsymbol{U}^*$ is the pseudoninverse of matrix $\boldsymbol{A}$, $\boldsymbol{p}$ is an arbitrary column vector of length $r - n$, $\boldsymbol{Z} = \|\boldsymbol{A}^+\|_{\ell_2}\boldsymbol{V}_2$ and $\boldsymbol{V} = \left[(\boldsymbol{V}_1)_{r\times n}, (\boldsymbol{V}_2)_{r\times(r-n)}\right]$. $\|\boldsymbol{A}^+\|_{\ell_2}$, denoting the ℓ_2-norm of the matrix $\boldsymbol{A}^+$, is introduced to reduce the possible ill-conditioning.

Combining of equations (5.10) and (5.12) and setting $\boldsymbol{A} = \boldsymbol{B}^T$, $\boldsymbol{x} = \tilde{\boldsymbol{\sigma}}$ yields

$$\tilde{\boldsymbol{\sigma}} = c_2 c_1 \boldsymbol{A}^+\boldsymbol{M}\tilde{\boldsymbol{u}} + c_2\boldsymbol{A}^+\tilde{\boldsymbol{f}} + \boldsymbol{Z}\boldsymbol{p}, \tag{5.13}$$

where $c_1 = (\omega^2 - i\omega a_1)$ and $c_2 = (1 + i\omega a_2)^{-1}$. It should be noted that only the vector $\boldsymbol{p}$ is unknown in (5.13). As a result, to acquire the stress field $\tilde{\boldsymbol{\sigma}}$ is equal to acquire the vector $\boldsymbol{p}$. The objective function could be reformulated into

$$e_{\mathrm{CRE}}(\tilde{\boldsymbol{u}}, \boldsymbol{p}, \boldsymbol{\theta}) = \frac{1}{2}\int_{\Omega} \|\boldsymbol{D}(\boldsymbol{\theta})^{-\frac{1}{2}} \left(\boldsymbol{D}(\boldsymbol{\theta})\boldsymbol{B}\tilde{\boldsymbol{u}} - \left(c_2 c_1 \boldsymbol{A}^{+}\boldsymbol{M}\tilde{\boldsymbol{u}} + c_2\boldsymbol{A}^{+}\tilde{\boldsymbol{f}} + \boldsymbol{Z}\boldsymbol{p}\right)\right)\|^2 d\Omega. \tag{5.14}$$

5.2.2 Sparse regularization

Usually, the amount of the measured data S_{uu}^{k} is insufficient due to the incomplete finite sensors and limited sample sources. This drives the inverse problem ill-posed and very sensitive to the measurement noise. As mentioned before, the sparse regularization is used herein. By incorporating the sparse regularization into equation (5.5), (P_0) can be replaced by (P_s)

$$(\mathrm{P}_s) \quad \begin{aligned} &(\tilde{\boldsymbol{u}}, \boldsymbol{p}, \boldsymbol{\theta}) = \arg\min F(\tilde{\boldsymbol{u}}, \boldsymbol{p}, \boldsymbol{\theta}) + \lambda\|\boldsymbol{\theta} - \boldsymbol{\theta}_0\|_1^1 \\ &\text{subject to } \tilde{\boldsymbol{u}} \in \mathcal{U}, \tilde{\boldsymbol{\sigma}}(\boldsymbol{p}) \in \Im, \boldsymbol{D}(\boldsymbol{\theta}) \in \mathcal{C}, \tilde{\boldsymbol{u}} = \tilde{\boldsymbol{u}}_{\mathrm{R}}^{k}, k \in \wp, \end{aligned} \tag{5.15}$$

where λ is the non-negative sparse regularization parameter controlling the trade-off between the sparsity and CRE, and $\|\boldsymbol{\theta}-\boldsymbol{\theta}_0\|_1^1 = \sum_{i=1}^{m} |\theta_i - \theta_{0i}|$. According to posteriori research, the 'threshold setting method'(TSM) is used to estimate the optimal regularization parameter where $\lambda_{\mathrm{est}} = \mathrm{TSM}(\boldsymbol{\Lambda}, l_{\max}, \alpha)$. For more details, refer to Section 3.2.2.

5.2.3 AM method

With an initial guess of the damage parameters $\boldsymbol{\theta}_0$, the solving process for the program (P_s) is described below.

- step 1 (UMF step): Update the mechanical field $(\tilde{\boldsymbol{u}}, \boldsymbol{p})$ with the given damage parameters $\boldsymbol{\theta}_{(j-1)}$

$$(\tilde{\boldsymbol{u}}_{(j)}, \boldsymbol{p}_{(j)}) = \arg \min_{\boldsymbol{u}\in\mathcal{U}, \boldsymbol{\sigma}(\boldsymbol{p})\in\Im, \boldsymbol{u}=\hat{\boldsymbol{u}}_k, k\in\wp} F(\tilde{\boldsymbol{u}}, \boldsymbol{p}, \boldsymbol{\theta}_{(j-1)}) \tag{5.16}$$

- step 2 (UDP step): Update the damage parameters $\boldsymbol{\theta}$ by the mechanical fields $(\tilde{\boldsymbol{u}}_{(j)}, \boldsymbol{p}_{(j)})$ obtained in step 1.

$$\boldsymbol{\theta}_{(j)} = \arg \min_{\boldsymbol{D}(\boldsymbol{\theta})\in\mathcal{C}} F(\tilde{\boldsymbol{u}}_{(j)}, \boldsymbol{p}_{(j)}, \boldsymbol{\theta}) + \lambda\|\boldsymbol{\theta} - \boldsymbol{\theta}_0\|_1^1 \tag{5.17}$$

UMF step

For the sake of convenience, superscript U and M correspond to the unmeasured and measured parts of the array in follows, respectively. Minimization of the objective function over the mechanical field $(\tilde{\boldsymbol{u}};\boldsymbol{p})$ yields

$$\begin{aligned}
&\begin{pmatrix} \tilde{\boldsymbol{u}}_{(j)} \\ \boldsymbol{p}_{(j)} \end{pmatrix} = \begin{pmatrix} \tilde{\boldsymbol{u}}^k_{R(j)} \\ (\boldsymbol{R}^{UU})^{-1}(\boldsymbol{S}^U - \boldsymbol{R}^{UM}\tilde{\boldsymbol{u}}^k_{R(j)}) \end{pmatrix} \\
&\boldsymbol{R} = (\big(\boldsymbol{D}(\boldsymbol{\theta}_{(j-1)})\boldsymbol{B} - c_2c_1\boldsymbol{A}^+\boldsymbol{M}, -\boldsymbol{Z}\big)^T\boldsymbol{D}(\boldsymbol{\theta}_{(j-1)})^{-1}(\big(\boldsymbol{D}(\boldsymbol{\theta}_{(j-1)})\boldsymbol{B} - c_2c_1\boldsymbol{A}^+\boldsymbol{M}, -\boldsymbol{Z}\big) \\
&\boldsymbol{S} = (\big(\boldsymbol{D}(\boldsymbol{\theta}_{(j-1)})\boldsymbol{B} - c_2c_1\boldsymbol{A}^+\boldsymbol{M}, -\boldsymbol{Z}\big)^T\boldsymbol{D}(\boldsymbol{\theta}_{(j-1)})^{-1}c_2\boldsymbol{A}^+\tilde{\boldsymbol{f}}.
\end{aligned} \tag{5.18}$$

As $\boldsymbol{p}_{(j)}$ is obtained, $\tilde{\boldsymbol{\sigma}}_{(j)}$ could be easily assembled based on equation (5.13).

UDP step

To update the damage parameter $\boldsymbol{\theta}$, the objective function in (P_s) is divided by each element

$$\begin{aligned}
e^i_{\mathrm{CRE}}(\tilde{\boldsymbol{u}}^i_{(j)}, \tilde{\boldsymbol{\sigma}}^i_{(j)}, \theta_i) &= \frac{1}{2}\int_\Omega \|(\theta_i\boldsymbol{D}_i)^{-\frac{1}{2}}\left(\theta_i\boldsymbol{D}_i\boldsymbol{B}_i\tilde{\boldsymbol{u}}^i_{(j)} - \tilde{\boldsymbol{\sigma}}^i_{(j)}\right)\|^2 d\Omega + \lambda|\theta_i - \theta_{0i}| \\
&= \left(a_i\theta_i + \frac{b_i}{\theta_i} + c_i\right) + \lambda|\theta_i - \theta_{0i}|,\ i = 1, \cdots, m \\
a_i &= \frac{1}{2}\int_\Omega \tilde{\boldsymbol{u}}^{iT}_{(j)}\boldsymbol{B}_i^T\boldsymbol{D}_i\boldsymbol{B}_i\tilde{\boldsymbol{u}}^i_{(j)}d\Omega, \\
b_i &= \frac{1}{2}\int_\Omega \tilde{\boldsymbol{\sigma}}^{iT}_{(j)}\boldsymbol{D}_i^{-1}\tilde{\boldsymbol{\sigma}}^i_{(j)}d\Omega, \\
&c_i : \text{constant term.}
\end{aligned} \tag{5.19}$$

Minimization of the objective function over every single-variable θ_i in each element results in

$$\begin{aligned}
\theta_{i(j)} &= \arg\min\left(a_i\theta_i + \frac{b_i}{\theta_i} + c_i\right) + \lambda|\theta_i - \theta_{0i}| \\
&= \begin{cases} \sqrt{\dfrac{b_i}{a_i + 2\lambda}}\ , \text{if } \lambda < \dfrac{1}{2}\left(\dfrac{b_i}{\theta_{0i}^2} - a_i\right) \\ \sqrt{\dfrac{b_i}{a_i - 2\lambda}}\ , \text{else if } \lambda < \dfrac{1}{2}\left(a_i - \dfrac{b_i}{\theta_{0i}^2}\right) \\ \theta_{0i}\ , \text{else } \lambda \geq \dfrac{1}{2}\left|a_i - \dfrac{b_i}{\theta_{0i}^2}\right| \end{cases},\ i = 1, \cdots, m.
\end{aligned} \tag{5.20}$$

5.2.4 Summary of the proposed damage identification approach

By combining the UMF step and the UDP step in Section 5.2.3 and using the threshold setting method so as to estimate the optimal regularization parameter λ, the damage identification algorithm by min-CRE and sparse regularization based on power spectrum density data can be established as shown in **Table 5.1**.

5.3 Numerical verification

5.3.1 Shear building structure

A 12-story shear building structure as shown in **Figure 5.1** is used to test the proposed damage identification approach first (see reference [73] for details of the structure). The mass and stiffness parameters of the intact system are $m_1 = m_2 = \cdots = m_{12} = 1.0 \times 10^5$kg, $k_1 = k_2 = \cdots = k_{12} = 2.0 \times 10^8$N/m. The Rayleigh damping model is adopted with the damping ratios taken equal to 5% for the first and second modes and the Rayleigh coefficients a_1 and a_2 are 0.506 and 1.073×10^{-4}, respectively. Two damage cases are considered: Single damage (D1), the stiffness of the 6th story is reduced by 20% (stiffness reduction=0.2); Multiple damages (D2), the stiffnesses of 2nd story and 4th story are reduced by 5% and 15% (stiffness reduction=0.05, 0.15), respectively. The natural frequencies before and after damage are shown in **Table 5.2**.

Assume that the structure is subjected to a stationary acceleration excitation of white noise from the ground. The measured accelerations of the 1st and 2nd stories are taken from the results of numerical simulation during the time period $[0, 60s]$ with a sampling rate of 500Hz and polluted by a standard normally distributed random noise of 10% level (**Figure 5.2**). **Figure 5.3** shows the comparison of the power spectrum density between the initial (undamaged) model and the damaged model at the 2nd story for D1.

To investigate the correspondence between the ReS-based solution $\boldsymbol{u}_{\mathrm{R}}$ and the Exs-based solution $\boldsymbol{u}_{\mathrm{E}}$ in section 5.1.1, the frequency response $\tilde{\boldsymbol{u}}_2$ of the 2nd story for the undamaged model is shown in **Figure 5.4**. One can find that two curves match each other well. This verifies the effectiveness of using the ReS-based solution to simulate the ExS-based solution during the damage identification process.

Table 5.1 Summery of the proposed AM method

Initial algorithm setting
-set inital damage parameters $\boldsymbol{\theta}_{(0)} = \boldsymbol{\theta}_0$ as those of the intact structure -set values of the maximum threshold setting rank l_{max} and the discriminating ratio α for the threshold setting method [72] -define the convergence tolerance TOL and the maximum number of iterations Z_{max} -load the measured response power spectrum density data $\boldsymbol{S}_{uu}^k$ as well as the excitation power spectrum density data $S_0(\omega)$ -construct the pseudo harmonic excitation $\boldsymbol{f}(t) = \boldsymbol{a}\sqrt{S_0(\omega)}e^{i\omega t}$(section 5.1.1) -assemble the strain-displacement matrix $\boldsymbol{B}$ and refer to **Remark** 5.2.1 to get the matrices $\boldsymbol{A}$,$\boldsymbol{Z}$
Alternating minimization approach (for $j = 1 : Z_{max}$)
-assemble the mass, stiffness and frequency response matrices $\boldsymbol{M}, \boldsymbol{K}$ and $\boldsymbol{H}$ using current value of $\boldsymbol{\theta}_{(j-1)}$ -obtain the pseudo harmonic response $\boldsymbol{u}_{\mathrm{R}(j-1)}^k = (\boldsymbol{c} + \boldsymbol{d}i)^k\sqrt{S_{uu}^k(\omega)}e^{i\omega t}$ (section 5.1.1) -refer to the UMF step to obtain the updating mechanical field (section 5.2.3, Appendix 5.2.3) $\begin{pmatrix} \tilde{\boldsymbol{u}}_{(j)} \\ \boldsymbol{p}_{(j)} \end{pmatrix} = \begin{pmatrix} \tilde{\boldsymbol{u}}_{R(j)}^k \\ (\boldsymbol{R}^{UU})^{-1}(\boldsymbol{S}^U - \boldsymbol{R}^{UM}\tilde{\boldsymbol{u}}_{R(j)}^k) \end{pmatrix}$ -choose the optimal regularization parameter λ according to the treshold setting method [72] -refer to the UDP step to obtain the updating damage parameter $\theta_{i(j)}$, $i = 1, \cdots, m$ (section 5.2.3, Appendix 5.2.3): • if $\lambda < \frac{1}{2}\left(\frac{b_i}{\theta_{0i}^2} - a_i\right)$, then $\theta_{i(j)} = \sqrt{\frac{b_i}{a_i+2\lambda}}$, • else if $\lambda < \frac{1}{2}\left(a_i - \frac{b_i}{\theta_{0i}^2}\right)$, then $\theta_{i(j)} = \sqrt{\frac{b_i}{a_i-2\lambda}}$, • else $\theta_{i(j)} = \theta_{i0} = 1$ -Convergence criterion • if $\parallel \tilde{\boldsymbol{\theta}}_{(j)} - \tilde{\boldsymbol{\theta}}_{(j-1)} \parallel / \parallel \tilde{\boldsymbol{\theta}}_{(0)} \parallel \leq$ TOL break

Table 5.2 Frequencies of the shear building structure in undamaged and damaged states

Mode	undamaged freq. (Hz)	D1 freq. (Hz)	D2 freq. (Hz)
1	0.89	0.88	0.88
2	2.67	2.66	2.66
3	4.40	4.32	4.37

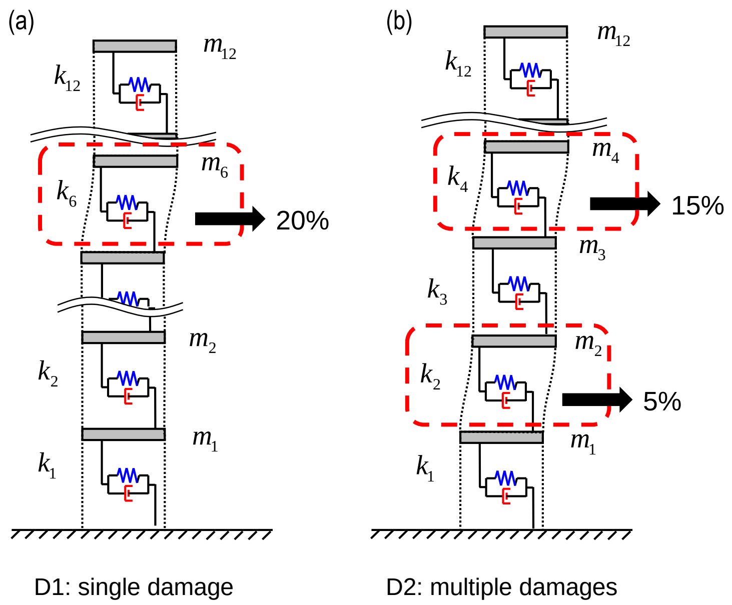

Figure 5.1 Overview of the numerical model

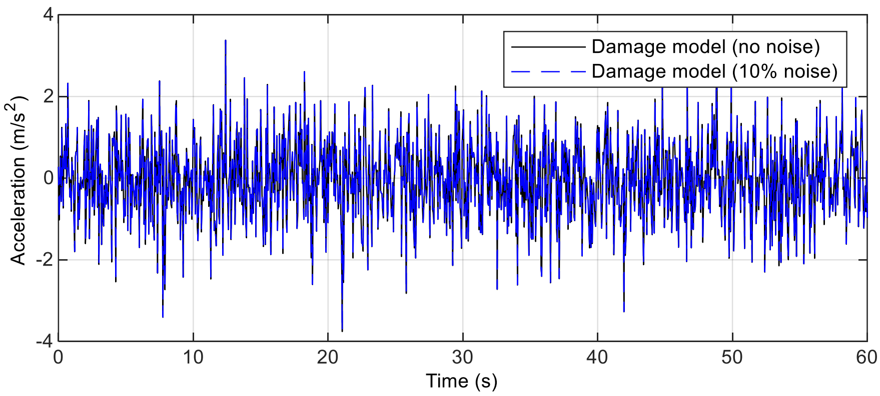

Figure 5.2 Response at 2nd floor for D1

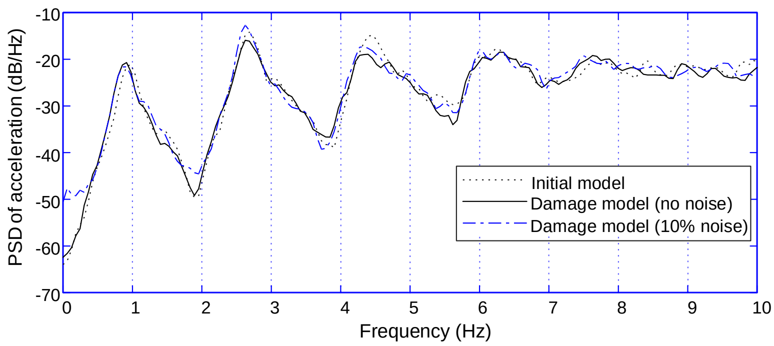

Figure 5.3 Power spectrum density of acceleration at 2nd floor for D1

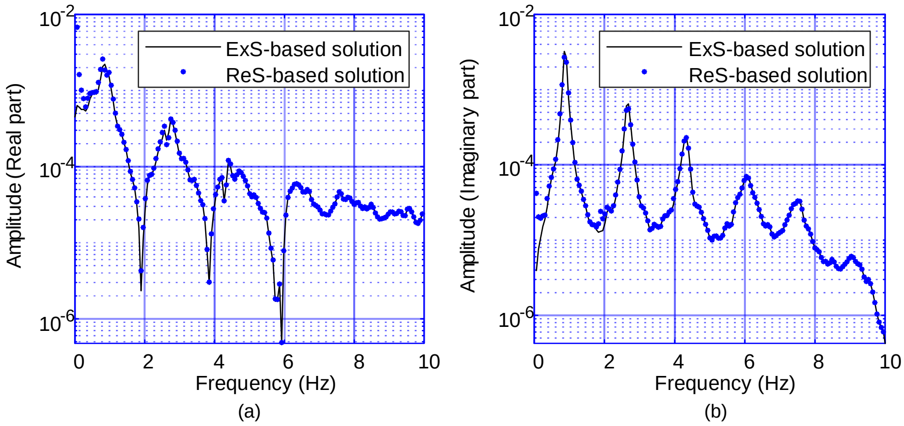

Figure 5.4 Frequency response comparison between ReS-based solution and Exs-based solution: (a)real part, (b)imaginary part

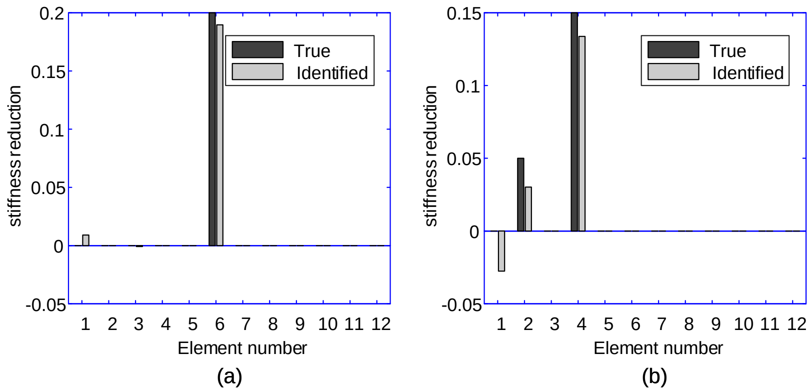

Figure 5.5 Identification results with 10% noise: (a)D1, (b)D2

Identification results for respective damage scenarios are summarized in **Figure 5.5**. As can be seen, damage is identified successfully for the single damage case D1 with an optimal value of regularization parameter $\lambda = 1.211 \times 10^{-11}$. Regarding the case D2, the multiple damages case seems to be more sensitive to the noise: some unwanted yet acceptable stiffness change at the 1st story was also observed. This phenomenon is due to the different effectiveness of the sparse regularization [72]. Sparsity obviously has a pronounced effect on less number of damages while multiple damages reduce sparsity in intensity. The optimal sparse regularization parameter is found to be 1.018×10^{11} for D2.

5.4 Experimental verification

In this section, the experimental verification of using the proposed min-CRE approach for damage identification will be further presented for a laboratory plane frame structure. The experimental set up, the data generation, the numerical model and the damage identification results will be presented in details in the following.

5.4.1 Experimental set-up and data generation

Two two-story testing plane frames, undamaged frame (UF) and damaged frame (DF), are fabricated in the structure laboratory in Kyoto University, as shown in **Figure 5.6**(a). Parameters of these frames are: height of the first story $H_1 = 0.225$m, height of the second story $H_2 = 0.25$m, width $B = 0.2$m, rectangular cross-section of the first story's beam/column $b_1 \times h_1 = 40\text{mm} \times 1\text{mm}$, rectangular cross-section of the second story's beam/column $b_2 \times h_2 = 30\text{mm} \times 1\text{mm}$, lumped mass pair of the first story $m_1 = 1.16\text{kg}$, lumped mass pair of the second story $m_2 = 1.09\text{kg}$. Young's modulus, Poisson's ratio and mass density of the beam/column are estimated as $E = 200\text{Gpa}$, $\nu = 0.3$ and $\rho = 7.7 \times 10^3\text{kg/m}^3$. The size of the lumped mass is measured as $50\text{mm} \times 50\text{mm} \times 50\text{mm}$. Lumped mass and beam/column are connected by L-angles with size $40\text{mm} \times 20\text{mm} \times 2\text{mm}$.

In DF, damages are introduced by reducing the rectangular cross section in the area of left 1/2 length of the beam in the first story, from $b_1 \times h_1 = 40\text{mm} \times 1\text{mm}$ to $b_d \times h_1 = 20\text{mm} \times 1\text{mm}$, as illustrated in **Figure 5.6**(b). As a result, the approximated Damage Index (k^{damage}/k_0) for this area is estimated as 0.5. For the sake of clarity, it should be noted that in this example, since the mass matrix of the structure is mainly determined by the lumped mass instead of the beam, only the change of stiffness is identified while the change of mass is ignored.

The frame is bolted on the shaking table and tested using ground excitation (**Figure 5.6**(d)). The sampling frequency is set to 200Hz and nine accelerometers(A0-A8) are installed for this test (**Figure 5.6**(a),**Figure 5.7**). Each accelermometer is weighted about 0.02kg$\sim$ 0.03kg. The horizontal acceleration responses are measured during the time period [0,30]s.

5.4.2 Numerical baseline model

An initial finite element (FE) model is established according to the geometric and physical properties of the experimental UF model, with 42 planar elements and 42 nodes as shown in **Figure 5.7**. Each node has three DOFs (two transnational displacements and one rotational displacement) and the system has 126 DOFs in total. The weights of lumped masses are added to the corresponding nodes and adjacent beam elements are set as rigid link in the FE model.

The UF was tested first using white noise ground excitation. Experimental modal analysis is then performed so as to extract the natural frequencies and mode shapes of the frame from the measured acceleration responses by the subspace method. The obtained modal data are used to perform the initial model updating to minimize the difference between the UF model and the FE model by the sensitivity-based method. This procedure was described in detail in reference [65]. **Figure 5.8** and **Figure 5.9**

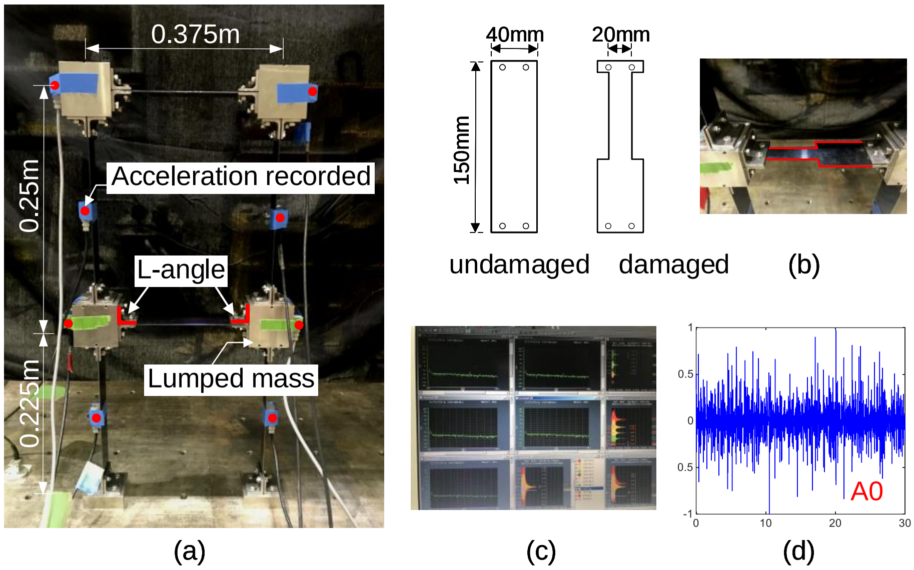

Figure 5.6 Overview of the test model: (a) test frame (UF/DF), (b) undamaged and damaged beam, (c) data acquisition, (d) acceleration of the ground excitation: white noise

show that the natural frequencies and mode shapes predicted by the updated FE model (the baseline model) match the experimental test results fairly well. It should be pointed out that the 4th mode was not identified through the experiment data and comparisons of this mode could not be conducted consequently.

A further validation of the updated model was preformed by comparing the experimental accelerations and those obtained by the updated FE model (**Figure 5.10**). As the FE model is only identified based on the experimental modal data, the identified damping parameters using the Rayleigh damping assumption are used in this comparison. The Rayleigh coefficients a_1 and a_2 are 0.7102 and 6.9325×10^{-5}, respectively. So far, the accuracy of the FE modal was strongly verified. This updated FE model is then used as **the baseline model** in the following damage identification process.

5.4.3 Damage identification

In the next identification step, the experimental DF structure is also subjected to the white noise excitation from the ground. Accelerations are obtained and then transformed into power spectrum densities using the Welch's method. To improve the robustness and accuracy of the identification approach, data pre-selection is conducted [74]. As can be seen from **Figure 5.8**, obvious changes of natural frequencies could

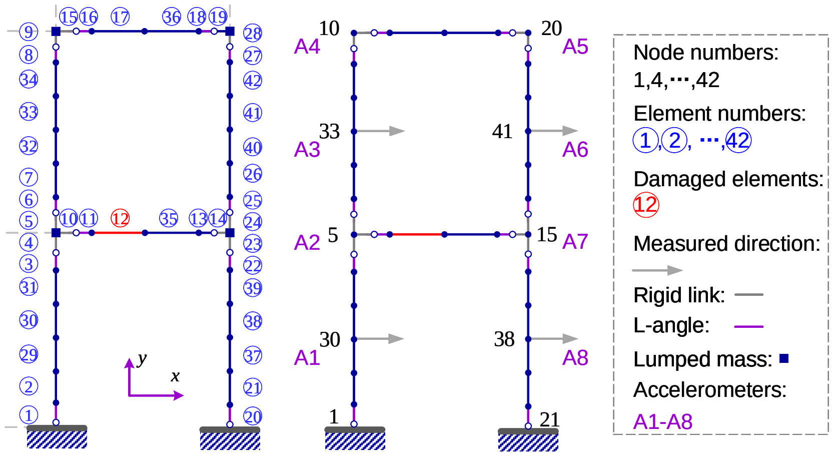

Figure 5.7 FE Model of plane frame structure

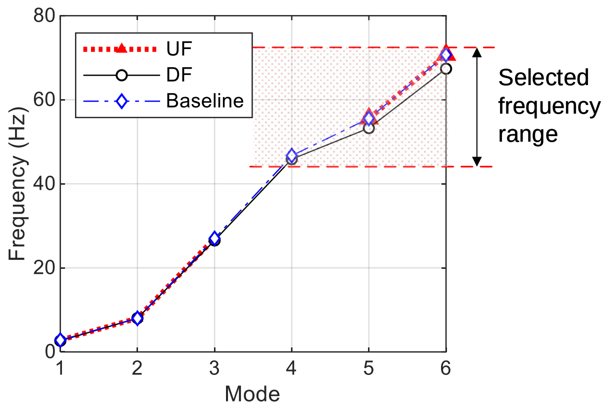

Figure 5.8 Natural frequencies of the experimental UF model, the experimental DF model and the baseline model

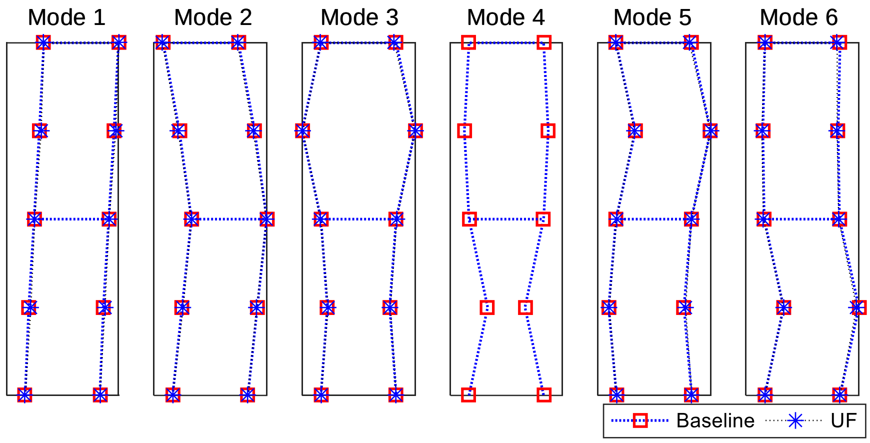

Figure 5.9 Mode shapes of the experimental UF model and the baseline model

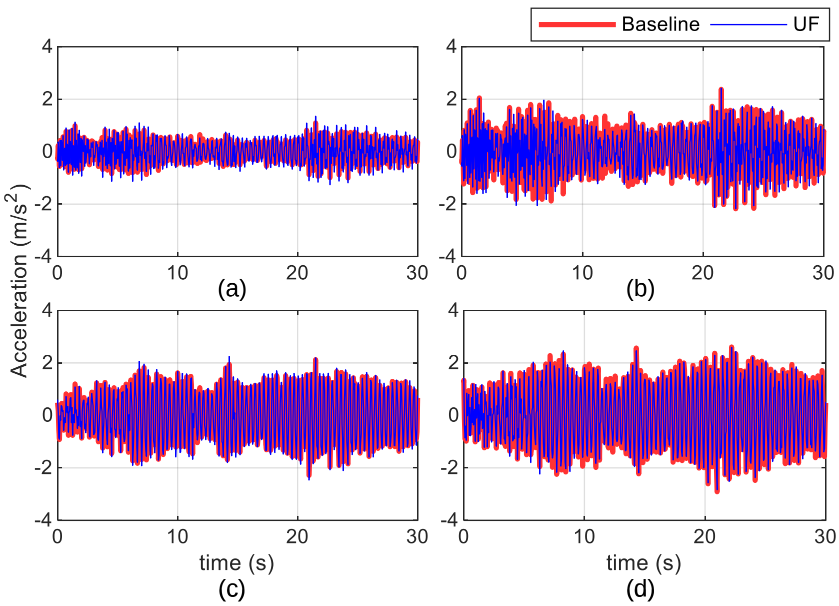

Figure 5.10 Accelerations of the experimental UF model and the baseline model at: (a)A1, (b)A2, (c)A3 and (d)A4

only be found in higher modes while the changes in lower natural frequencies are small (modes 1-3). This indicates that the responses of the structure in higher frequency range are more sensitive to this kind of damage pattern. As a result, the selected frequency range for the response power spectrum density data is set to [45,72]Hz herein.

Using the measured data from the accelerometers installed at all positions is not necessary for the proposed identification approach. As the frequency range [45,72]Hz is chosen, only accelerometers A1, A3, A6 and A8 are used for damage identification. The reason behind this choice is that the dynamic response of accelerometers A2, A4, A5 and A7 is considered to be equal to zero for this selected high frequency range, which could be directly seen from **Figure 5.12** and also be inferred from the 4-6 mode shapes in **Figure 5.9**. To investigate the data from which accelerometers are more efficient for identification, the accelerometers are divided into two groups: (1) G1: A1&A8 and (2) G2: A3&A6.

Identification results are shown in **Figure 5.11**. As could be seen, the proposed approach with sparse regularization could identify the damage location (Element 12) clearly. Compared to G1, G2 results in more satisfactory damage extent assessment. The optimal regularization parameters are $\lambda = 3.074 \times 10^{-12}$ for G1 and $\lambda = 1.980 \times 10^{-12}$ for G2. **Figure 5.11**(c) is concerned with the identified results without any sparse regularization for G1. As is observed, neither damage location nor damage extent could be appropriately identified in such situation. Sparse regularization has demonstrated a pronounced effect on the accuracy and robustness for the identification process. To testify the convergence of the proposed approach, the number of iterations is illustrated in **Figure 5.11**(d). One can find that damage is clearly identified after 100 steps. This result verifies the convergence of the presented method.

Although the proposed identification approach is a procedure of updating damage parameter of the identified model to best fit the constitutive relation, rather than the dynamic response, of the experimental model, the power spectrum densities of the baseline beam model, identified model and DF model at A1-A4 are depicted in **Figure 5.12**. One can find that the power spectrum density of the identified model corresponds with the DF model well. This case shows that the proposed approach is as effective to identify the damage parameters as those methods which measure the response discrepancies between the numerical model and the dynamic test results.

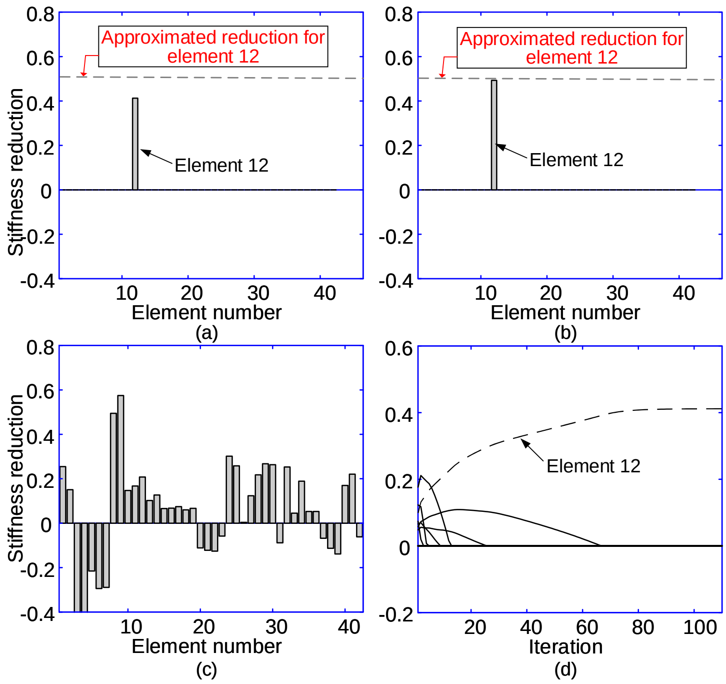

Figure 5.11 Identified results: (a) G1 (b) G2 (c) G1 without sparsity (d) stiffness reduction vs iteration in case G1

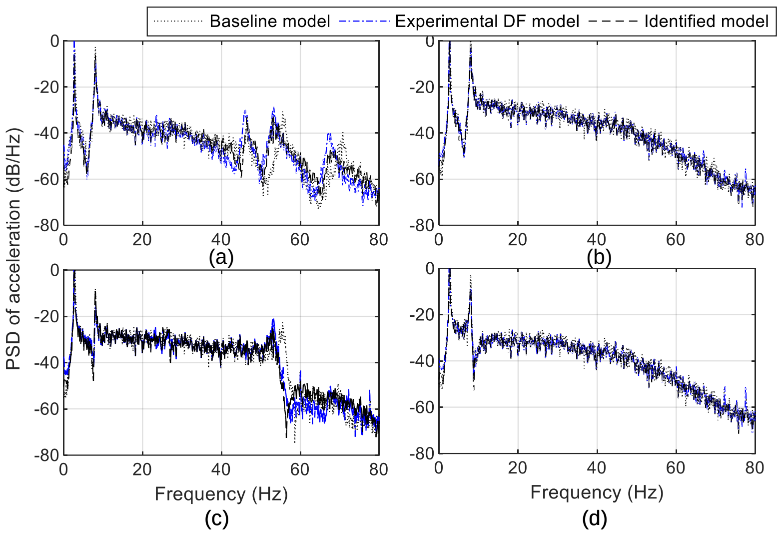

Figure 5.12 Power spectrum density of acceleration at: (a)A1, (b)A2, (c)A3 and (d)A4

5.5 Conclusions

Usage of the error in constitutive relation for damage identification has gained increasing attention from many engineers recently. An effective and simple solution procedure so as to use the CRE as the objective function is crucial to the development of this technique. A spectrum-driven damage identification strategy based on the min-CRE approach was proposed in this chapter. The sparse regularization has been enforced to enhance the robustness of this approach with introducing little additionally computational effort due to the favourable mathematical features of the CRE objective function. The AM method was used to get the solution to this nonlinear optimization problem. Results show that:

1. The stationary random vibration problem could be transformed into a series of harmonic vibrations by the pseduo excitation method and the error in constitutive relation is established by the admissible stress field and admissible displacement field.

2. The response spectrum based solution (ReS-based) and the excitation spectrum-based solution (ExS-based) are introduced so as to be used into the CRE objective function.

3. Building of the admissible stress field is addressed in a much simpler way by using singular value decomposition than previous chapters.

4. The sparse regularization is found to be effective to circumvent the ill-posedness of the inverse problem.

5. The proposed method has the advantage that only measurement power spectrum density data from few limited sensors are needed for the inverse problem.

6. The proposed method is insensitive to measurement noise (up to 10%) and effective for both small and large damage identifications according to the numerical example of the shear building structure.

7. Effectiveness and accuracy of the synthesis of the min-CRE approach and sparse regularization using spectrum data are also verified by the experimental test of a laboratory plane frame structure subjected to white noise ground motion.

8. Structures with damages occurring at less locations are recommended for the proposed approach.

6

Conclusions

6.1 Conclusions

The research work presented in this thesis was focused on the development of an advanced model-based computational procedure for damage identification. This identifying procedure is based on minimum constitutive relation error (min-CRE) and sparse regularization. The interest in applying the proposed approach in this research to large-scale architectural and civil structures was the essential motivation of this research. Several main conclusions drawn will be listed in the following.

Minimum constitutive relation error: A separately convex objective function to measure the residual of the constitutive equations connecting between the admissible stress field and the admissible displacement field has been established for damage identification. This function has a strong physical meaning and is quite general. The mathematical advantages of this objective function has be clarified. The alternating minimization (AM) method was then applied to practically get the solution for this nonlinear optimization problem. The attractive features of using min-CRE as objective function are: 1. no sensitivity analysis is involved and thus high computational cost could be avoided; 2. as the objective function is separately convex, large damages may become identifiable.

Measured data: In this research, the the min-CRE principle has been successfully applied to probably the most widely used measured data: static, modal, FRF and spectrum data. Different types of exciatations correspond to different types of measured data. Multiple loads and associated sets of measurements are suggested to be conducted for static test. Compared to the number of measured sensors used during the modal test, only few limited sensors are needed if the FRF or spectrum data are appropriately obtained. Particular attention should be paid to properly select the frequency ranges of the FRF and spectrum data.

Sparse regularization: Empirical parameter identification from a finite measurement data set is always an underdetermined problem, sparse regularization is applied to the original CRE objective function in this research so as to solve such problem. Physical interpretation of sparse and Tikhonov regularizations has been clarified and sparse regularization is found to be much more efficient, more accurate and less sensitive to the modeling errors than the Tikhonov regularization. The main prerequisite for sparse regularization is that the damage only occurs at limited/sparse members for the structures and no other information is required. A novel threshold setting method is proposed to determine the sparse regularization parameter with closed-form solutions automatically and efficiently.

Identification results: The proposed min-CRE principle and the corresponding sparse regularized damage identification approach have been successfully applied to beam structures using few measurements with noise included. The same phenomenon was also shown to occur with 2D/3D framed structures. It was analytically and experimentally shown that the proposed approach can give good identification results of the damage location and severity and is effective for both small and large, single and multiple damage identification. Furthermore, the proposed method converges well in practice.

6.2 Suggestions for further work

Physics model: The present approach is based on a clear physical model of the structure. In practice, both Neumann and Dirichlet boundary conditions could be less reliable. Hence, an identification strategy enabling to take into account all the available information and capable to deal with different reliability levels of information should be considered.

Uniqueness aspect: Non-unique parameter estimations seem inevitable in damage identification or model updating problem. More detailed explanation of the identified mathematics behind non-unique damage parameter changes and its relation to regularizations should be further investigated.

Non-linearity: Current min-CRE based techniques only have the ability to identify linear elastic stiffness parameters for an appropriately defined identification model. However these techniques are not sufficient to provide means to update the parameters that govern either nonlinear behavior or deterioration of material properties. Applications of nonlinear damage identification should be further explored. In nonlinear time-dependent problems, three error sources should be distinguished: the space discretization, the time discretization and the iterative technique used to solve the nonlinear discrete problem. For that reason, several error estimators could be deduced based on the constitutive law residuals so as to take these three sources into account.

Strength vs. Stiffness: Existing damage diagnosis techniques are primarily limited to stiffness reduction identification of the structure. In some instances there is a significant difference between strength and stiffness. For example, one major failure mechanism of concrete highway bridge is by the corrosion of the steal reinforcement cables running in channels in the concrete. Once the cables in the concrete has no strength in tension and so the bridge is liable to collapse. Unfortunately, the stiffness of the bridge do not change because the stiffness of the bridge is mainly due to the concrete. Such critical issue challenges most of the identification techniques.

Appendix A

Displacement-based and force-based beam element

For the following 3D beam structure in this Appendix, the displacement and force of the beam is described in an $Oxyz$-local coordinate system and an $\bar{O}\bar{x}\bar{y}\bar{z}$-global coordinate system. For the time being, the position of O and the orientation of the y and z-axes may be chosen freely.

A.1 Displacement-based beam element

The auxiliary local nodal displacements $(u_x^i, u_y^i, u_z^i, \theta_x^i, \theta_y^i, \theta_z^i)$ (3 translations and 3 rotations) at an arbitrary node i are naturally selected to obtain the admissible displacement solution first. Thus, for an arbitrary element e with two nodes i, j, the discretized displacement field $(w_x^e, w_y^e, w_z^e, \theta_x^e)$ as shown in **Figure A.1** constructed by linear Lagrange interpolation for (w_x^e, θ_x^e) and cubic Hermit interpolation for (w_y^e, w_z^e) based on the corresponding local nodal displacements $(u_x^i, u_y^i, u_z^i, \theta_x^i, \theta_y^i, \theta_z^i)$ and $(u_x^j, u_y^j, u_z^j, \theta_x^j, \theta_y^j, \theta_z^j)$, is

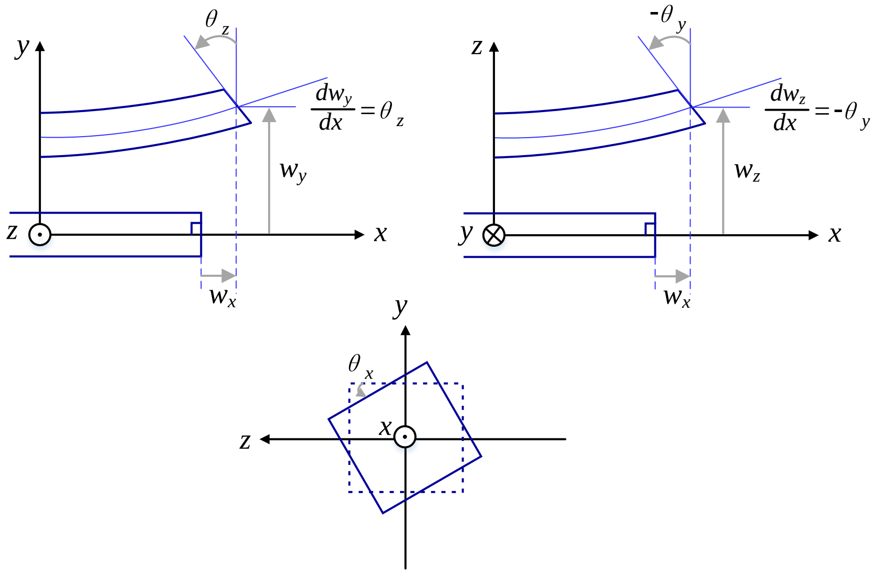

Figure A.1 Basics of a displacement-based finite element e

expressed as

$$
\begin{pmatrix} w_x^e \\ w_y^e \\ w_z^e \\ \theta_x^e \end{pmatrix} = \boldsymbol{\Phi}_u^e \tilde{\boldsymbol{u}}_L^e, \;\; \tilde{\boldsymbol{u}}_L^e := \left[u_x^i, u_y^i, u_z^i, \theta_x^i, \theta_y^i, \theta_z^i, u_x^j, u_y^j, u_z^j, \theta_x^j, \theta_y^j, \theta_z^j\right]^T
$$

$$
\boldsymbol{\Phi}_u^e := \begin{pmatrix} N_1 & 0 & 0 & 0 & 0 & 0 & N_2 & 0 & 0 & 0 & 0 & 0 \\ 0 & H_1 & 0 & 0 & 0 & H_2 & 0 & H_3 & 0 & 0 & 0 & H_4 \\ 0 & 0 & H_1 & 0 & -H_2 & 0 & 0 & 0 & H_3 & 0 & -H_4 & 0 \\ 0 & 0 & 0 & N_1 & 0 & 0 & 0 & 0 & 0 & N_2 & 0 & 0 \end{pmatrix} \tag{A.1}
$$

where the polynomial interpolation functions $N_1, N_2, H_1, H_2, H_3, H_4$ are of the following forms,

$$
\begin{aligned}
&N_1(\xi) = \frac{1-\xi}{2}, N_2(\xi) = \frac{1+\xi}{2} \\
&\begin{cases} H_1(\xi) = \frac{1}{2}(\xi+2)(\xi-1)^2, H_2(\xi) = \frac{1}{4}(\xi+1)(\xi-1)^2\frac{h^e}{2}, \\ H_3(\xi) = \frac{1}{2}(2-\xi)(\xi+1)^2, H_4(\xi) = \frac{1}{4}(\xi-1)(\xi+1)^2\frac{h^e}{2}, \end{cases} \\
&\xi = \frac{2s^e}{h^e} - 1, h^e = \sqrt{(x_j-x_i)^2 + (y_j-y_i)^2 + (z_j-z_i)^2}, \\
&s^e = \sqrt{(x-x_i)^2 + (y-y_i)^2 + (z-z_i)^2}.
\end{aligned} \tag{A.2}
$$

In order to perform the further assembling computation, the local nodal displacements $\tilde{\boldsymbol{u}}_L^e$ need to be expressed in a common coordinate system or the global coordinate system. To this end, the relationship between local nodal displacements $\tilde{\boldsymbol{u}}_L^e$ and global nodal displacements $\tilde{\boldsymbol{u}}^e$ in element e is explored, pertaining to

$$\tilde{\boldsymbol{u}}_L^e = \boldsymbol{T}_u^e \tilde{\boldsymbol{u}}^e, \tag{A.3}$$

where $\boldsymbol{T}_u^e$ is the transformation matrix of the following form

$$\boldsymbol{T}_u^e = \begin{pmatrix} \boldsymbol{t} & \boldsymbol{0} & \boldsymbol{0} & \boldsymbol{0} \\ \boldsymbol{0} & \boldsymbol{t} & \boldsymbol{0} & \boldsymbol{0} \\ \boldsymbol{0} & \boldsymbol{0} & \boldsymbol{t} & \boldsymbol{0} \\ \boldsymbol{0} & \boldsymbol{0} & \boldsymbol{0} & \boldsymbol{t} \end{pmatrix} \tag{A.4}$$

$$\boldsymbol{t} = \begin{pmatrix} \cos(x,\bar{x}) & \cos(x,\bar{y}) & \cos(x,\bar{z}) \\ \cos(y,\bar{x}) & \cos(y,\bar{y}) & \cos(y,\bar{z}) \\ \cos(z,\bar{x}) & \cos(z,\bar{y}) & \cos(z,\bar{z}) \end{pmatrix} \tag{A.5}$$

$\boldsymbol{t}$ is the Direction Cosine Matrix (DCM) between local coordinate system ($Oxyz$) and global coordinate system ($\bar{O}\bar{x}\bar{y}\bar{z}$).

For brevity, the displacement finite element approximation is designated as

$$\begin{pmatrix} w_x^e \\ w_y^e \\ w_z^e \\ \theta_x^e \end{pmatrix} = \boldsymbol{N}_1^e \tilde{\boldsymbol{u}}^e, \ \boldsymbol{N}_1^e := \boldsymbol{\Phi}_u^e \boldsymbol{T}_u^e \tag{A.6}$$

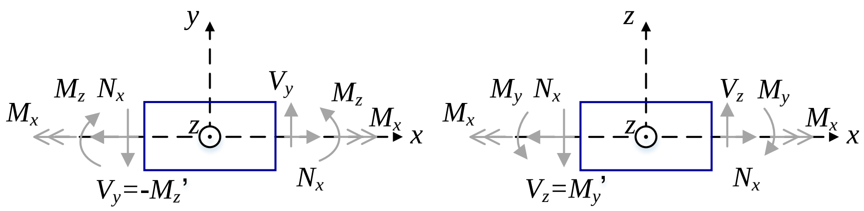

Figure A.2 Basics of a force-based finite element e

A.2 Force-based beam element

In the force-based finite dimensional space, the discretized stress field $(N_x^e, M_z^e, M_y^e, M_x^e)$ (see **Figure A.2**) for an arbitary element e should be constructed at first. Practically, this can be reached by setting

$$(N_x^e, M_z^e, M_y^e, M_x^e) = (N_x^{0e}, M_z^{0e}, M_y^{0e}, M_x^{0e}) + (N_x^{pe}, M_z^{pe}, M_y^{pe}, M_x^{pe}) \tag{A.7}$$

where $(N_x^{pe}, M_z^{pe}, M_y^{pe}, M_x^{pe})$ is the inhomogeneous part caused by the concentrated loads on Neumann boundary $\partial\Omega_f$ and $(N_x^{0e}, M_z^{0e}, M_y^{0e}, M_x^{0e})$ is the homogeneous part approximated by the following force element.

Auxiliary local nodal forces $(N_x^i, V_y^i, V_z^i, M_x^i, M_y^i, M_z^i)$ at an arbitrary node i are used to construct the homogeneous discretized stress field $(N_x^0, M_z^0, M_y^0, M_x^0)$ initially; that is, for element e, $(N_x^{0e}, M_z^{0e}, M_y^{0e}, M_x^{0e})$ are given by

$$\begin{aligned}
&\left(N_x^{0e}, M_z^{0e}, M_y^{0e}, M_x^{0e}\right)^T = \boldsymbol{\Phi}_q^e \tilde{\boldsymbol{q}}_{0L}^e, \\
&\tilde{\boldsymbol{q}}_{0L}^e := [N_x^i, V_y^i, V_z^i, M_x^i, M_y^i, M_z^i, N_x^j, V_y^j, V_z^j, M_x^j, M_y^j, M_z^j]^T \\
&\boldsymbol{\Phi}_q^e := \begin{pmatrix} N_1 & 0 & 0 & 0 & 0 & 0 & N_2 & 0 & 0 & 0 & 0 & 0 \\ 0 & -H_2 & 0 & 0 & 0 & H_1 & 0 & -H_4 & 0 & 0 & 0 & H_3 \\ 0 & 0 & H_2 & 0 & H_1 & 0 & 0 & 0 & H_4 & 0 & H_3 & 0 \\ 0 & 0 & 0 & N_1 & 0 & 0 & 0 & 0 & 0 & N_2 & 0 & 0 \end{pmatrix}
\end{aligned} \tag{A.8}$$

where $\boldsymbol{\Phi}_q^e$ is the shape function matrix. Having gained $(N_x^{0e}, M_z^{0e}, M_y^{0e}, M_x^{0e})$ in equation (A.8) via the auxiliary local nodal forces, the next is to shift into the usage of global nodal forces. To this end, the transformation matrix for the force finite element pertains to be

$$\boldsymbol{T}_q^e = \boldsymbol{H}\boldsymbol{T}_u^e \tag{A.9}$$

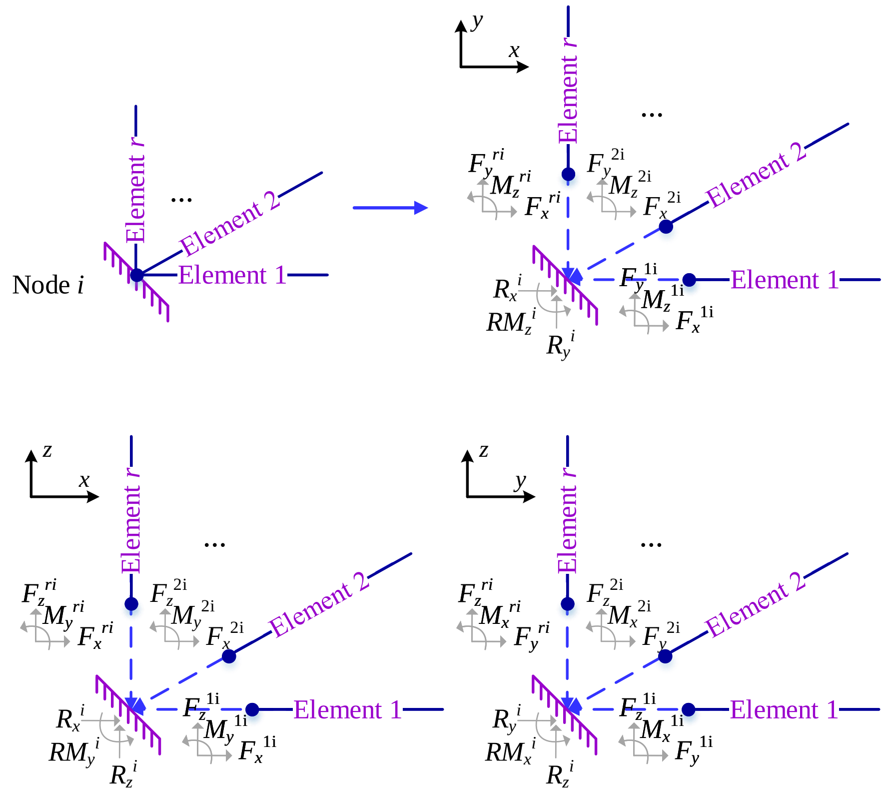

Figure A.3 Equilibrium at a node i

where

$$\boldsymbol{H} = \begin{pmatrix} -\boldsymbol{I}_{6\times6} & \mathbf{0} \\ \mathbf{0} & \boldsymbol{I}_{6\times6} \end{pmatrix} \tag{A.10}$$

Hence, the relationship between local element nodal forces $\tilde{\boldsymbol{q}}^e_{0L}$ and global element nodal forces $\tilde{\boldsymbol{q}}^e_0$ in terms of element e is given by

$$\tilde{\boldsymbol{q}}^e_{0L} = \boldsymbol{T}^e_q \tilde{\boldsymbol{q}}^e_0 \tag{A.11}$$

Next, the formulation of nodal equilibriums is utilized to find independent global nodal force (DOFs) $\hat{\boldsymbol{q}}^e_0$. Element nodal forces $\tilde{\boldsymbol{q}}^{ei}_0 = [F^{ei}_x, F^{ei}_y, F^{ei}_z, M^{ei}_x, M^{ei}_y, M^{ei}_z]^T$ of all r beams as well as reaction forces $\boldsymbol{R}^i_G = [R^i_x, R^i_y, R^i_z, RM^i_x, RM^i_y, RM^i_z]^T$ adjacent to the objective node i in the directions of all the degrees of freedom are algebraically summed up as shown in **Figure A.3**. This is carried out for all nodes. The equilibrium equation for each node i is accordingly given by

$$\sum_{e=1}^{r} \tilde{\boldsymbol{q}}_0^{ei} + \boldsymbol{R}_G^i = \boldsymbol{0} \tag{A.12}$$

Based on this equilibrium equation, dependent nodal forces $\tilde{\boldsymbol{q}}_0^{ri}$ could be represented by independent global nodal forces $\hat{\boldsymbol{q}}_0^{ei} := (\tilde{\boldsymbol{q}}_0^{ei}, e = 1, 2, \cdots, r-1, \boldsymbol{R}_G^i)$ for the node i in the sequel

$$\boldsymbol{n}\hat{\boldsymbol{q}}_0^{ei} = -\sum_{e=1}^{r-1} \tilde{\boldsymbol{q}}_0^{ei} - \boldsymbol{R}_G^i = \tilde{\boldsymbol{q}}_0^{ri} \tag{A.13}$$

where $\boldsymbol{n}$ stands for the linear combination of $\{\tilde{\boldsymbol{q}}_0^{ei}, e = 1, 2, \cdots, r-1\}$ and $\boldsymbol{R}_G^i$. It should be noticed that homogeneous Neumann boundary conditions should be enforced on reaction forces $\boldsymbol{R}_G^i$, setting corresponding forces to be zero for different types of supports. Thus, one can obtain for an element e with an ending node i that

$$[F_x^{ei}, F_y^{ei}, F_z^{ei}, M_x^{ei}, M_y^{ei}, M_z^{ei}]^T = \boldsymbol{L}_i^e \hat{\boldsymbol{q}}_0^{ei} \tag{A.14}$$

where

$$\begin{gathered} \boldsymbol{L}_i^e(3e-2:3e, 3e-2:3e) = \boldsymbol{I}_{3\times 3} \text{ for } e = 1, 2, \cdots, r-1 \\ \boldsymbol{L}_i^e = \boldsymbol{n} \text{ for } e = r \end{gathered} \tag{A.15}$$

Integrating Equations (A.8),(A.11) and (A.14), the force finite element approximation of $(\hat{N}_h^e, \hat{M}_h^e)$ is established as

$$\begin{gathered} \begin{pmatrix} N_x^{0e} \\ M_z^{0e} \\ M_y^{0e} \\ M_x^{0e} \end{pmatrix} = \boldsymbol{\Psi}_q^e \hat{\boldsymbol{q}}_0^e = \boldsymbol{N}_2^e \tilde{\boldsymbol{q}}_0^e \\ \boldsymbol{\Psi}_q^e := \boldsymbol{N}_2^e \begin{pmatrix} \boldsymbol{L}_i^e & \boldsymbol{0} \\ \boldsymbol{0} & \boldsymbol{L}_i^e \end{pmatrix} = \boldsymbol{\Phi}_q^e \boldsymbol{T}_q^e \begin{pmatrix} \boldsymbol{L}_i^e & \boldsymbol{0} \\ \boldsymbol{0} & \boldsymbol{L}_i^e \end{pmatrix} \\ \tilde{\boldsymbol{q}}_0^e = \begin{pmatrix} \boldsymbol{L}_i^e & \boldsymbol{0} \\ \boldsymbol{0} & \boldsymbol{L}_i^e \end{pmatrix} \hat{\boldsymbol{q}}_0^e = \begin{pmatrix} \boldsymbol{L}_i^e & \boldsymbol{0} \\ \boldsymbol{0} & \boldsymbol{L}_i^e \end{pmatrix} \begin{pmatrix} \hat{\boldsymbol{q}}_0^i \\ \hat{\boldsymbol{q}}_0^j \end{pmatrix} \end{gathered} \tag{A.16}$$

Turning to the particular part $(N_x^{pe}, M_z^{pe}, M_y^{pe}, M_x^{pe})$, the external concentrated loads are directly involved. Assume that the concentrated loads $\tilde{\boldsymbol{q}}_p^e := [F_{px}, F_{py}, F_{pz},$

M_{px},$M_{py}, M_{pz}]^T$ are enforced on the left-hand side $k = 1$ (or right-hand side $k = 2$) of the element e. Under this circumstance, (N_x^{pe}, M_z^{pe}, M_y^{pe}, M_x^{pe}) could be obtained by the interpolation matrix defined in equation (A.1) and transformation matrix defined in equation (A.9) as follows

$$\begin{pmatrix} N_x^{pe} \\ M_z^{pe} \\ M_y^{pe} \\ M_x^{pe} \end{pmatrix} = \boldsymbol{N}_2^e \tilde{\boldsymbol{q}}_p^e \tag{A.17}$$

where $\tilde{\boldsymbol{q}}_p$ collects all concentrated loads ($F_{px}, F_{py}, F_{pz}, M_{px}, M_{py}, M_{pz}$).

Finally, substituting Equation (A.16) and (A.17) into Equation (A.7) and simplifying, one can get

$$\begin{pmatrix} N_x^{e} \\ M_z^{e} \\ M_y^{e} \\ M_x^{e} \end{pmatrix} = \boldsymbol{N}_2^e \tilde{\boldsymbol{q}}_0^e + \boldsymbol{N}_2^e \tilde{\boldsymbol{q}}_p^e \tag{A.18}$$

References

[1] Wei Fan and Pizhong Qiao. Vibration-based damage identification methods: a review and comparative study. *Structural Health Monitoring*, 10(1):83–111, 2011.

[2] Mario Di Paola and Cristiano Bilello. An integral equation for damage identification of euler-bernoulli beams under static loads. *Journal of Engineering Mechanics*, 130(2):225–234, 2004.

[3] Pelin Gundes Bakir, Edwin Reynders, and Guido De Roeck. Sensitivity-based finite element model updating using constrained optimization with a trust region algorithm. *Journal of Sound and Vibration*, 305(1-2):211–225, 2007.

[4] ZD Zheng, ZR Lu, WH Chen, and JK Liu. Structural damage identification based on power spectral density sensitivity analysis of dynamic responses. *Computers & Structures*, 146:176–184, 2015.

[5] ZR Lu and SS Law. Features of dynamic response sensitivity and its application in damage detection. *Journal of Sound and Vibration*, 303(1-2):305–329, 2007.

[6] GR Liu and SC Chen. A novel technique for inverse identification of distributed stiffness factor in structures. *Journal of Sound and Vibration*, 254(5):823–835, 2002.

[7] Mohamed Abdel-Basset Abdo. Parametric study of using only static response in structural damage detection. *Engineering Structures*, 34:124–131, 2012.

[8] D Huynh, J He, and D Tran. Damage location vector: A non-destructive structural damage detection technique. *Computers & Structures*, 83(28):2353–2367, 2005.

[9] SH Sung, HJ Jung, and HY Jung. Damage detection for beam-like structures using the normalized curvature of a uniform load surface. *Journal of Sound and Vibration*, 332(6):1501–1519, 2013.

[10] O Begambre and José Elias Laier. A hybrid particle swarm optimization–simplex algorithm (PSOS) for structural damage identification. *Advances in Engineering Software*, 40(9):883–891, 2009.

[11] Adriana Hera and Zhikun Hou. Application of wavelet approach for asce structural health monitoring benchmark studies. *Journal of Engineering Mechanics*, 130(1): 96–104, 2004.

[12] N Roveri and A Carcaterra. Damage detection in structures under traveling loads by hilbert–huang transform. *Mechanical Systems and Signal Processing*, 28:128–144, 2012.

[13] Bijaya Jaishi and Wei-Xin Ren. Damage detection by finite element model updating using modal flexibility residual. *Journal of Sound and Vibration*, 290(1-2): 369–387, 2006.

[14] Zhong-Rong Lu and Li Wang. An enhanced response sensitivity approach for structural damage identification: convergence and performance. *International journal for numerical methods in engineering*, 111(13):1231–1251, 2017.

[15] Jesiel Cunha, Scott Cogan, and Christophe Berthod. Application of genetic algorithms for the identification of elastic constants of composite materials from dynamic tests. *International Journal for Numerical Methods in Engineering*, 45 (7):891–900, 1999.

[16] GR Liu and SC Chen. Flaw detection in sandwich plates based on time-harmonic response using genetic algorithm. *Computer Methods in Applied Mechanics and Engineering*, 190(42):5505–5514, 2001.

[17] Hua-Peng Chen and Than Soe Maung. Regularised finite element model updating using measured incomplete modal data. *Journal of Sound and Vibration*, 333(21): 5566–5582, 2014.

[18] Mohamed Kaouk and David C Zimmerman. Structural damage assessment using a generalized minimum rank perturbation theory. *AIAA Journal*, 32(4):836–842, 1994.

[19] I Ojalvo and D Pilon. Diagnostics for geometrically locating structural math model errors from modal test data. In *29th Structures, Structural Dynamics and Materials Conference*, page 2358, 1988.

[20] Mo R Banan, Ma R Banan, and KD Hjelmstad. Parameter estimation of structures from static response. I. Computational aspects. *Journal of Structural Engineering*, 120(11):3243–3258, 1994.

[21] Mo R Banan, Ma R Banan, and KD Hjelmstad. Parameter estimation of structures from static response. II. Numerical simulation studies. *Journal of Structural Engineering*, 120(11):3259–3283, 1994.

[22] Erasmo Viola and Paolo Bocchini. Non-destructive parametric system identification and damage detection in truss structures by static tests. *Structure and Infrastructure Engineering*, 9(5):384–402, 2013.

[23] Pierre Ladevèze and Amar Chouaki. Application of a posteriori error estimation for structural model updating. *Inverse Problems*, 15(1):49, 1999.

[24] Giuseppe Geymonat and Stéphane Pagano. Identification of mechanical properties by displacement field measurement: a variational approach. *Meccanica*, 38(5):535–545, 2003.

[25] Jia Guo, Li Wang, and Izuru Takewaki. Static damage identification in beams by minimum constitutive relation error. *Inverse Problems in Science and Engineering*, 2018. doi: 10.1080/17415977.2018.1553965.

[26] Pierre Feissel and Olivier Allix. Modified constitutive relation error identification strategy for transient dynamics with corrupted data: The elastic case. *Computer Methods in Applied Mechanics and Engineering*, 196(13):1968–1983, 2007.

[27] Benoît Blaysat, E Florentin, Gilles Lubineau, and Ali Moussawi. A dissipation gap method for full-field measurement-based identification of elasto-plastic material

parameters. *International Journal for Numerical Methods in Engineering*, 91(7): 685–704, 2012.

[28] Marc Bonnet and Andrei Constantinescu. Inverse problems in elasticity. *Inverse Problems*, 21(2):R1, 2005.

[29] Biswanath Banerjee, Timothy F Walsh, Wilkins Aquino, and Marc Bonnet. Large scale parameter estimation problems in frequency-domain elastodynamics using an error in constitutive equation functional. *Computer Methods in Applied Mechanics and Engineering*, 253:60–72, 2013.

[30] Francis B Hildebrand. *Methods of applied mathematics.* Courier Corporation, 2012.

[31] Ernst Hellinger. *Die allgemeinen ansätze der mechanik der kontinua.* 1913.

[32] Eric Reissner. On a variational theorem in elasticity. *Journal of Mathematics and Physics*, 29(1-4):90–95, 1950.

[33] Kyūichirō Washizu. On the variational principles of elasticity and plasticity. Technical report, Massachusetts Inst of Tech Cambridge Aeroelastic and Structures Research Lab, 1955.

[34] Arnaud Deraemaeker, Pierre Ladevèze, and Ph Leconte. Reduced bases for model updating in structural dynamics based on constitutive relation error. *Computer methods in applied mechanics and engineering*, 191(21-22):2427–2444, 2002.

[35] Olgierd Cecil Zienkiewicz, Robert Leroy Taylor, Olgierd Cecil Zienkiewicz, and Robert Lee Taylor. *The finite element method*, volume 36. McGraw-hill London, 1977.

[36] B Titurus and MI Friswell. Regularization in model updating. *International Journal for Numerical Methods in Engineering*, 75(4):440–478, 2008.

[37] Chun Zhang, Jie-Zhong Huang, Gu-Quan Song, and Lin Chen. Structural damage identification by extended kalman filter with ℓ_1-norm regularization scheme. *Structural Control and Health Monitoring*, page e1999, 2017. doi: 10.1002/stc.1999.

[38] Eric M Hernandez. Identification of isolated structural damage from incomplete spectrum information using l1-norm minimization. *Mechanical Systems and Signal Processing*, 46(1):59–69, 2014.

[39] Emmanuel J Candes, Michael B Wakin, and Stephen P Boyd. Enhancing sparsity by reweighted ℓ_1 minimization. *Journal of Fourier Analysis and Applications*, 14 (5):877–905, 2008.

[40] Pierre Ladeveze and Dominique Leguillon. Error estimate procedure in the finite element method and applications. *SIAM Journal on Numerical Analysis*, 20(3): 485–509, 1983.

[41] P-E Charbonnel, P Ladevèze, F Louf, and Ch Le Noac'h. A robust cre-based approach for model updating using in situ measurements. *Computers & Structures*, 129:63–73, 2013.

[42] Eric Florentin and Gilles Lubineau. Identification of the parameters of an elastic material model using the constitutive equation gap method. *Computational Mechanics*, 46(4):521–531, 2010.

[43] D Barthe, Arnaud Deraemaeker, Pierre Ladevèze, and Sebastien Le Loch. Validation and updating of industrial models based on the constitutive relation error. *AIAA journal*, 42(7), 2004.

[44] Ian Knowles. Uniqueness for an elliptic inverse problem. *SIAM Journal on Applied Mathematics*, 59(4):1356–1370, 1999.

[45] Ian Knowles. Parameter identification for elliptic problems. *Journal of Computational and Applied Mathematics*, 131(1):175–194, 2001.

[46] Robert V Kohn and Bruce D Lowe. A variational method for parameter identification. *ESAIM: Mathematical Modelling and Numerical Analysis*, 22(1):119–158, 1988.

[47] Gerard R Richter. An inverse problem for the steady state diffusion equation. *SIAM Journal on Applied Mathematics*, 41(2):210–221, 1981.

[48] Thomas Widlak and Otmar Scherzer. Stability in the linearized problem of quantitative elastography. *Inverse Problems*, 31(3):035005, 2015.

[49] Amir Beck. On the convergence of alternating minimization for convex programming with applications to iteratively reweighted least squares and decomposition schemes. *SIAM Journal on Optimization*, 25(1):185–209, 2015.

[50] HM Lee and HS Park. Gage-free stress estimation of a beam-like structure based on terrestrial laser scanning. *Computer-Aided Civil and Infrastructure Engineering*, 26(8):647–658, 2011.

[51] CD Zhang and YL Xu. Comparative studies on damage identification with tikhonov regularization and sparse regularization. *Structural Control and Health Monitoring*, 23(3):560–579, 2016.

[52] Mark Schmidt. Least squares optimization with l1-norm regularization. *CS542B Project Report*, pages 14–18, 2005.

[53] Mee Young Park and Trevor Hastie. L1-regularization path algorithm for generalized linear models. *Journal of the Royal Statistical Society: Series B (Statistical Methodology)*, 69(4):659–677, 2007.

[54] M Saiidi, B Douglas, and S Feng. Prestress force effect on vibration frequency of concrete bridges. *Journal of Structural Engineering-ASCE*, 120(7):2233–2241, 1994.

[55] Jeong-Tae Kim, Yeon-Sun Ryu, Hyun-Man Cho, and Norris Stubbs. Damage identification in beam-type structures: frequency-based method vs mode-shape-based method. *Engineering Structures*, 25(1):57–67, 2003.

[56] Benedikt Weber, Patrick Paultre, and Jean Proulx. Structural damage detection using nonlinear parameter identification with tikhonov regularization. *Structural Control and Health Monitoring*, 14(3):406–427, 2007.

[57] PF Rizos, N Aspragathos, and AD Dimarogonas. Identification of crack location and magnitude in a cantilever beam from the vibration modes. *Journal of Sound and Vibration*, 138(3):381–388, 1990.

[58] KD Hjelmstad and S Shin. Crack identification in a cantilever beam from modal response. *Journal of Sound and Vibration*, 198(5):527–545, 1996.

[59] N Hu, X Wang, H Fukunaga, ZH Yao, HX Zhang, and ZS Wu. Damage assessment of structures using modal test data. *International Journal of solids and structures*, 38(18):3111–3126, 2001.

[60] Yongchao Yang and Satish Nagarajaiah. Structural damage identification via a combination of blind feature extraction and sparse representation classification. *Mechanical Systems and Signal Processing*, 45(1):1–23, 2014.

[61] Doo-Ho Lee and Woo-Seok Hwang. Parametric optimization of complex systems using a multi-domain FRF-based substructuring method. *Computers & structures*, 81(22-23):2249–2257, 2003.

[62] A Esfandiari, F Bakhtiari-Nejad, A Rahai, and M Sanayei. Structural model updating using frequency response function and quasi-linear sensitivity equation. *Journal of Sound and Vibration*, 326(3):557–573, 2009.

[63] Z Wang, RM Lin, and MK Lim. Structural damage detection using measured frf data. *Computer methods in applied mechanics and engineering*, 147(1-2):187–197, 1997.

[64] Havard Vold, John Crowley, and G Thomas Rocklin. New ways of estimating frequency response functions. *Sound & Vibration*, 18(11):34–38, 1984.

[65] John E Mottershead, Michael Link, and Michael I Friswell. The sensitivity method in finite element model updating: a tutorial. *Mechanical systems and signal processing*, 25(7):2275–2296, 2011.

[66] Rongrong Hou, Yong Xia, Yuequan Bao, and Xiaoqing Zhou. Selection of regularization parameter for l1-regularized damage detection. *Journal of Sound and Vibration*, 423:141–160, 2018.

[67] Zhong-Rong Lu, Junxian Zhou, and Li Wang. On choice and effect of weight matrix for response sensitivity-based damage identification with measurement and model errors. *Mechanical Systems and Signal Processing*, 114:1–24, 2019.

[68] JV Araujo Dos Santos, CM Mota Soares, CA Mota Soares, and NMM Maia. Structural damage identification in laminated structures using FRF data. *Composite Structures*, 67(2):239–249, 2005.

[69] Jerome Friedman, Trevor Hastie, and Robert Tibshirani. *The elements of statistical learning*, volume 1. Springer series in statistics New York, 2001.

[70] Jiahao Lin, Wenshou Zhang, and Jianjun Li. Structural responses to arbitrarily coherent stationary random excitations. *Computers & structures*, 50(5):629–633, 1994.

[71] Jiahao Lin, Yan Zhao, and Yahui Zhang. Accurate and highly efficient algorithms for structural stationary/non-stationary random responses. *Computer Methods in Applied Mechanics and Engineering*, 191(1-2):103–111, 2001.

[72] Jia Guo, Li Wang, and Izuru Takewaki. Modal-based structural damage identification by minimum constitutive relation error and sparse regularization. *Structural Control and Health Monitoring*, page e2255, 2018. doi: 10.1002/stc.2255.

[73] Koushik Roy and Samit Ray-Chaudhuri. Fundamental mode shape and its derivatives in structural damage localization. *Journal of Sound and Vibration*, 332(21): 5584–5593, 2013.

[74] Jia Guo, Li Wang, and Izuru Takewaki. Frequency response-based damage identification in frames by minimum constitutive relation error and sparse regularization. *Journal of Sound and Vibration*, 443:270–292, 2018. doi: 10.1016/j.jsv.2018.11.020.

Publications

Journal Papers (Published)

1) Guo J, Wang L, Takewaki I. Frequency response-based damage identification in frames by minimum constitutive relation error and sparse regularization. Journal of Sound and Vibration, 443: 270-292, 2019.
2) Guo J, Wang L, Takewaki I. Modal-based structural damage identification by minimum constitutive relation error and sparse regularization. Structural Control and Health Monitoring, 25(12): e2255, 2018. 3.
3) Guo J, Wang L, Takewaki I. Static damage identification in beams by minimum constitutive relation error. Inverse Problems in Science and Engineering, DOI:10.1080/17415977.2018.1553965. (Published online: 11 Dec 2018).

Journal Papers (In Review)

4) Jia Guo, Jiao Jian, Kohei Fujita, and Izuru Takewaki, A spectrum-driven damage identification by minimum constitutive relation error. Mechanical Systems and Signal Processing, 2018 (in review).

Conference Papers

5) Guo J, Takewaki I. Minimum constitutive relation error based static identification of beams using force method. Journal of Physics: Conference Series. IOP Publishing, 842(1): 012026, 2017.
6) 郭　佳，竹脇　出．構成則誤差最小化とスパース正則化を用いたモーダル構造損傷同定解析，日本建築学会大会，仙台（2018 年 9 月）